REPORT DOCUMENTATION PAGE

PLEASE DO NOT RETURN YOUR FORM TO THE ABOVE ORGANIZATION.

1. REPORT DATE 20210712	**2. REPORT TYPE** Final	**3. DATES COVERED** **START DATE** 20170101	**END DATE** 20210228

4. TITLE AND SUBTITLE

Physical understanding and predictive modeling of high Reynolds number non-equilibrium turbulent boundary layers

5a. CONTRACT NUMBER N00014-17-1-2310	**5b. GRANT NUMBER** N00014-17-1-2310	**5c. PROGRAM ELEMENT NUMBER**
5d. PROJECT NUMBER	**5e. TASK NUMBER**	**5f. WORK UNIT NUMBER**

6. AUTHOR(S)

Parviz Moin

7. PERFORMING ORGANIZATION NAME(S) AND ADDRESS(ES)

Leland Stanford Junior
University488 Escondido Mall
Stanford, CA 94305

8. PERFORMING ORGANIZATION REPORT NUMBER

9. SPONSORING/MONITORING AGENCY NAME(S) AND ADDRESS(ES)

Office of Naval Research
875 N. Randolph Street, Ste. 1425
Arlington, VA 22203-1995

10. SPONSOR/MONITOR'S ACRONYM(S)

11. SPONSOR/MONITOR'S REPORT NUMBER(S)

12. DISTRIBUTION/AVAILABILITY STATEMENT

Approved for Public Release; distribution is Unlimited

13. SUPPLEMENTARY NOTES

14. ABSTRACT

Much of the research on a turbulent boundary layer (TBL) have focused on equilibrium turbulence found in idealized zero-pressure gradient flows over flat plates. However, the vast knowledge of equilibrium turbulence gained over the last 50 years has had limited impact on our ability to predict practical flows of interest. The reason is that TBLs in realistic flows are affected strongly by non-equilibrium effects controlled by flow-dependent boundary conditions. Additionally, regarding prediction of practical flows, wall-modeled large-eddy simulation (WMLES) is now perceived as an alternative to costly wall-resolved LES. However, its performance in complex flows involving the three-dimensional TBL (3-D TBL) has not been assessed thoroughly to increase the technology-readiness level of the emerging WMLES methodology.

15. SUBJECT TERMS

Non-equilibrium turbulent boundary layers, Direct Numerical Simulation, Wall modeled LES, Coherent structures

16. SECURITY CLASSIFICATION OF:			**17. LIMITATION OF ABSTRACT**	**18. NUMBER OF PAGES**
a. REPORT	**b. ABSTRACT**	**C. THIS PAGE**		74

19a. NAME OF RESPONSIBLE PERSON Parviz Moin	**19b. PHONE NUMBER** *(Include area code)* (650) 723-9713

PREVIOUS EDITION IS OBSOLETE.

STANDARD FORM 298 (REV. 5/2020)
Prescribed by ANSI Std. Z39.18

FINAL REPORT

ONR Award Number: N00014-17-1-2310

Proposal Title: Physical understanding and predictive modeling of high Reynolds number non-equilibrium turbulent boundary layers

Institution: Center for Turbulence Research, Stanford University

Principal Investigator (PI): Prof. Parviz Moin

PI Contact: 650-723-9713 (phone), 650-725-3525 (fax), moin@stanford.edu (email)
Address: Center for Turbulence Research
Stanford University
488 Escondido Mall
Stanford, CA, 94305-3024

Table of Contents

1 Recapitulation of the Proposed Effort

Most of the research on a turbulent boundary layer (TBL) have focused on equilibrium turbulence found in idealized zero-pressure gradient flows over flat plates. However, the vast knowledge of equilibrium turbulence gained over the last 50 years has had limited impact on our ability to predict practical flows of interest. The reason is that TBLs in realistic flows are affected strongly by non-equilibrium effects controlled by flow-dependent boundary conditions. Additionally, regarding prediction of practical flows, wall-modeled large-eddy simulation (WMLES) is now perceived as an alternative to costly wall-resolved LES. However, its performance in complex flows involving the three-dimensional TBL (3-D TBL) has not been assessed thoroughly to increase the technology-readiness level of the emerging WMLES methodology.

The major goals of the project are 1) to elucidate structural changes in the inner and outer layers of wall turbulence at high Reynolds numbers subjected to non-equilibrium 3D effects (see figure 1), and 2) to assess the predictive capabilities of wall models for large-eddy simulation (LES) in non-equilibrium turbulent boundary layers (TBLs) with mean-flow three dimensionality, including those in a bent square duct and over a skewed bump. The overall goal of this project is to explain fundamental physical phenomena and mechanisms associated with changes of high Reynolds number wall turbulence subjected to non-equilibrium effects through high-fidelity numerical simulations. This project will also assess WMLES techniques for their application to flows exhibiting three dimensionality and separation. A robust predictive capability is thus needed for design and control of watercrafts and aircrafts with increased speed, maneuverability, and efficiency. By understanding the fundamental flow physics in non-equilibrium TBLs and extending WMLES techniques to such complex flows, this project will augment the U.S. Navys knowledge required to fulfill this objective.

2 TASK 1: DNS and WMLES analysis of a 3-D TBL in a planar channel

2.1 Introduction

Our current understanding of wall turbulence is largely rooted in studies of equilibrium boundary layers with two-dimensional (2-D) mean velocity profiles (i.e., contained in a plane). However, non-equilibrium turbulence with mean-flow three-dimensionality is the rule rather than the exception in most geophysical and engineering flows. Prominent examples of the former are flows in complex terrain, tornadoes, and river bends, while industrial flows include flow over swept-wing aircrafts and hulls of marine vehicles, around buildings and obstacles, within turbomachines, etc. Despite the ubiquity of such flows, fundamental questions remain unanswered regarding the structural changes of wall turbulence under three-dimensional (3-D) non-equilibrium conditions, challenging our intellectual ability to comprehend and predict wall turbulence in broader scenarios. In the present work, we study the transition of statistically stationary 2-D turbulence to non-stationary 3-D states induced by the sudden application of a spanwise pressure gradient. Our emphasis is on the multiscale structure of wall-bounded turbulence at moderately high Reynolds numbers.

The vast majority of the fundamental studies on wall turbulence has focused on a narrow subset of equilibrium 2-D wall-bounded flows (2DTBL) such as turbulent channels (Kim *et al.*, 1987; Lee & Moser, 2015), pipes (Wu *et al.*, 2015; Pirozzoli *et al.*, 2018), and flat-plate boundary layers (Spalart, 1988; Sillero *et al.*, 2013, 2014; Wu *et al.*, 2017). These studies have unravelled constitutive characteristics of the near-wall turbulence, including its self-sustaining nature (Jiménez & Moin, 1991; Jiménez & Pinelli, 1999; Panton, 2001; Flores & Jiménez, 2010; Hwang & Cossu, 2011; Hwang, 2015; Farrell *et al.*, 2016, 2017), the coherent structure and geometry of the flow (del Álamo & Jiménez, 2006; Kawahara *et al.*, 2012; Lozano-Durán *et al.*, 2012; Dong *et al.*, 2017; McKeon, 2017), the life cycle of the momentum-carrying eddies (Lozano-Durán & Jiménez, 2014*b*; Hwang & Cossu, 2010; Cossu & Hwang, 2017), and the wall-attached structure of the flow in the logarithmic layer (Marusic *et al.*, 2013; Hwang & Bengana, 2016; Chandran *et al.*, 2017; Marusic & Monty, 2019; Cheng *et al.*, 2019), among others. Unfortunately, theories built upon equilibrium wall-turbulence have had limited impact on our ability to predict 3-D boundary layers (3DTBL) and to grasp the physics underlying the extensive collection of numerical and experimental observations. This is principally due to the violation of the temporal/spatial homogeneity of the flow and the unidirectionality of the mean shear, which are foundational assumptions of 2DTBL absent in 3DTBL. Consequently, the knowledge established largely for equilibrium 2DTBL, such as the law-of-the-wall (Prandtl, 1925; Millikan, 1938; Coles & Hirst, 1969), the scaling laws for the velocity and energy spectra (Perry & Abell, 1975, 1977; Zagarola & Smits, 1998; Morrison *et al.*, 2004; del Álamo *et al.*, 2004; Marusic *et al.*, 2013; Vallikivi *et al.*, 2015; Hoyas & Jiménez, 2006; Klewicki *et al.*, 2007; Chandran *et al.*, 2017), structural models of the flow (Townsend, 1976; Adrian *et al.*, 2000; Meneveau & Marusic, 2013; Agostini & Leschziner, 2017; Lozano-Durán & Bae, 2019; Jiménez, 2018; Marusic & Monty, 2019), and reduced-order models (Rowley & Dawson, 2017; Durbin, 2018; Bose & Park, 2018), cannot be generalised trivially to non-canonical 3DTBL.

Often, 3DTBL are classified according to their state as either in equilibrium or in non-equilibrium. Townsend (1961) was the first to coin the term 'equilibrium layer' to define a portion of the boundary layer in which the rates of production and dissipation of turbulent kinetic energy are equal. De Graaff & Eaton (2000) suggested a more restrictive definition in which the total shear stress is balanced by the shear stress at the wall. A comprehensive theory of equilibrium and self-similar flow motions in the outer region of turbulent boundary layers can be also found in the works by Castillo & George (2001) and Maciel *et al.* (2006, 2018). Here, we refer to equilibrium flow simply as that in statistically stationary state. Despite equilibrium 3DTBL, such as the Ekman layer, being of paramount importance (see e.g. Spalart (1989); Coleman *et al.* (1990); Littell & Eaton (1994); Wu & Squires (1997)), the subject of the present work is the non-equilibrium response of 3DTBL, which is one of the most challenging cases for the current turbulence theories. In addition to their equilibrium state (or lack thereof), 3DTBL are also classified according to the mechanisms by which the three-dimensionality is incorporated into the flow. In this respect, 3DTBL can be labelled as 'viscous-induced' when the three-dimensionality is a direct consequence of the viscous effects propagating from the solid boundaries (e.g., moving walls, accelerating frames of reference,...), or as 'inviscid-induced' when the 3-D flow is the result of space-varying body forces or pressure gradients (such as those triggered by the presence of complex geometries or by baroclinic effects in atmospheric flows). These two mechanisms are usually referred to as shear-driven and pressure-driven in the literature, although such a nomenclature may lead to confusion in some situations. Here we are concerned with the first kind, i.e. 'viscous-induced' 3DTBL, which are relevant for turbomachinery applications and large-scale wind farms, just to mention two examples, albeit it is worth noting that in many real life scenarios three-dimensionality is induced by a combination of the two mechanisms.

From the early works by Bradshaw & Terrell (1969) and Van den Berg & Elsenaar (1972), it was readily noted that 3DTBL exhibit a response contrary to the common expectations from their 2-D counterparts. Such counter-intuitive effects manifest themselves in the reduction of the tangential Reynolds stress and the misalignment of the Reynolds stress and mean shear 'vectors'. These observations have been reported for both equilibrium and non-equilibrium 3DTBL, albeit the effects are exacerbated in the latter. The pioneering studies on 3DTBL were laboratory experiments. Bradshaw & Terrell (1969) presented the first set of Reynolds-stress measurements in a yawed flat plate as a surrogate of an 'infinite' swept wing. They observed a lag between the Reynolds stress angle and the mean velocity gradient angle despite the mild three-dimensionality of the flow. Subsequent experiments by Johnston (1970), Van den Berg *et al.* (1975) and Bradshaw & Pontikos (1985) confirmed the aforementioned behaviour in similar set-ups. In a succeeding series of studies, Van den Berg & Elsenaar (1972), Elsenaar & Boelsma (1974) and Van den Berg *et al.* (1975) further showed that the intensity of the Reynolds stress for a given amount of turbulent kinetic energy (a.k.a. Townsend's structure parameter) dropped below the commonly reported value in 2-D flows, establishing the second main counter-intuitive effect of 3DTBL.

Over the past decades, a variety of additional experimental studies on 3DTBL have been performed, each characterised by the different mechanism utilised to induce three-dimensionality in the flow. Among them, we can highlight 3DTBL over wedges (Anderson & Eaton, 1987, 1989; Compton & Eaton, 1997), rotating cylinders (Furuya & Fujita, 1966; Bissonnette & Mellor, 1974; Lohmann, 1976; Driver & Hebbar, 1987, 1989, 1991), rotating disks (Littell & Eaton, 1994), flow within the bend of ducts (Schwarz & Bradshawt, 1993; Schwarz & Bradshaw, 1994; Flack, 1993; Flack & Johnston, 1994), swept steps and bumps (Flack, 1993; Webster *et al.*, 1996), and wing-body junctions (Ölçmen & Simpson, 1992, 1995). More recently, Kiesow & Plesniak (2002, 2003) used particle-image velocimetry (PIV) to acquire detailed information of the flow structure at varying degrees of cross-flow generated by moving belts. The large body of literature on experimental 3DTBL until the 1990s is summarised in the reviews by Fernholz & Vagt (1981), van den Berg *et al.* (1988), Eaton (1995) and Johnston & Flack (1996).

The advent of direct numerical simulation (DNS) and large-eddy simulation (LES) led to an increase in the number of numerical investigations of 3DTBL. Computational studies carried out to date include channel flows subject to transverse pressure gradients (Moin *et al.*, 1990; Sendstad & Moin, 1992; Coleman *et al.*, 1996*a*; He *et al.*, 2018), flat plates with time-dependent free-stream velocity (Spalart, 1989), rotating disks (Littell & Eaton, 1994; Wu & Squires, 2000), Couette flows with spanwise pressure gradient (Holstad *et al.*, 2010), and concentric annulus with rotating inner wall (Jung & Sung, 2006), among others. Coleman *et al.* (1996*a*,*b*, 2000) computed DNS of initially 2-D fully-developed turbulence subjected to mean strains, emulating the effect of spatially varying changes of the pressure gradients in ducts or diffusers. Wu & Squires (1997, 1998) performed LES of the swept bump proposed experimentally by Webster *et al.* (1996), while other numerical investigations have introduced three-dimensionality in flow by the impulsive motion of walls in the spanwise direction (Howard & Sandham, 1997; Le, 1999; Le *et al.*, 1999), by spanwise oscillating walls (Jung *et al.*, 1992), and by a sustained lateral displacement of a finite section of the wall (Kannepalli & Piomelli, 2000).

The current consensus among the experimental and numerical studies above is that three-dimensionality of the mean flow is typically accompanied by a decrease of the tangential Reynolds stress, the reduction of drag, and the misalignment of the mean Reynolds stress vector and mean shear vector. Given that equilibrium 2-D turbulence is commonly enhanced by the addition of mean shear, the previous results are non-trivial to interpret. Accordingly, there have been multiple attempts to reconcile the non-intuitive flow response with the traditional structural organisation of near-wall turbulence (Jiménez & Moin, 1991; Jiménez & Pinelli, 1999; Schoppa & Hussain, 2002). Most structural studies of 3DTBL depart from the premise that 2DTBL are structurally 'optimal' for the generation of Reynolds stress, and that 3DTBL are essentially a distorted, less efficient version of the former. Lohmann (1976) postulated one of the first structural pictures of the flow by suggesting that transverse shear was responsible for the break up of quasi-streamwise vortices into smaller structures. Bradshaw & Pontikos (1985) further hypothesised that eddies were tilted away from their preferred alignment by the spanwise strain, which impeded the production of Reynolds stress. Eaton (1991) stated that low-speed streaks are inhibited by the mean cross-flow, which reduces the number of ejections (and hence of Reynolds stress) generated via streak instability and breakdown. Kannepalli & Piomelli (2000) also observed significant disruption of the near-wall streaks at both the leading and trailing edge of the moving wall section as the flow adjusts to the new wall boundary conditions. Later PIV measurements by Kiesow & Plesniak (2002) confirmed a significant alteration of the near-wall flow physics, with significant disruption of the streak length compared to 2DTBL. On the other hand, the works by Anderson & Eaton (1989), Sendstad & Moin (1992), Littell & Eaton (1994), Eaton (1995), and Chiang & Eaton (1996), have centred the attention on the strong asymmetry between vortices of different sign rather than on streaks as the main cause for stress reduction. They argued that the intrinsic structure of 3DTBL favour either a sweep or a ejection, which reduces the efficiency of the boundary layer to produce Reynolds stress. The LES by Wu & Squires (1997) supported the structural model proposed by Littell & Eaton (1994). However, Jung & Sung (2006) rendered the latter scenario invalid in a concentric annulus by analysing the distinctive flow features using conditional analysis.

Previous numerical studies on 3DTBL focused on relatively low Reynolds numbers in which half or a larger portion of the boundary layer is dominated by viscous effects. Experimental studies are capable of attaining higher Reynolds numbers, but the current measurement techniques have limitations in accessing the near-wall region and generating fully resolved datasets in space and time. To date, it is unclear whether distinctly different mechanisms are at work at Reynolds numbers in which the inviscid core region occupy more than 80% of the boundary layer thickness. Moreover, important questions remain unanswered at high Reynolds numbers such as the scaling properties of the Reynolds stress reduction under 3-D non-equilibrium effects, the structural modifications in the flow responsible for these changes, and the formulation of a structural model consistent with the previous observations which accounts for the multiscale nature of turbulence. Therefore, the rich information provided by high-fidelity simulations at higher Reynolds numbers is needed for a detailed understanding of 3DTBL present in most real-world applications. In the present work, we address these questions and show that our higher Reynolds numbers, even if moderate, allows us to unravel the scaling laws and multiscale structural changes in the flow previously obscured by the lack of scale separation.

Finally, it is worth mentioning that the peculiarities of 3DTBL are expected to undermine the performance of modelling techniques built on and validated for 2DTBL. Especially concerning is the development and testing of wall models for LES, motivated by the need to bypass the inner wall region in order to reduce computational costs (Chapman, 1979; Choi & Moin, 2012). Early wall models relying on equilibrium assumptions have yielded fair predictions in simple flows, but are known to be suboptimal in more complex configurations (Larsson *et al.*, 2016). This has motivated recent efforts to develop new wall models accounting for non-equilibrium effects (Balaras *et al.*, 1996; Wang & Moin, 2002; Yang *et al.*, 2015; Park & Moin, 2014), free of tunable parameters (Bose & Moin, 2014; Lozano-Durán *et al.*, 2017; Bae *et al.*, 2018*b*), and capable of delivering robust predictions for non-canonical flow settings (see for instance the recent review by Bose & Park, 2018). Note that, in general, wall models are not effective at transferring information of the flow structure from the inner to the outer layer (Piomelli & Balaras, 2002). Hence, the current flow set-up characterised by a spanwise boundary layer growing from the wall is a challenging testbed for wall-model LES (WMLES).

The primary foci of this work are the investigation of the scaling properties of 3DTBL, absent in previous numerical studies at low Reynolds numbers, and the elucidation of the structural mechanisms responsible for Reynolds stress deficit during the initial transient. The insight gained is used to envision a multiscale structural model consistent with the scalings and structural changes observed. We also inspect the implications of three-dimensionality and non-equilibrium state for WMLES. A preliminary version of this work can be found in Giometto *et al.* (2017). The paper is organised as follows. The numerical set-up and

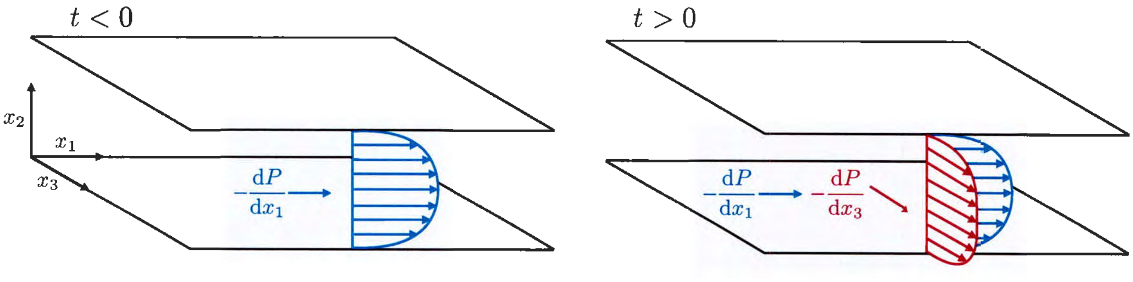

(a) (b)

Figure 1: Schematic of the numerical set-up of a 2-D fully-developed turbulent channel flow subjected to a sudden transverse pressure gradient at $t = 0$. The profiles in blue and red represent the streamwise and spanwise mean velocity profiles, respectively. The channel flow is driven by a streamwise $\mathrm{d}P/\mathrm{d}x_1$ and spanwise $\mathrm{d}P/\mathrm{d}x_3$ mean pressure gradient applied in the streamwise and spanwise direction, respectively.

database are presented in §2.2. The analysis of the scaling and flow structure of the flow is discussed in §2.3. In §2.4, we focus on the comparison of selected quantities for DNS and wall-modelled LES. Finally, conclusions are offered in §2.8.

2.2 Problem set-up and numerical database

We perform a series of DNS of incompressible turbulent channel flow subjected to a sudden imposition of a transverse pressure gradient (Moin *et al.*, 1990). The problem set-up is sketched in figure 1. This flow configuration, despite its simplicity, has proven successful in capturing the essential features of non-equilibrium 3DTBL. The calculation is initialised with a 2-D fully-developed equilibrium channel flow. At $t = 0$, a mean spanwise pressure gradient is applied, inducing a sudden acceleration of the flow in the spanwise direction. During this process, the channel flow is driven in the streamwise direction by the usual mean streamwise pressure gradient. The current set-up is formally equivalent to the sudden application of an in-plane spanwise acceleration to the walls in the opposite direction (Panton, 1984, page 253). Our focus is on the initial transient succeeding the application of the transverse pressure gradient.

Two Reynolds numbers are considered, namely $Re_\tau = hu_\tau/\nu \approx 500$ and $Re_\tau \approx 1000$, both defined at $t = 0$, where h is the channel half-height, u_τ is the friction velocity at $t = 0$, and ν is the kinematic viscosity. The density of the fluid is ρ. The streamwise, wall-normal, and spanwise directions are represented by x_1, x_2, and x_3, respectively, and the corresponding velocities are u_1, u_2, and u_3. The pressure is denoted by p. The size of the computational domain is $L_1 \times L_2 \times L_3 = 4\pi h \times 2h \times 2\pi h$ for cases at $Re_\tau \approx 500$, and $8\pi h \times 2h \times 3\pi h$ for cases at $Re_\tau \approx 1000$. According to previous studies (Lozano-Durán & Jiménez, 2014*a*), these domain sizes should suffice to accommodate the largest structures populating the region $x_2 < 0.4h$ (Marusic *et al.*, 2013), which is the main focus of this study. Wall (or inner) units, $(\cdot)^+$, are obtained by normalising flow quantities by u_τ and ν, and outer units, $(\cdot)^*$, are defined in terms of u_τ and h. Note that $(\cdot)^+$ and $(\cdot)^*$ are referred to

Re_τ	L_1^*	L_3^*	Δ_1^+	Δ_3^+	$\Delta_{2,\min}^+$	$\Delta_{2,\max}^+$	N_2	T^*	Π	N_R
546	4π	2π	8.92	4.46	0.26	6.51	385	1	0,5,10,20,30,40,60,80	10
934	8π	3π	7.36	4.29	0.35	6.72	401	1	0,10,30,60,100	5

Table 1: Geometry and parameters of the DNS runs. Re_τ is the friction Reynolds number. $L_1^* = L_1/h$ and $L_3^* = L_3/h$ are the streamwise and spanwise dimensions of the numerical box, respectively, and h is the channel half-height. Δ_1^+ and Δ_3^+ are the spatial grid resolutions in wall units for the streamwise and spanwise direction, respectively. $\Delta_{2,\min}^+$ and $\Delta_{2,\max}^+$ are the finer (closer to the wall) and coarser (further from the wall) grid resolutions in the wall-normal direction in wall units. N_2 is the number of wall-normal grid points. The simulations are integrated for a time T^* equal to one eddy turnover time defined as $T^* = Tu_\tau/h = 1$, where u_τ is the friction velocity at $t = 0$. $\Pi = (\mathrm{d}P/\mathrm{d}x_3)/(\mathrm{d}P/\mathrm{d}x_1)$ is the spanwise to streamwise mean pressure gradient ratio driving the channel flow. N_R is the total number of runs performed per each case given by the pair (Re_τ, Π).

$t = 0$. The streamwise and spanwise mean pressure gradients are $\mathrm{d}P/\mathrm{d}x_1 = \rho u_\tau^2/h$ and $\mathrm{d}P/\mathrm{d}x_3$, respectively. A campaign of simulations at different Re_τ and multiple spanwise mean pressure gradients are performed with spanwise to streamwise mean pressure gradient ratios ranging from $\Pi = (\mathrm{d}P/\mathrm{d}x_3)/(\mathrm{d}P/\mathrm{d}x_1) = 1$ to 100. Several runs (N_R) are considered for each Re_τ and Π by initialising the simulations with various temporally-uncorrelated 2-D equilibrium turbulent channel flows. The set of simulations is summarised in table 1. Examples of the instantaneous streamwise velocity at two time instants are shown in figure 2 for $\Pi = 60$ at $Re_\tau \approx 1000$.

The simulations are performed by discretising the incompressible Navier-Stokes equations with a staggered, second-order accurate, centred, finite difference method (Orlandi, 2000) in space, and an explicit third-order accurate Runge-Kutta method (Wray, 1990) for time advancement. The system of equations is solved via an operator splitting approach (Chorin, 1968). Periodic boundary conditions are imposed in the streamwise and spanwise directions, and the no-slip condition is applied at the walls. The code has been validated in turbulent channel flows (Lozano-Durán & Bae, 2016; Bae *et al.*, 2018*c*) and flat-plate boundary layers (Lozano-Durán *et al.*, 2018). The validation for channel flows under the sudden imposition of a lateral mean pressure gradient is presented in appendix 2.5. The streamwise and spanwise grid resolutions are uniform and denoted by Δ_1 and Δ_3, respectively. The wall-normal grid resolution, Δ_2, is stretched in the wall-normal direction following an hyperbolic tangent. The time step is such that the Courant-Friedrichs-Lewy condition is always below 0.5 during the run. Details on the parameters of the numerical set-up are included in table 1. The sensitivity of the results to the grid resolution and size of the computational domain are discussed in appendix 2.6.

2.3 Analysis of non-equilibrium 3DTBL

The present section is devoted to, first, the identification of universal scaling laws for the tangential Reynolds stress in the 3-D transient channel flow described in §2.2, and second, the scrutiny of the structural and energetic alterations of the flow during the transient.

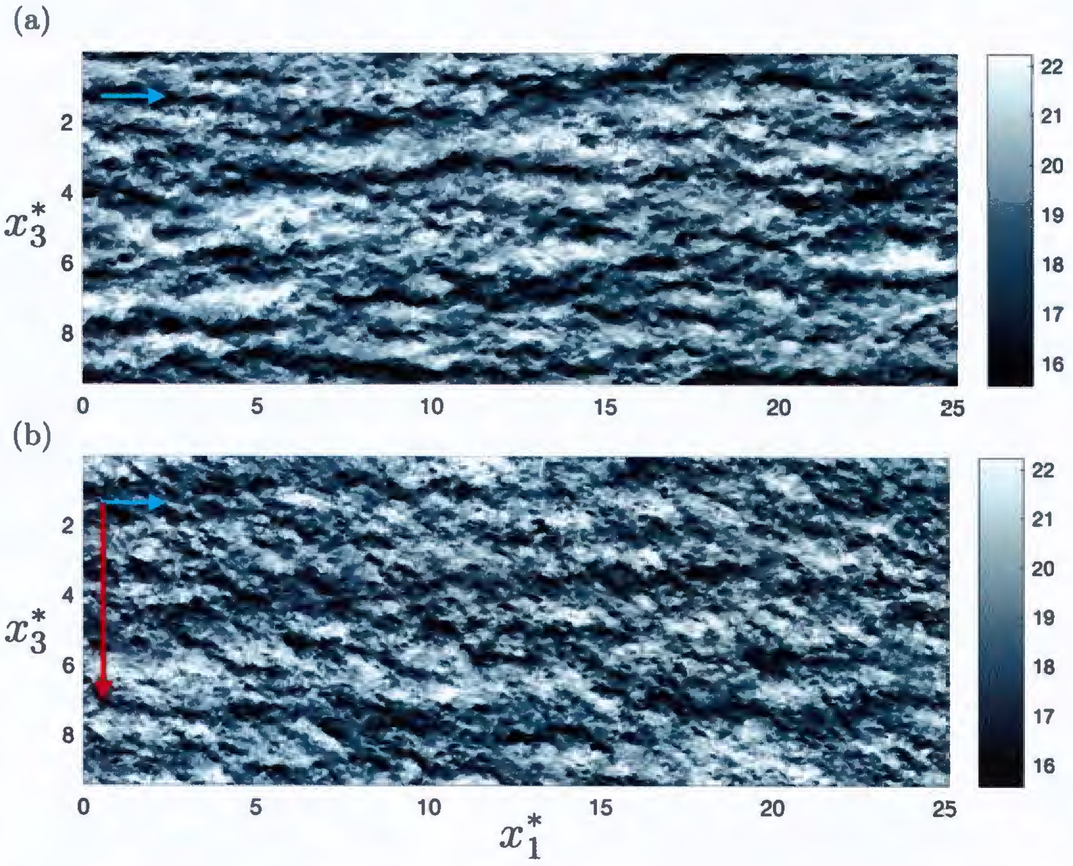

Figure 2: Instantaneous x_1–x_3 planes of the streamwise velocity at $x_2^* = 0.25$ for (a) $t^* = 0$, and (b) $t^* = 0.6$. The data is for $\Pi = 60$ at $Re_\tau \approx 1000$. The colour bars show the magnitude of the streamwise velocity normalised in wall units. The arrows represent the direction of $\mathrm{d}F/\mathrm{d}x_1$ in blue and $\mathrm{d}P/\mathrm{d}x_3$ in red, but note that lengths of the arrows are not at scale.

A large number of studies have been dedicated to the scaling of quantities of interest in fully-developed 2DTBL (see e.g., Millikan, 1938; Klewicki *et al.*, 2007; Monkewitz *et al.*, 2008). Recent efforts have been facilitated by the increased availability of numerical data at high Reynolds numbers with an appreciable scale separation between the inner and outer layers. In contrast, advances in non-equilibrium 3DTBL have been hindered by the lack of high Reynolds number flow datasets. Similar limitations apply to the analysis of structural changes on the flow.

The next section offers an overview of the evolution of the one-point statistics during the transient period, followed by a discussion on the role of the no-slip wall. Then, we classify the flow regimes and analyse the scaling laws concerning the history of the tangential Reynolds stress. The time-dependent, 3-D structural changes undergone by the flow are discussed at the end of the section, where we propose a structural model consistent with our observations.

2.3.1 Overview of one-point statistics

We select the channel flow at $Re_\tau \approx 500$ with $\Pi = 60$ as a representative case to illustrate the non-equilibrium response of the flow succeeding the imposition of the lateral pressure gradient. The systematic analysis for various Re_τ and Π is presented in §2.3.2. For $t \to \infty$, the system attains a new statistically steady state corresponding to a 2-D channel flow at higher Re_τ and mean-flow direction parallel to the vector $(\mathrm{d}P/\mathrm{d}x_1, 0, \mathrm{d}P/\mathrm{d}x_3)$. We focus on the initial transient dominated by 3-D non-equilibrium effects for $t^* < 1$. The statistical quantities of interest are computed by averaging the flow in the homogeneous directions, over the top and bottom halves of the channel, and among different runs. The averaging operator is hereafter denoted by $\langle\cdot\rangle$, and velocity fluctuations are signified by $(\cdot)'$. Fluctuating velocities are measured with respect to the time-evolving mean velocity profiles in the streamwise and spanwise direction, $\langle u_1\rangle(x_2,t)$ and $\langle u_3\rangle(x_2,t)$, respectively.

The mean velocity profiles are shown in figure 3 at several times. The streamwise mean velocity undergoes mild changes in shape (figure 3a), and the main outcome of the lateral pressure gradient is the development of a spanwise boundary layer of thickness δ_3 (figure 3b). The growth of δ_3 is initially governed by viscous diffusion, i.e., $\delta_3 \sim \sqrt{\nu t}$ for $t < t_\nu$. A rough estimation of t_ν is given by $t_\nu^+ \approx 70$ (Moin *et al.*, 1990), such that the initial viscous growth period becomes a smaller fraction of T as Re_τ increases. For $t > t_\nu$, turbulent diffusion prevails and $\delta_3 \sim \sqrt{\nu_e t}$, where ν_e is the turbulent eddy viscosity. Assuming the mixing-length hypothesis, $\nu_e \sim u_\tau \delta_3$, then $\delta_3 \sim u_\tau t$, i.e. the spanwise boundary layer grows linearly in time regardless of $\mathrm{d}P/\mathrm{d}x_3$ in first-order approximation. The agreement of the approximation $\delta_3^+ \approx 0.445t^+$, included in figure 3(b) with δ_3, highlights the validity of the previous assumptions after the initial viscous phase. The inertial core of the channel, $\langle\cdot\rangle_\infty$, is accelerated by the mean spanwise pressure gradient such that $\rho\langle u_3\rangle_\infty \approx (\mathrm{d}P/\mathrm{d}x_3)t$, which controls the additional spanwise shear, $\partial\langle u_3\rangle/\partial x_2 \sim \langle u_3\rangle_\infty/\delta_3 \sim (\mathrm{d}P/\mathrm{d}x_3)/(\rho u_\tau)$. In summary, the sudden imposition of $\mathrm{d}P/\mathrm{d}x_3$ results in the emergence of a spanwise boundary layer diffusing upwards from the wall linearly in time, $\delta_3 \sim u_\tau t$, accompanied by an additional mean shear proportional to $\mathrm{d}P/\mathrm{d}x_3$.

The evolution of the mean Reynolds stresses is shown in figure 4. Considering that the flow is subjected to the additional strain $\partial\langle u_3\rangle/\partial x_2$, the classic theory anticipates an increase of the Reynolds stresses under the equilibrium assumption $-\langle u_i'u_j'\rangle + (1/3)\langle u_k'u_k'\rangle\delta_{ij} \propto \nu_e\langle S_{ij}\rangle$,

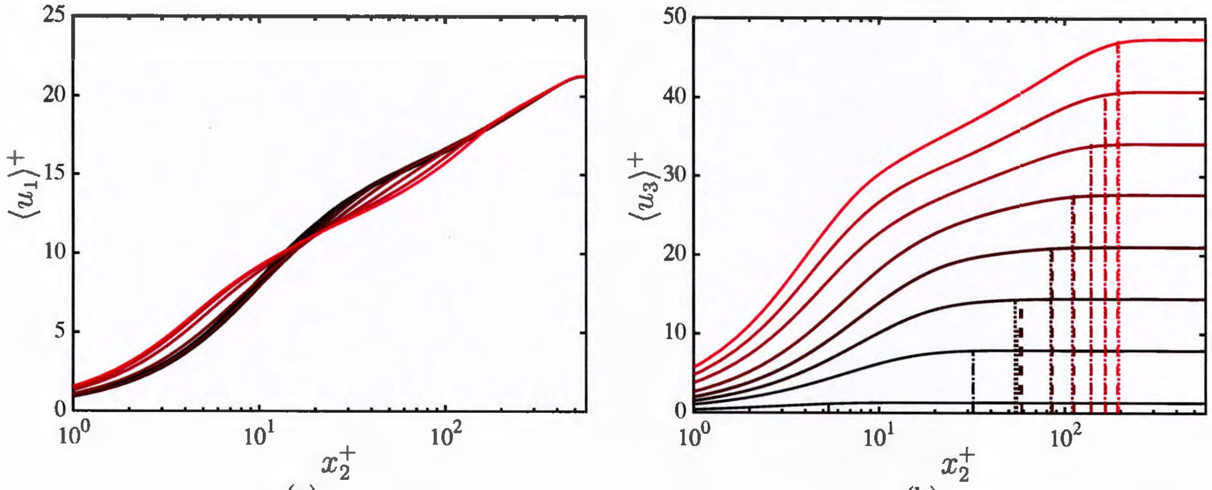

(a) (b)

Figure 3: Mean velocity profile in (a) the streamwise direction and (b) the spanwise direction for $t^+ = 12, 72, 132, 192, 252, 312, 372$, and 432. Colours indicate time from $t^+ = 0$, black, to $t^+ = 432$, red. The vertical dotted lines (········) are the boundary layer thickness δ_3 defined by the wall-normal distance at which $\langle u_3\rangle = 0.99\langle u_3\rangle_\infty = 0.99\langle u_3\rangle(h,t)$, and the vertical dashed lines (– – –) are the estimated boundary layer thickness given by $\delta_3^+ = 0.445t^+$.

where S_{ij} is the rate-of-strain tensor and δ_{ij} is the Kronecker delta. Figure 4 shows that the behaviour of $\langle u_i'u_j'\rangle$ is consistent with the equilibrium prediction for large times. However, during the first stages of the transient $\langle u_1'u_1'\rangle$ and $-\langle u_1'u_2'\rangle$ experience a vigorous depletion, whereas $\langle u_2'u_2'\rangle$ and $\langle u_3'u_3'\rangle$ remain roughly constant. Thus, the initial transient exhibits a counterintuitive behaviour of Reynolds stresses, inconsistent with the equilibrium assumption. The reduction in magnitude of those stresses comprising u_1' hints to a deficiency in the streak generation cycle triggered during the transient; the structural origin of such a deficiency is discussed in §2.3.4. A similar equilibrium argument applies to the angle of Reynolds stress direction, $\gamma_\tau = \mathrm{atan}[\langle u_2'u_3'\rangle/\langle u_1'u_2'\rangle]$, and mean shear direction $\gamma_S = \mathrm{atan}[(\partial\langle u_3\rangle/\partial x_2)/(\partial\langle u_1\rangle/\partial x_2)]$, which are expected to satisfy $\gamma_\tau \approx \gamma_S$ in an equilibrium 2DTBL. As seen from figure 5(a), the equilibrium condition is not met for the angles; the Reynolds stress direction lags behind the mean direction closer to the wall and leads further away. We will focus most of our attention on the tangential Reynolds stress, $-\langle u_1'u_2'\rangle$, because the initial non-equilibrium response is most vividly manifested on that component, although other coordinate-dependent metrics can be defined to measure non-equilibrium effects. In particular, it was assessed that the conclusions drawn below are also valid when non-equilibrium effects are quantified in terms of the classic Townsend (1976) structure parameter as shown in appendix 2.7.

It could be argued that the drop in $-\langle u_1'u_2'\rangle$ in figure 4(d) is an artefact of the static frame of reference $\mathcal{F} : (x_1, x_2, x_3)$. The direction given by $\mathcal{F}$ is no longer co-planar to the mean shear vector, which is the primal source responsible for the injection of kinetic energy into the turbulence intensities. To show that the depletion of $-\langle u_1'u_2'\rangle$ is not the consequence

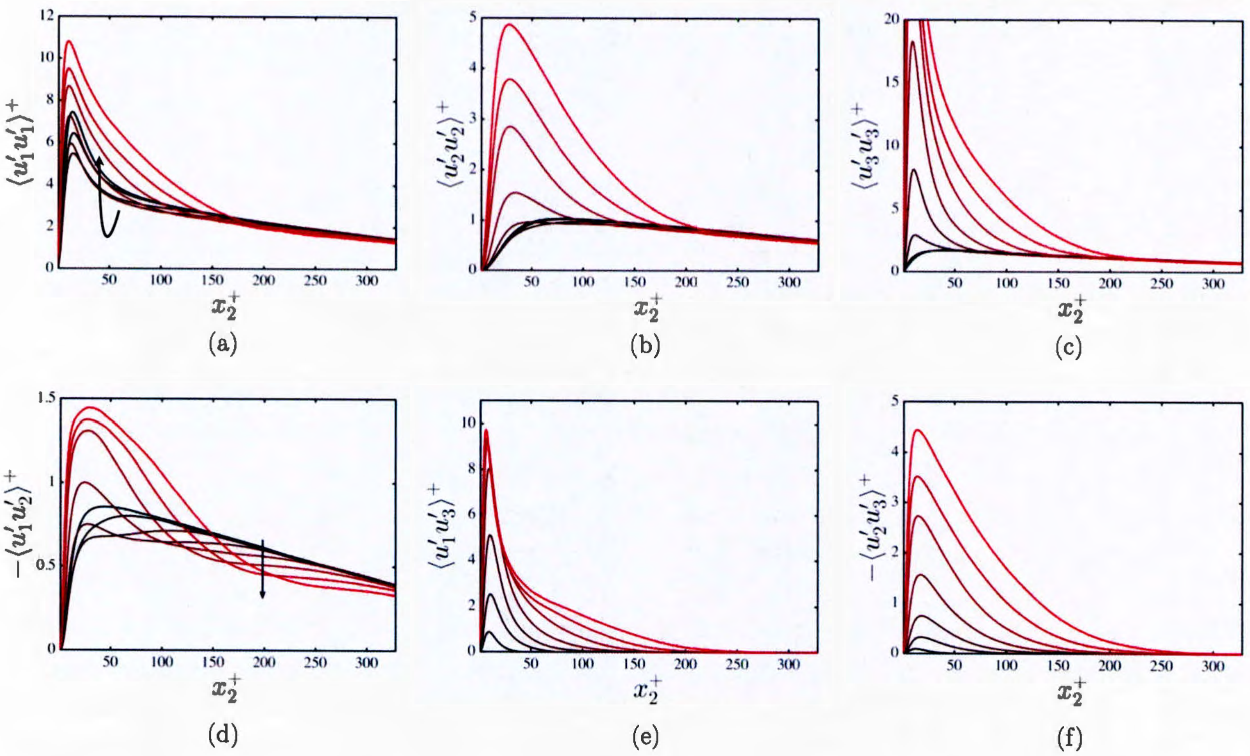

(a) (b) (c)

(d) (e) (f)

Figure 4: Mean Reynolds stress for $\Pi = 60$ at $Re_\tau \approx 500$. Different lines correspond to different times at $t^+ = 12, 72, 132, 192, 252, 312, 372$, and 432. Colours indicate time from $t^+ = 0$, black, to $t^+ = 432$, red. The arrows indicate the direction of time.

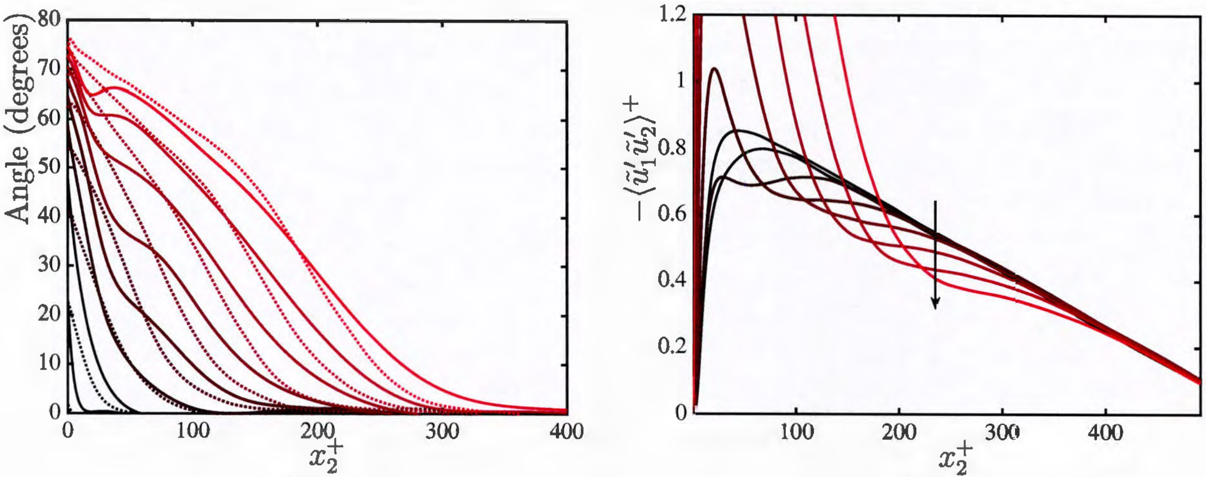

(a) (b)

Figure 5: (a) Angle of the mean Reynolds stress direction γ_τ (——) and mean shear direction γ_S (········) with respect to x_1. (b) Mean tangential Reynolds stress in the wall-normal and time-dependent frame of reference $\tilde{\mathcal{F}}$ aligned with the mean-shear direction γ_S. The arrow in panel (b) indicates the direction of time. Different lines correspond to different times at $t^+ = 12, 72, 132, 192, 252, 312, 372$, and 432. In both panels, the colours denote time from $t^+ = 0$, black, to $t^+ = 432$, red. The data is for $\Pi = 60$ at $Re_\tau \approx 500$.

of observing the flow from the point of view of $\mathcal{F}$, we define the wall-normal and time-dependent frame of reference $\tilde{\mathcal{F}} : (\tilde{x}_1, x_2, \tilde{x}_3)$ such that $\tilde{x}_1$ points in the direction of the local mean shear vector $(\partial \langle u_1 \rangle / \partial x_2, 0, \partial \langle u_3 \rangle / \partial x_2)$ at each wall-normal location and time instant. The angle between $\tilde{x}_1$ and x_1 is given by γ_S (figure 5a). The velocity components in the frame of reference $\tilde{\mathcal{F}}$ are denoted by $\tilde{u}_1$, $\tilde{u}_2 (\equiv u_2)$, and $\tilde{u}_3$. Figure 5(b) demonstrates that the shear-aligned tangential Reynolds stress, $-\langle \tilde{u}_1' \tilde{u}_2' \rangle$, also experiences a strong reduction in magnitude. An alternative frame of reference is that aligned with the principal Reynolds stress direction defined by the angle γ_τ (Moin *et al.*, 1991). The difference between γ_S and γ_τ is small (figure 5a), and the history of the Reynolds stresses in the frame of reference of the principal Reynolds stress direction (not shown) is similar to the results from figure 5(b).

2.3.2 Flow regimes

We quantify the flow regimes of the transient response of the momentum-carrying eddies (responsible for $-\langle u_1' u_2' \rangle$) subjected to non-equilibrium effects. It is assumed that the Reynolds number of the channel flow is sufficiently high to develop a multi-scale collection of randomly distributed momentum-carrying motions with their roots attached to the wall, as first conjectured by Townsend (1976) and currently supported by a growing number of studies (e.g. Davidson *et al.*, 2006; Lozano-Durán *et al.*, 2012; Hwang, 2015; Hellström *et al.*, 2016; Hwang & Bengana, 2016; Dong *et al.*, 2017; Baars *et al.*, 2017; Hwang & Sung, 2018; Yang *et al.*, 2019; Cheng *et al.*, 2019). We can anticipate that for low values of Π, the perturbation introduced by the lateral forcing is very gentle and eddies evolve in a quasi-equilibrium state irrespective of their size and lifespan. Conversely, large values of Π are expected to drive the entire population of eddies at all scales across the boundary out of equilibrium. The non-dimensional parameters governing these flow regimes are Re_τ and Π.

The level of non-equilibrium endured by the momentum-carrying eddies can be estimated by assuming that, prior to the application of Π, the boundary layer is populated by a collection of wall-attached self-similar eddies with sizes l_e proportional to the distance to the wall, $l_e \sim x_2$, and characteristic velocity u_τ (Townsend, 1976). Consequently, the characteristic lifetime of eddies of size l_e is $t_e \sim x_2/u_\tau$. The smallest momentum-carrying eddies are found close to the wall at $x_2 \sim \nu/u_\tau$ due to the limiting effect of viscosity, and their lifetimes reduce to $t_e \sim \nu/u_\tau^2$. The largest eddies are constrained by the channel height $x_2 \sim h$, with lifetimes $t_e \sim h/u_\tau$. The lateral mean pressure gradient introduces an additional time-scale associated with the spanwise acceleration of the flow $t_p \sim \rho u_\tau/(\mathrm{d}P/\mathrm{d}x_3)$. The condition for non-equilibrium is $t_p < t_e$, i.e. the characteristic time to accelerate the flow in the spanwise direction is shorter than the lifetime of the momentum-carrying eddies in order to shove the latter out of the equilibrium state. A similar conclusion is drawn by reasoning in terms of the minimum strength of the lateral shear layer $\partial\langle u_3\rangle/\partial x_2$ necessary to disturb the local-in-x_2 mean shear of the wall-attached eddies $\partial\langle u_1\rangle/\partial x_2$. The former was shown to be $\partial\langle u_3\rangle/\partial x_2 \sim (\mathrm{d}P/\mathrm{d}x_3)/(\rho u_\tau)$ in §2.3.1, while the latter can be approximated by assuming a logarithmic mean velocity profile of the form $\langle u_1\rangle \sim (u_\tau/\kappa)\log(x_2^+)$ such that $\partial\langle u_1\rangle/\partial x_2 \sim u_\tau/x_2$. Then, the lateral mean shear required to overcome the mean streamwise shear is $u_\tau/x_2 < (\mathrm{d}P/\mathrm{d}x_3)/(\rho u_\tau)$ which is equivalent to time-scale argument, $t_p < t_e$, discussed above.

Based on the flow scales discussed above, we differentiate three flow regimes as sketched in figure 6(a). For $\Pi < \mathcal{O}(1)$ ($t_p > t_e$), the spanwise pressure gradient is categorised as weak, and all flow scales relax instantly to a quasi-equilibrium state during the transient period. Conversely, for $\Pi > \mathcal{O}(Re_\tau)$ ($t_p < t_e$), the momentum-carrying eddies are unable to adjust to the prompt imposition of the shear regardless of their size. For intermediate values of Π, eddies coexist in both quasi-equilibrium and non-equilibrium states, the former being the eddies located in the region closer to the wall.

The analysis above is corroborated in figures 6(b) and (c), which show the maximum percentage drop of the tangential Reynolds stress during the transient period after the imposition of the lateral mean pressure gradient, $\min_t\{D_\tau(x_2,t)\}$, where D_τ is defined as

$$D_\tau(x_2,t) = \frac{\langle\tilde{u}_1\tilde{u}_2\rangle(x_2,t) - \langle\tilde{u}_1\tilde{u}_2\rangle(x_2,0)}{\langle\tilde{u}_1\tilde{u}_2\rangle(x_2,0)} \times 100. \tag{1}$$

Note that the Reynolds stress in (1) is referred to the frame of reference $\tilde{\mathcal{F}}$ aligned with the mean shear. Similar conclusions are drawn when the stress is referred to $\mathcal{F}$. The results in figure 6(b) reveal that the relative reduction in the Reynolds stress attains up to 30%, and that the drop accentuates for increasing Π and x_2^*. Figure 6(c) confirms that the trend holds at higher Re_τ.

The scaling of $\min_t\{D_\tau\}$ is inspected in figure 7, which contains various cuts of the (Π, x_2^*)-maps shown in figures 6(b) and (c). Within the buffer region (figure 7a), the response of the

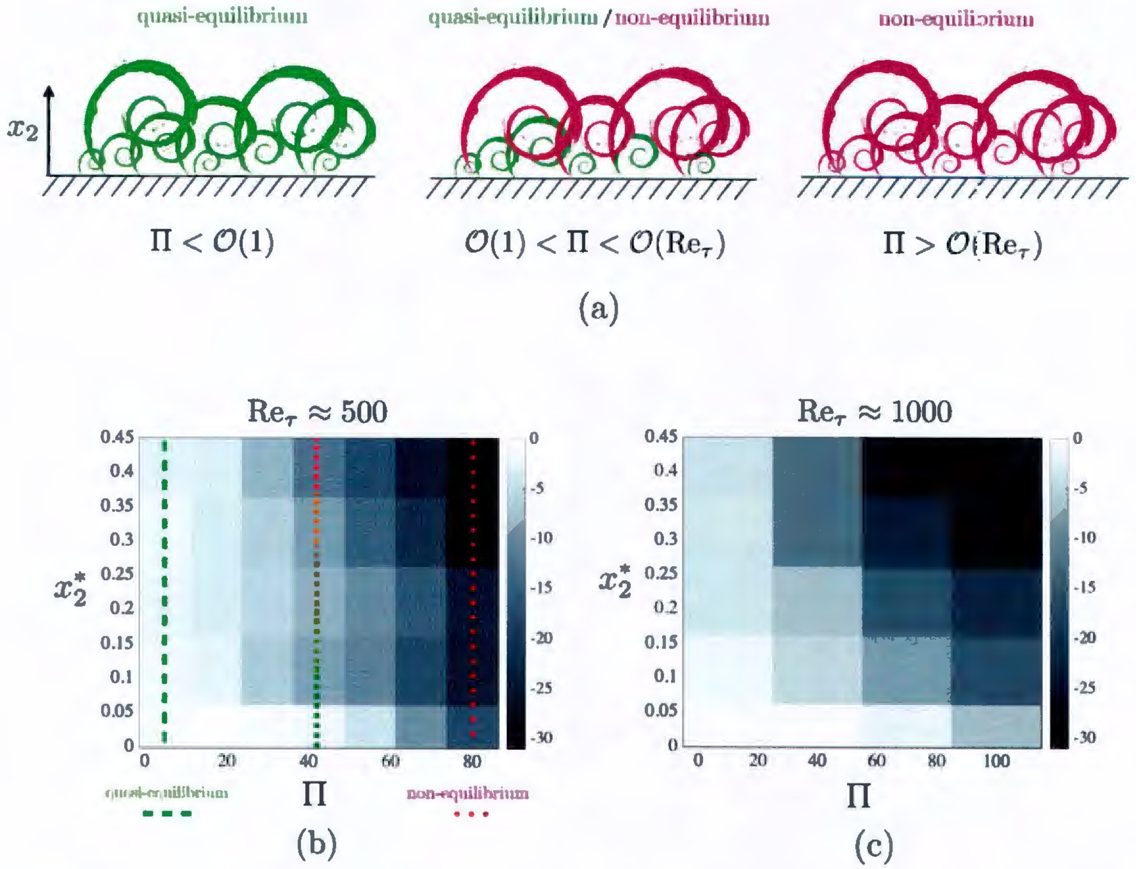

Figure 6: (a) Schematic of self-similar, wall-attached, momentum-carrying eddies, and different flow regimes as function of the spanwise to streamwise mean pressure gradient ratio Π. The eddies coloured in green are in a quasi-equilibrium state, whereas eddies coloured in red are out-of-equilibrium. Panels (b) and (c) are the percentage drop of tangential Reynolds stress, $\min_t\{D_\tau\}$, in the frame of reference of the mean shear $\tilde{\mathcal{F}}$ as a function of the spanwise to streamwise the mean pressure gradient ratio Π and wall-normal distance x_2^* for (b) $Re_\tau \approx 500$ and (c) $Re_\tau \approx 1000$. The vertical lines in (b) represent flow states ranging from the equilibrium regime (green) to non-equilibrium regime (red).

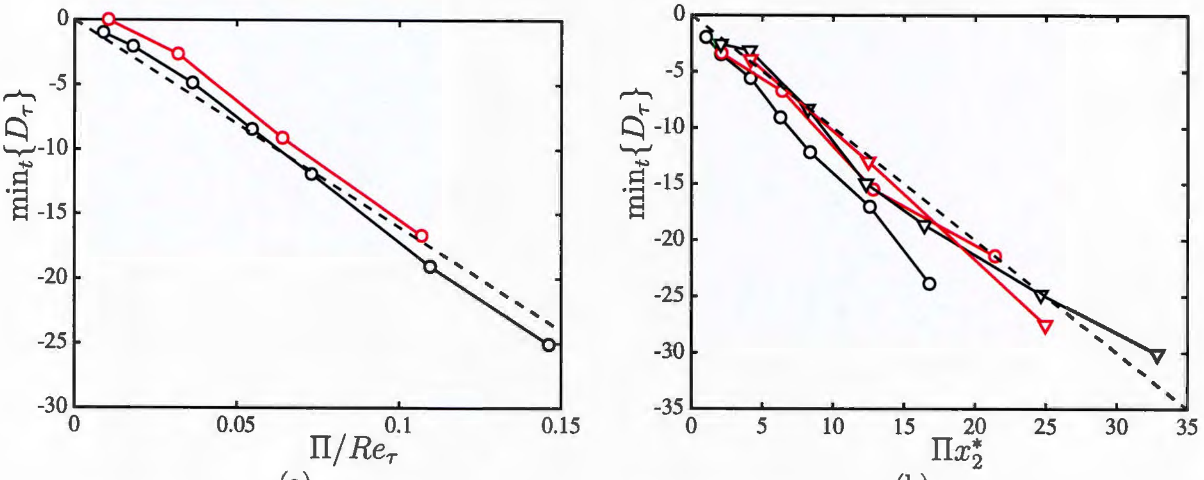

(a) (b)

Figure 7: Maximum percentage drop of the tangential Reynolds stress $\min_t\{D_\tau\}$ in the frame of reference of the mean shear. Colours are black for cases at $Re_\tau \approx 500$ and red for cases at $Re_\tau \approx 1000$. In panel (a), lines with (○) are $\min_t\{D_\tau\}$ at $x_2^+ = 30$, and (−−−) is $\min_t\{D_\tau\} \approx -160\Pi/Re_\tau$. In panel (b), lines with symbols are $\min_t\{D_\tau\}$ at $x_2^* = 0.2$ (○) and $x_2^* = 0.4$ (▽), and (−−−) corresponds to $\min_t\{D_\tau\} \approx -\Pi x_2^*$.

flow is controlled by the viscous scales. The momentum equation in inner units is given by

$$\frac{\mathcal{D}u_i^+}{\mathcal{D}t^+} = -\frac{\partial p'^+}{\partial x_i^+} - \frac{\mathrm{d}P^+}{\mathrm{d}x_i^+}\delta_{i3} + \frac{\partial^2 u_i^+}{\partial x_k^+ \partial x_k^+}, \tag{2}$$

where $\mathcal{D}$ denotes material derivative and $\mathrm{d}P^+/\mathrm{d}x_1^+ = \mathcal{O}(1/Re_\tau)$ has been neglected. From (2), we conclude that a similar reduction in the Reynolds stress is obtained across different Re_τ for identical values of $\mathrm{d}P^+/\mathrm{d}x_3^+ = \Pi/Re_\tau$, which is the relevant spanwise to streamwise mean pressure gradient for the buffer region.

For the logarithmic layer, for which the high Re_τ analysis holds (figure 7b), wall-attached eddies of a given size $l_e \sim x_2$ experience a similar drop in the Reynolds stress when the mean spanwise pressure gradient is normalised by the characteristic scales, x_2 and u_τ, controlling the eddies. Analysis of the nondimensional equations obtained by introducing the similarity variable $\eta = t/t_e = tu_\tau/x_2$ reveals that the condition for self-similar Reynolds stress depletion at a given wall-normal distance is obtained by a common value of the compensated spanwise to streamwise mean pressure gradient ratio, Πx_2^*, consistent with the results from figure 7(b).

From the scaling analysis above and the numerical results in figure 7, the quantitative drop in Reynolds stress for the flow motions free of viscous effects at a given x_2 location is well approximated by

$$\min_t\{D_\tau\} \approx -\Pi x_2^*. \tag{3}$$

If we further assume that the self-similar scaling of the flow motions with x_2 does not hold below $x_2^+ \approx 160$, the inner-layer scaling law for the Reynolds stress decrease implied by (3) is

$$\min_t\{D_\tau\} \approx -160\frac{\Pi}{Re_\tau}, \tag{4}$$

which is valid for the buffer region and serves as an approximation to the trends observed in figure 7(a).

Finally, a tentative relation delimiting the necessary spanwise forcing to achieve the fully non-equilibrium regime (eddies out of equilibrium across almost the entire boundary layer), arbitrarily delimited by $\min_t\{D_\tau\} < -5\%$, is given by

$$\Pi > 0.03 Re_\tau. \tag{5}$$

Equation (5) shows that the lateral mean pressure gradient required to attain the fully non-equilibrium regime increases proportionally to the Reynolds number. Note that (5) is a non-equilibrium condition for $x_2^+ > 30$. Prescribing a lower wall-normal limit would result in an even more stringent condition than (5). The meaning of Π in this particular flow cannot be unambiguously extrapolated to more general flows configurations. Nonetheless, the time-scale argument used to derived (5) suggests that, in external aerodynamic applications, the inner layer is most likely to be found in a quasi-equilibrium state given the high Reynolds numbers typically encountered in these situations.

2.3.3 Evolution of the tangential Reynolds stress

In the previous section we were concerned with the maximum drop in the tangential Reynolds stress without consideration of its time response. Here, we discuss the scaling of the evolution of D_τ for 3-D channels in the fully non-equilibrium regime, i.e., $\Pi > 0.03Re_\tau$, which is the most intriguing case from the physical viewpoint. As in §2.3.2, we perform the analysis separately for the buffer region and logarithmic layer, although the former can be thought of as the near-wall limit of the latter.

The evolution of D_τ in the buffer layer is plotted in figure 8 for various pairs of (Re_τ, Π). Three scalings are inspected. Figure 8(a) shows the evolution of D_τ as a function of time normalised in outer units. Unsurprisingly, both the intensity of D_τ and the time instant for the maximum drop varies considerably among distinct combinations of (Re_τ, Π). Inasmuch as the near-wall eddies do not scale in outer units, the results in figure 8(a) are included only to expose the lack of collapse among cases under an inadequate normalisation. The time-scaling using wall units is tested in figure 8(b). It was argued in §2.3.2 that the depletion of Reynolds stress within the inner layer is proportional to Π/Re_τ. Consequently, the results in figure 8(b) are plotted against the compensated Reynolds stress drop, $D_\tau Re_\tau/\Pi$. The new scaling improves the collapse of the results, especially for $t^+ < 150$, above which the evolution of $D_\tau Re_\tau/\Pi$ diverges among cases. The absence of collapse for $t^+ > 150$ coincides with the typical lifetime of the momentum-carrying eddies in the buffer layer (Lozano-Durán & Jiménez, 2014*b*). Thus, u_τ (defined at $t = 0$) is representative of the originally-in-equilibrium near-wall eddies until the generation cycle is restarted and newborn eddies emerge under different flow conditions. Following the previous reasoning, the collapse can be further improved under the assumption that the length and time scales of the newly created eddies

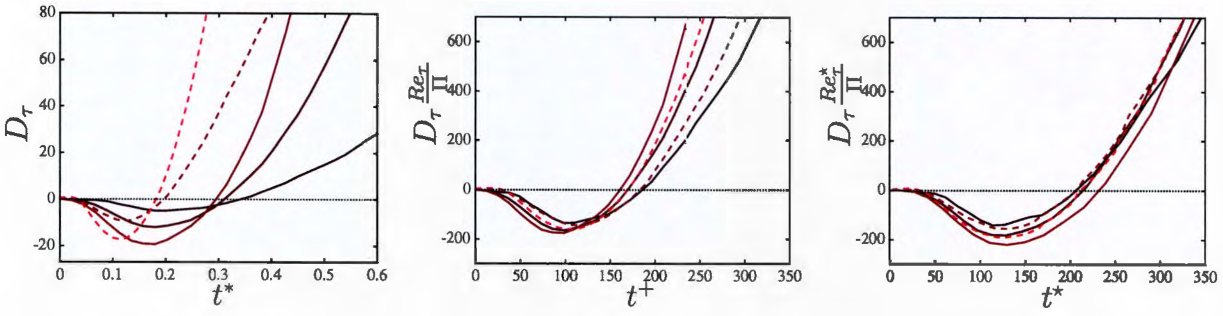

(a) (b) (c)

Figure 8: Evolution of the percentage change of tangential Reynolds stress D_τ in the buffer layer for $x_2^+ = 30$ in panels (a) and (b), and for $x_2^\star = 30$ in panel (c). The lines are (——) for $Re_\tau \approx 500$ and (– – –) for $Re_\tau \approx 1000$. For cases at $Re_\tau \approx 500$, colours are $\Pi = 20, 40$, and 60 from dark red to light red. For cases at $Re_\tau \approx 1000$, colours are dark red for $\Pi = 60$ and light red for $\Pi = 100$.

are controlled by the local-in-time friction velocity

$$u_\tau^{\star 2}(t) = \sqrt{\left(\nu \frac{\partial \langle u_1 \rangle}{\partial x_2}\right)^2 + \left(\nu \frac{\partial \langle u_3 \rangle}{\partial x_2}\right)^2}\Bigg|_{x_2=0}. \tag{6}$$

The local wall units, denoted by $(\cdot)^\star$, are analogously defined in terms of ν and $u_\tau^\star(t)$, and the local friction Reynolds number is $Re_\tau^\star(t) = u_\tau^\star(t)h/\nu$. The results in figure 8(c) confirm that the local scaling ($t^\star$ versus $D_\tau Re_\tau^\star/\Pi$) holds for longer times.

The evolution of D_τ for the momentum-carrying eddies across the logarithmic layer is shown in figure 9, where three scaling laws are investigated. The evolution of D_τ in outer units is include in figure 9(a). Wall-attached eddies follow an ordered response in time after the sudden imposition of the transverse pressure gradient: eddies closer to the wall react earlier and are the least perturbed, while larger eddies experience a more acute Reynolds stress reduction at later times. The preceding analysis for the buffer region is extended to the logarithmic layer by taking into consideration that the lifetimes of the wall-attached eddies scale as $\sim x_2/u_\tau$, with a consistent drop in the Reynolds stress proportional to $\Pi x_2^\star$. The self-similar response of wall-attached eddies under the lateral force is evidenced by the improved collapse in figure 8(b), at least for $tu_\tau/x_2 \lesssim 1$. Analogously to the inner layer, u_τ stands as the characteristic velocity scale of the original eddies in the equilibrium state, but does not hold as such for times longer than the lifespan of individual wall-attached eddies, $tu_\tau/x_2 \approx 1$ (Lozano-Durán & Jiménez, 2014*b*). The collapse among cases is perfected by using the local time-scale $tu_\tau^\star/x_2$ (figure 8c), which accounts for variations in the momentum transfer controlling the eddies during the transient. We close the section by highlighting that the scaling properties of the flow studied above are conspicuous only at moderate/high Reynolds numbers. The response of the flow at lower Reynolds numbers is discussed in appendix 2.5, where it is shown that 3-D channels at $Re_\tau \approx 180$ lack the necessary scale separation to exhibit a multiscale depletion of the Reynolds stress.

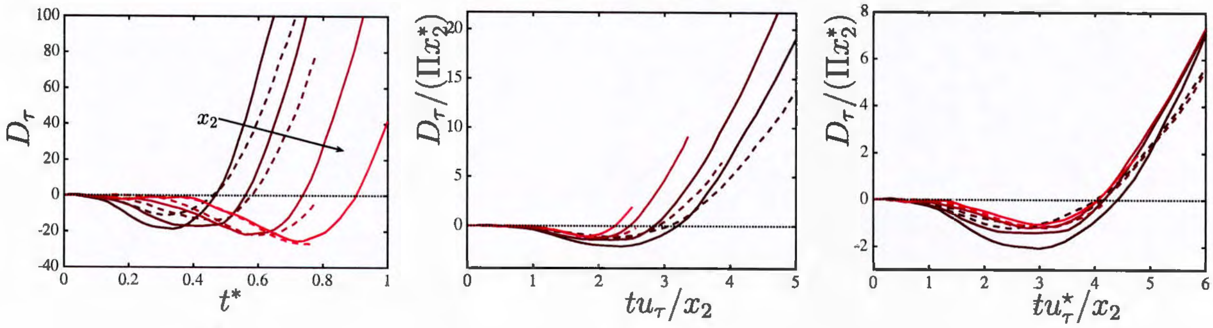

(a) (b) (c)

Figure 9: Evolution of the percentage change of tangential Reynolds stress D_τ in the logarithmic layer for $x_2^* = 0.15, 0.2, 0.3$, and 0.4 represented by lines coloured from dark red to light red. Lines are (——) for cases at $Re_\tau \approx 500$ and (- - -) for cases at $Re_\tau \approx 1000$, both for $\Pi = 60$. The arrow in panel (a) indicates increasing wall-normal distance.

2.3.4 Structural changes in the conditionally averaged flow field

We examine the structural evolution of the flow in the surroundings of the momentum-carrying eddies. To that end, we identify three-dimensional structures of the intense momentum transfer using the methodology introduced by Lozano-Durán *et al.* (2012) (see also Lozano-Durán & Jiménez, 2014*b*; Lozano-Durán & Borrell, 2016). An individual structure (or object) of intense momentum transfer at time t is defined as a spatially connected region in the flow satisfying

$$-u_1'(x_1, x_2, x_3, t)u_2'(x_1, x_2, x_3, t) > H\langle u_1'^2\rangle^{1/2}(x_2, t)\langle u_2'^2\rangle^{1/2}(x_2, t), \qquad (7)$$

where H is a thresholding parameter (hyperbolic-hole size, Bogard & Tiederman, 1986) equal to 1.75 obtained following the analysis by Moisy & Jiménez (2004). It was tested that varying H within the range $0.5 < H < 3$ does not change the conclusions below. The original frame of reference defined by $\mathcal{F}$ is preferred to $\tilde{\mathcal{F}}$ in order to avoid artificial distortions in the flow due to the time and space variations in $\tilde{\mathcal{F}}$. Hereafter, we refer to individual structures of intense $-u_1'u_2'$ events as $-u_1'u_2'$-structures. Numerically, three-dimensional structures are constructed by connecting neighbouring grid points fulfilling (7) and using the 6-connectivity criteria (Rosenfeld & Kak, 1982). Figure 10 shows the wall-attached $-u_1'u_2'$-structures identified before and after the imposition of the spanwise pressure gradient. Figure 10 also includes one individual $-u_1'u_2'$-structure highlighted by the box with red edges.

We focus our attention on the channel at $Re_\tau \approx 1000$ and $\Pi = 60$, but similar results are obtained consistently across different Re_τ and Π, provided that the latter is large enough to attain the fully non-equilibrium regime. We select three time instants to assess the structural changes in the flow, namely, $t^* = 0$, $t^* = 0.25$, and $t^* = 0.50$. The evolution of D_τ is plotted in figure 11(a), which shows that the maximum drop in the tangential Reynolds stress occurs at $t^* \approx 0.50$.

The identification procedure above yields about 10^5 structures at each time instant after

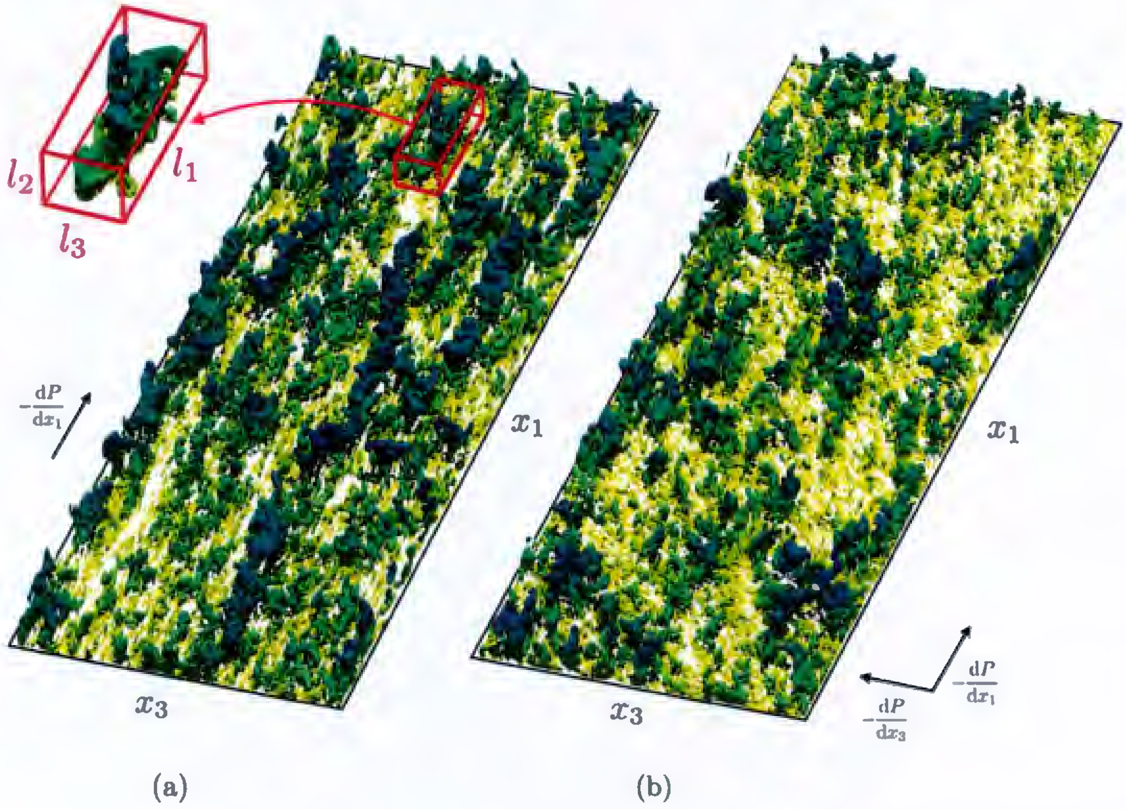

Figure 10: Instantaneous $-u_1'u_2'$-structures defined by (7) for $\Pi = 60$ and $Re_\tau \approx 1000$ at (a) $t^* = 0$ and (b) $t^* = 0.5$. Only $-u_1'u_2'$-structures attached to the bottom wall are shown. The colours represent the distance to the wall from yellow (closer to the wall) to blue (farther from the wall). The box with edges coloured in red is the bounding box of one individual $-u_1'u_2'$-structure with streamwise, wall-normal, and spanwise sizes equal to l_1, l_2, and l_3, respectively.

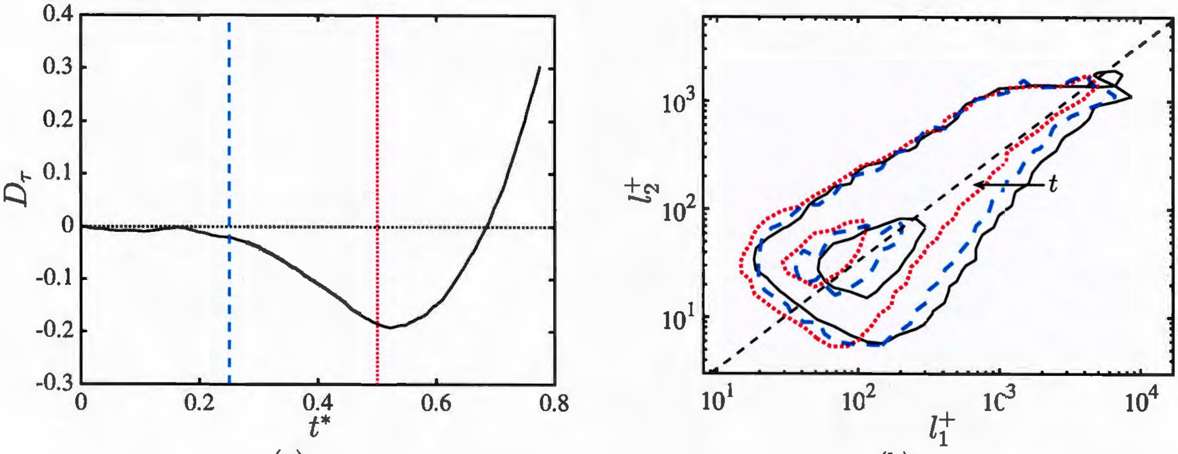

(a) (b)

Figure 11: (a) Evolution of the percentage change of tangential Reynolds stress D_τ at $x_2^* = 0.25$. The vertical lines are the times selected to study the flow structure in addition to $t^* = 0$, namely $t^* = 0.25$ (– – –) and $t^* = 0.5$ (········). (b) Joint probability density functions of the logarithms of the streamwise l_1 and wall-normal l_2 sizes of wall-attached $-u_1'u_2'$-structures, $p(l_1^+, l_2^+)$. The contours plotted contain 50% and 99.8% of the probability. The lines are (——) for $t^* = 0$, (– – –) for $t^* = 0.25$, and (········) for $t^* = 0.5$. The straight dashed line is $l_1^+ = 3l_2^+$ and the arrow indicates the direction of time. The results are for $Re_\tau \approx 1000$ and $\Pi = 60$.

discarding those objects with volumes smaller than 30^3 wall units. The sizes of the objects are measured by circumscribing each structure within a box aligned to the Cartesian axes, whose streamwise, wall-normal, and spanwise sizes are denoted by l_1, l_2, and l_3, respectively. The minimum and maximum distances of each object to the closest wall are $x_{2,\mathrm{min}}$ and $x_{2,\mathrm{max}}$, respectively, and such that $l_2 = x_{2,\mathrm{max}} - x_{2,\mathrm{min}}$. An example of an individual $-u_1'u_2'$-structure and its bounding box is included in figure 10(a). The bounding boxes of the structures are aligned with the original flow direction. At $t^* = 0.5$, the mean shear at the centre of gravity of a $-u_1'u_2'$-structure of size $x_2^* \approx 0.4$ is rotated by $\gamma_S \approx 15$ degrees (see also figure 10b). This low turning angle justifies the selection of $\mathcal{F}$ to study the flow for short times, as it is the case here, but the investigation of structural changes for longer times would require a properly chosen rotating frame of reference. We centre our attention on wall-attached $-u_1'u_2'$-structures, defined as those with $x_{2,\mathrm{min}}^+ < 25$ (Del Álamo *et al.*, 2006). For the value of H selected, wall-attached structures are responsible for more than 60% of the tangential Reynolds stress at all three times considered. Figure 11(b) shows the joint probability density function (p.d.f.) of the sizes of the wall-attached structures, $p(l_1^+, l_2^+)$. At $t^* = 0$, the distribution of sizes is consistent with a geometrically self-similar population of structures akin to the wall-attached eddies envisioned by Townsend (1976) at high Reynolds numbers. The mode of the p.d.f. follows a reasonably well-defined linear law, $l_1 \sim 3l_2$ consistent with previous studies (Lozano-Durán *et al.*, 2012). From $t^* = 0$ to $t^* = 0.50$, the most pronounced modification in the geometry of the structures is a gradual shortening of their streamwise length, while their wall-normal heights are barely affected.

Each $-u_1'u_2'$-structure can be classified as either an ejection, when the average wall-normal velocity within its enclosed volume is positive, or as a sweep otherwise. Sweeps and ejections are known to be spatially organised in pairs side-by-side along the spanwise direction (Ganapathisubramani, 2008; Lozano-Durán *et al.*, 2012; Wallace, 2016; Osawa & Jiménez, 2018). This sweep-ejection group, representative of a streamwise roll, is the predominant logarithmic-layer flow structure responsible for the generation of tangential Reynolds stress. Consequently, we are interested in examining the modification of the flow around sweep-ejection pairs during the transient period. We denote the centre of gravity of the bounding boxes of the n-th sweep and its paring ejection as $\boldsymbol{x}_s^n$ and $\boldsymbol{x}_e^n$, respectively. The wall-normal size of the sweep is $l_{2,s}^n$ and of the ejection $l_{2,e}^n$. The averaged flow field conditioned to the presence of a sweep-ejection pair is computed by averaging the velocity vector in a rectangular domain along different n-th pairs, whose centre coincides with $\boldsymbol{x}_p^n = (\boldsymbol{x}_e^n + \boldsymbol{x}_s^n)/2$, and it edges are $\boldsymbol{r}$ times the average wall-normal height $l_p^n = (l_{2,e}^n + l_{2,s}^n)/2$. Then, the conditionally averaged flow around sweep-ejection pairs is given by

$$\{u_i'\}(\boldsymbol{r}) = \sum_{n=1}^{N} \frac{u_i'(\boldsymbol{x}_p^n + l_p^n \boldsymbol{r})}{N}, \tag{8}$$

where $n = 1, .., N$ is the set of sweep-ejection pairs selected to perform the conditional average, and $\boldsymbol{r} = (r_1, r_2, r_3)$. We also take advantage of the spanwise symmetry of the flow, and r_3 is always chosen to be positive towards the sweep. The reader is referred to Lozano-Durán *et al.* (2012) and Dong *et al.* (2017) for additional details on the procedure to obtain conditional flow fields.

The averaged flow field conditioned to sweep-ejection pairs with $0.2 < l_p^{n*} < 0.3$ is plotted in figure 12. At $t^* = 0$ (figure 12a), the characteristic flow structure consistent with the statistically-in-equilibrium flow state is a streamwise roll flanked by one low-velocity streak and one high-velocity streak. At succeeding times (figure 12b,c), the roll persist, while the intensity and size of the low-velocity streak have already decreased at $t^* = 0.5$. The high-velocity streaks and roll are also weakened, but the variations are less pronounced. Another observation is the loss of coherence in a developing layer underneath the low-velocity streak. This effect is demonstrated by the low values of $\{u_1'\}$ represented by the green regions below the white dashed lines in the figure 12 (right panels). The nearly zero averaged streamwise velocity for $t^* > 0$ is an indication that, from the viewpoint of the larger rolls, the fluid motions below cancel out and are perceived as incoherent. During the transient, both low- and high-velocity streaks shorten in the streamwise direction in accordance with the geometric analysis in figure 11(b). Although not shown, the results above are also applicable to sweep-ejection pairs across different ranges of l_p^n when the times are appropriately scaled by $l_p^n/u_\tau^\star$, implying that the modifications in the flow are self-similar in space and time.

The message from figure 13 is that the main structural alteration during the transient is the weakening of the low-velocity streaks, which is in turn associated with the loss of coherence of the flow within a growing layer underneath the streamwise rolls. The aforementioned loss of coherence may be attributed to (i) the relative displacement of wall-parallel layers at different heights and (ii) the additional mean spanwise shear which enhances the generation of smaller-scale momentum-carrying eddies (as shown by Mizuno & Jiménez (2011); Jiménez (2018); Lozano-Durán & Bae (2019)). This is illustrated in figure 13, which contains the instantaneous streamwise velocity at two wall-normal distances; one closer to the wall at $x_2^* = 0.1$ influenced by the additional shear from the lateral boundary layer, and another farther from the wall at $x_2^* = 0.3$ still unaffected.

2.3.5 Structural model

On the basis of the above observations, we propose a conceptual model that accounts for the changes undergone by the flow. The model is sketched in figure 14. The key elements are the low- and high-velocity streaks and their relative alignment with respect to the streamwise roll. Although the flow can be conceptually divided into streaks and rolls, both are interdependent flow entities which interact in a self-sustaining cycle (Waleffe, 1997; Jiménez & Pinelli, 1999; Hwang & Cossu, 2011; Cossu & Hwang, 2017; Lozano-Durán *et al.*, 2020*a*). At a given wall-normal distance x_2 and $t = 0$, the flow is configured in an equilibrium array of rolls and streaks with their centres at x_2, sizes $2x_2$, and lifetimes $2x_2/u_\tau$ (Lozano-Durán & Jiménez, 2014*b*). The tangential Reynolds stress $\langle u_1'u_2'\rangle$ at x_2 is the result of the wall-normal momentum transport conducted by the rolls and the arrangement of streaks in the equilibrium state. The momentum transfer at $t = 0$ can be modelled as the sum of two contributions,

$$\begin{aligned} \langle u_1'u_2'\rangle(x_2, t=0)^{\mathrm{model}} &\approx (u_1'^S u_2'^R)_{\mathrm{top}} + (u_1'^S u_2'^R)_{\mathrm{bot}} && (9)\\ &\approx (u_\tau)(-u_\tau/2) + (-u_\tau)(u_\tau/2) \approx -u_\tau^2, && (10)\end{aligned}$$

where $(u_1'^S u_2'^R)_{\mathrm{top}}$ represents the wall-normal transport of the high-velocity streak, $u_1'^S \approx u_\tau$, by the downward motion of the roll, $u_2'^R \approx -u_\tau/2$, above x_2. Conversely, $(u_1'^S u_2'^R)_{\mathrm{bot}}$ is the

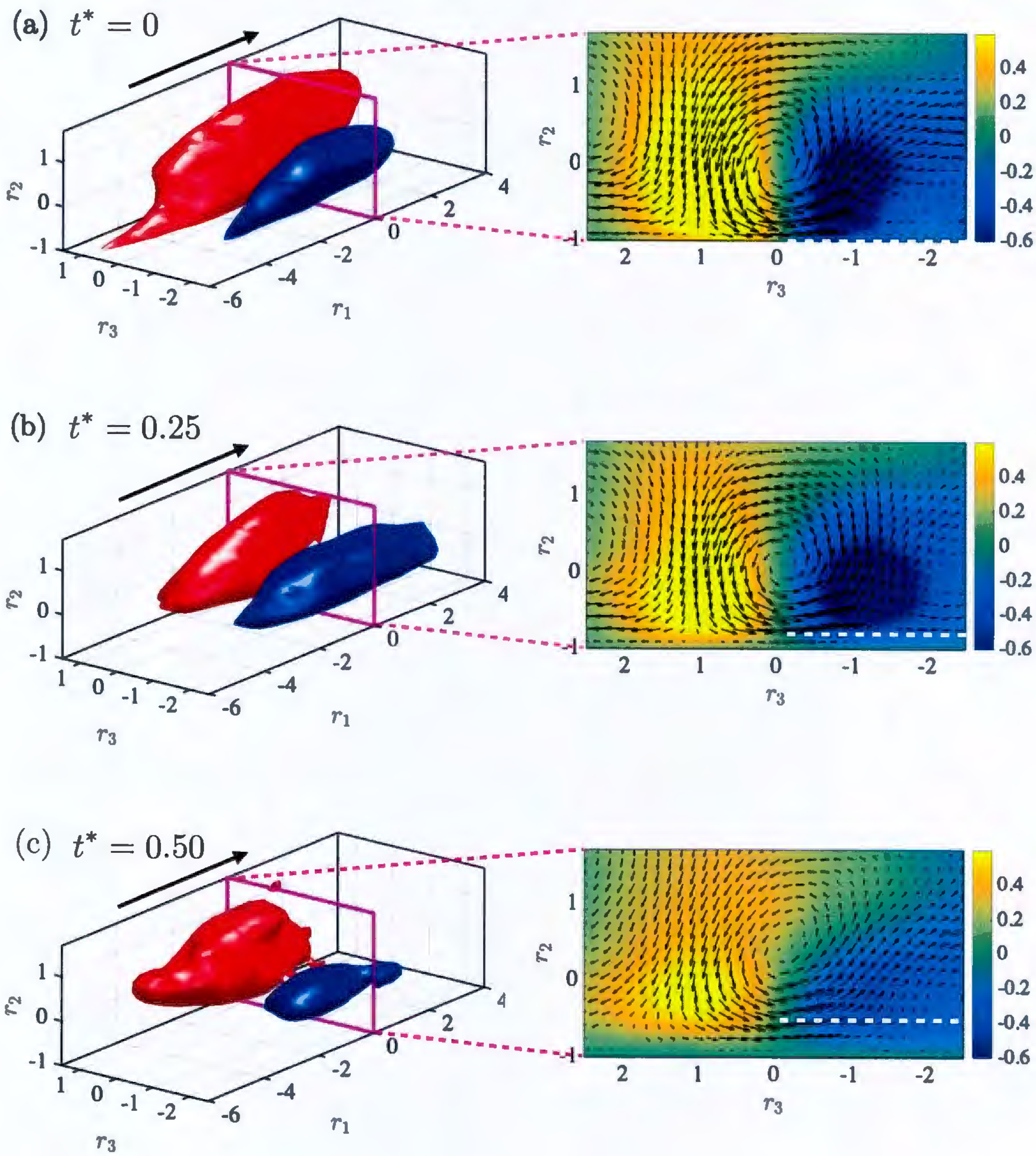

Figure 12: Averaged flow fields conditioned to wall-attached pairs of sweeps and ejections with wall-normal sizes in the range $0.2 < l_p^{n*} < 0.3$ at (a) $t^* = 0$, (b) $t^* = 0.25$, and (c) $t^* = 0.50$. Panels on the left contain isosurfaces of the low- (blue) and high- (red) velocity streaks defined by $\pm\alpha$ of the maximum positive and negative, respectively, fluctuating streamwise velocity of the average flow with (a) $\alpha = 0.6$, (b) $\alpha = 0.55$, and (c) $\alpha = 0.43$. The arrows indicate the mean flow direction. Panels on the right display the cross-flow velocity vector field $(\{u_2'\}, \{u_3'\})$ (arrows) and the fluctuating velocity $\{u_1'\}$ (colours). The dashed white line shows the wall-normal extension from the wall of the incoherent streamwise velocity field represented by low values of $\{u_1'\}$ in green. Velocities are normalised by u_τ. Results are for $\Pi = 60$ at $Re_\tau \approx 1000$.

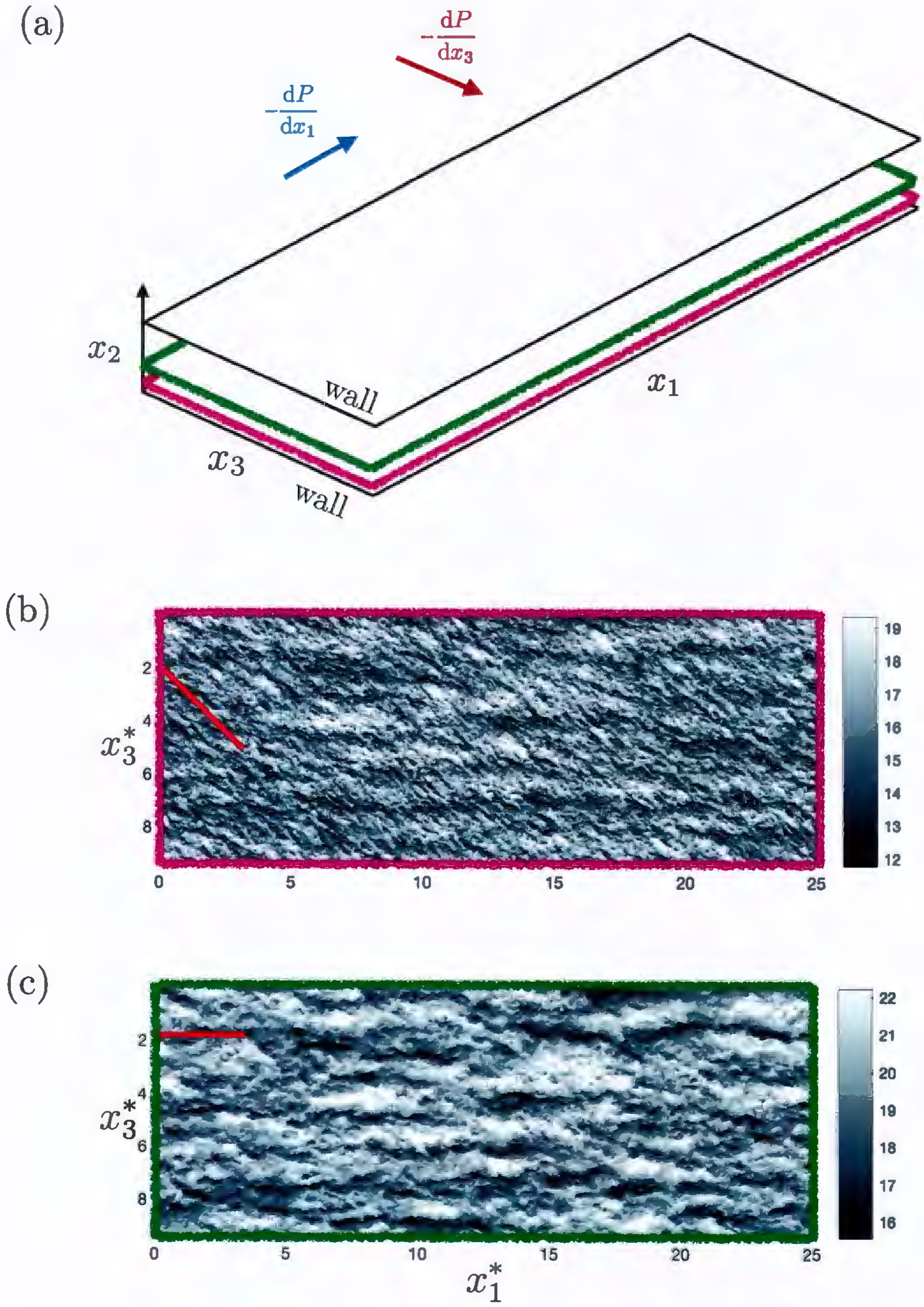

Figure 13: (a) Schematic of the channel flow domain with the wall-normal planes shown in panels (b) and (c). Panels (b) and (c) contain the streamwise velocity at (b) $x_2^* = 0.1$ and (c) $x_2^* = 0.3$ at the same time instant $t^* = 0.5$ for $\Pi = 60$ at $Re_\tau \approx 1000$. The red straight lines in (b) and (c) indicate the mean flow direction. Velocities are normalised by u_τ.

wall-normal transport of the low-velocity streak, $u_1'^R \approx -u_\tau/2$, by the upward motion of the roll, $u_2'^R \approx u_\tau$, below x_2. The intensities of $u_1'^S$ and $u_2'^R$ are adjusted to produce a total momentum transfer equal to $-u_\tau^2$, although the discussion is extensive to other values.

At half the lifespan of the eddies $t \approx x_2/u_\tau$, the spanwise boundary layer extends up to $\delta_\nu \approx 0.445x_2$, based on the estimations in §2.3.1, and remains below the centre of the rolls located at x_2. Simultaneously, the upper flow is laterally displaced by $\Delta_r \approx (1/\rho)(\mathrm{d}P/\mathrm{d}x_3)(x_2/u_\tau)^2$. For values of Δ_r larger than the spanwise coherence of the roll-streak structure, namely $\Delta_r > 2x_2$, the centre of the rolls is misaligned with the underneath streaks within the lateral boundary layer. The latter streaks are also altered by $\partial\langle u_3\rangle/\partial x_2$, which increases the local Reynolds number and triggers the emergence of smaller scales (as discussed in §2.3.4, figure 13). These changes originate a new flow configuration which is less efficient in producing $-\langle u_1'u_2'\rangle$ compared to the equilibrium state. The rationale behind such a reduction is a loss of flow coherence underneath the rolls, as supported by figure 12, which weakens the vertical momentum transported by the rolls from the layers closer to the wall. The new momentum transfer at $t \approx x_2/u_\tau$ can be modelled similarly to (9) by assuming that $(u_1'^S u_2'^R)_{\mathrm{top}}$ is barely affected, whereas $(u_1'^S u_2'^R)_{\mathrm{bot}}$ provides a deficient momentum transfer such that

$$\begin{aligned}\langle u_1'u_2'\rangle(x_2, t = x_2/u_\tau)^{\mathrm{model}} &\approx (u_1'^S u_2'^R)_{\mathrm{top}} - (u_1'^S u_2'^R)_{\mathrm{bot}} \qquad (11)\\ &\approx (u_\tau)(-u_\tau/2) + (-u_\tau\lambda)(u_\tau/2) \approx -\frac{u_\tau^2}{2}(1+\lambda), \qquad (12)\end{aligned}$$

where λ is a damping factor accounting for the reduction in the Reynolds stress generation due to the loss of streak coherence within the lateral boundary layer. The functional form of λ is modelled by assuming that the loss of streak coherence is, in first order approximation, linearly proportional to the relative spanwise mean shear,

$$\lambda = 1 - \frac{\partial\langle u_3\rangle/\partial x_2}{\partial\langle u_1\rangle/\partial x_2}, \qquad (13)$$

such that $\langle u_1'u_2'\rangle = -u_\tau^2$ for $\partial\langle u_3\rangle/\partial x_2 = 0$. If we consider the approximations $\partial\langle u_3\rangle/\partial x_2 \approx \mathrm{d}P/\mathrm{d}x_3/(\rho u_\tau)$ and $\partial\langle u_1\rangle/\partial x_2 \approx u_\tau/(2x_2)$ (see §2.3.1), then

$$\langle u_1'u_2'\rangle(x_2, t = x_2/u_\tau)^{\mathrm{model}} \approx -u_\tau^2\left(1 - \frac{x_2\mathrm{d}P/\mathrm{d}x_3}{\rho u_\tau^2}\right). \qquad (14)$$

Equation (14) can be re-arranged as $\min_t\{D_\tau^{\mathrm{model}}\} \approx -\Pi x_2^*$, which coincides with the maximum Reynolds stress depletion from (3).

Additionally, the model above predicts that the condition for non-equilibrium of flow structures at height x_2 is given by $\Delta_r > 2x_2$, which in non-dimensional form yields $\Pi x_2^* > 2$. In order to disturb the wall-parallel layers at all heights across the boundary layer, x_2^* should be fixed in wall units and such that $\Pi > \mathcal{O}(Re_\tau)$, also consistent with the estimation of $\Pi > 0.03Re_\tau$ provided in §2.3.2.

The scenario promoted above is self-similar: the continuous depletion in time of the Reynolds stress in figure 5(b) is the result of the time-ordered disruption of streaks and rolls from their natural equilibrium by the growth of the spanwise boundary layer. The

(a) $t = 0$

Equilibrium roll-streak configuration

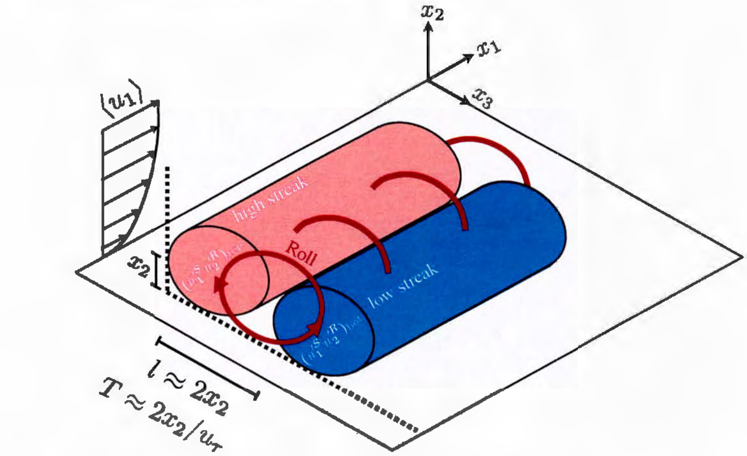

(b) $t \approx x_2/u_\tau$

Roll-streak configuration and additional shear layer underneath

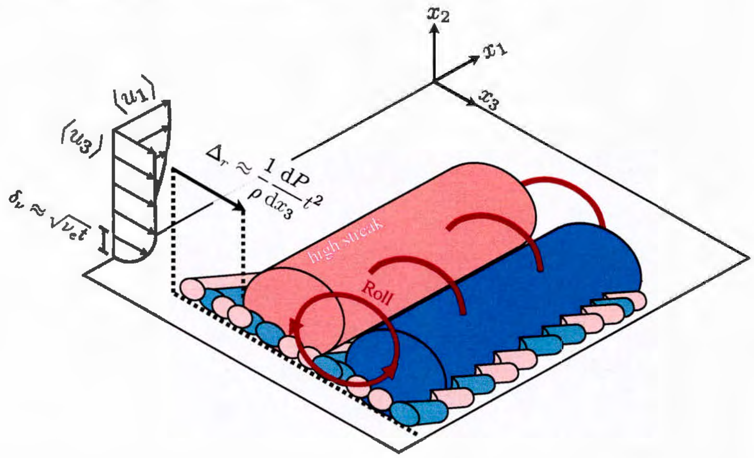

Figure 14: Structural model of self-similar wall-attached eddies subjected to a sudden mean spanwise pressure gradient. The figure shows one building block structure which comprises a streamwise roll flanked by one low-velocity streak and one high-velocity streak. Note that the complete flow field consist of the superposition of multiple building block structures of different sizes. (a) Statistically in equilibrium wall-attached momentum-carrying eddies of size $2x_2$ at $t = 0$ generating a momentum transfer $\approx -u_\tau^2$. (b) Non-equilibrium wall-attached momentum-carrying eddies at $t = x_2/u_\tau$ after the imposition of a transverse mean pressure gradient generating a momentum transfer $\approx -u_\tau^2/2(1+\lambda)$. In panel (a), $(u_1'^S u_2'^R)_{\text{top}}$ and $(u_1'^S u_2'^R)_{\text{bot}}$ represent the downward and upward, respectively, wall-normal momentum transfer by the streamwise roll. In panel (b), δ_ν is the spanwise boundary layer thickness and Δ_r is the lateral displacement of the flow above δ_ν due to the uniform acceleration $(1/\rho)\mathrm{d}P/\mathrm{d}x_3$ imposed by the mean spanwise pressure gradient. The smaller-scale low- and high-velocity streaks underneath the larger roll in panel (b) represent the incoherent fluid motions discussed in §2.3.4 (figures 12b,c) and visualised in figure 13(b). At $t = 0$, the flow also contains smaller streamwise streaks underneath the larger roll; although in this case they are aligned with the x_1 direction. However, smaller streaks are not represented in panel (a), as they do not contribute to the destruction of the near-wall coherence of the rolls above (figure 12a).

present model complements and generalises previous studies formulated in terms of single-scale near-wall streaks and quasistreamwise vortices to the analogous log-layer streaks and rolls of arbitrary size x_2. The mechanism above also shares some similarities with the physical arguments pertaining to the modification of near-wall turbulence in the presence of oscillating walls characteristic of drag reduction studies (Jung *et al.*, 1992; Laadhari *et al.*, 1994; Choi & Clayton, 2001; Choi *et al.*, 2002; Ricco & Quadrio, 2008), although our model is tailored for multiscale flows and uniform accelerations.

It is worth noting that the reduction of the Reynolds stress has been mainly modelled on the basis of non-equilibrium effects rather than on the three-dimensionality of the mean flow and, therefore, is not constrained to the application of additional mean pressure gradients only in the spanwise direction. Accordingly, the model also predicts that a sudden forcing in the streamwise direction would encompass a decrease of the Reynolds stress as long as the relative shift between wall-parallel layers is capable of misaligning the cores of the roll and the streaks underneath. As it is well-known that streaks are longer than wider across the logarithmic layer by a factor of 3 to 6, we can anticipate that suddenly imposed streamwise mean pressure gradients are less efficient in decreasing the Reynolds stress than their spanwise counterparts. This view is supported by the studies by He & Seddighi (2013), He & Seddighi (2015) Seddighi *et al.* (2015), and Mathur *et al.* (2018), who showed that channel flows subjected to streamwise mean pressure gradients exhibit a similar, but less exacerbated, counter-intuitive response of flow consistent with the model presented here.

To conclude, we comment on the similarities and differences of the present structural model with respect to previous models in the literature. We should stress first that our model relies on the multiscale organisation of the flow, while past models are usually formulated under the assumption of a single-scale flow at low Reynolds number. From figure 13, it was argued that the flow structures produced under the additional mean shear are smaller in size, and that this contributes to the loss of coherence from the viewpoint of the upper flow layers. The generation of smaller eddies is supported by the work of Lozano-Durán & Bae (2019), who showed that the characteristic length scale of the flow structures decreases proportionally to the mean shear. Our model is also consistent with the generation of smaller flow features postulated by Lohmann (1976) and corroborated experimentally by Kiesow & Plesniak (2002) for the near-wall region. Bradshaw & Pontikos (1985) suggested that the mechanism responsible for the reduction in the Reynolds stress is the tilting about the streamwise direction of pre-existing flow structures caused by the "instant" introduction of $\partial\langle u_3\rangle/\partial x_2$ by inviscid skewing. In the present flow configuration, $\partial\langle u_3\rangle/\partial x_2$ diffuses upwards from the wall in a finite time. Yet, the aforementioned tilting mechanism is not completely incompatible with the model depicted in figure 14, as the relative displacement between wall-parallel flow layers still entails some degree of inclination of the eddies in the x_1–x_2 plane. Coleman *et al.* (1996*b*) noted that the toppling of eddies dominates when the three-dimensionality is introduced by inviscid skewing, but its role might be secondary in cases with uniform lateral acceleration as in the present study. Comparisons with previous models framed in terms of the evolution of streaks, ejections, and sweeps are complicated due to the lack of interaction between flow structures at different scales. Eaton (1991) and Kannepalli & Piomelli (2000) hypothesised that the cross-flow could inhibit the intensity of the low-velocity streaks and, consequently, the associated Reynolds stress from the streak breakdown. Other works advocate for an asymmetric distribution of sweeps and ejections as a key requirement for the Reynolds stress reduction (Anderson & Eaton, 1989; Sendstad & Moin, 1992; Littell & Eaton, 1994; Eaton, 1995; Chiang & Eaton, 1996; Wu & Squires, 1997). Although the weakening of the streaks and the asymmetry of sweeps/ejections are not necessarily incompatible with our model, they are not essential components to attain a Reynolds stress reduction.

2.3.6 Evolution of the tangential Reynolds stress budget

We examine the reduction of $-\langle u_1'u_2'\rangle$ from the Reynolds-stress budget viewpoint to complement the physical insight gained from the structural analysis in §2.3.4. We use the static frame of reference $\mathcal{F}$ to avoid the complexity of additional terms of the form $\partial/\partial t$ in the budget equation. Following Mansour *et al.* (1988), the dynamic equation for the component $\langle u_i'u_j'\rangle$ is given by

$$\frac{\mathcal{D}\langle u_i'u_j'\rangle}{\mathcal{D}t} = P_{ij} + \varepsilon_{ij} + T_{ij} + PS_{ij} + PD_{ij} + V_{ij}, \tag{15}$$

where the terms in the right-hand side of (15) are the Reynolds stress production (P_{ij}), dissipation (ε_{ij}), turbulent diffusion (T_{ij}), pressure strain (PS_{ij}), pressure diffusion (PD_{ij}), and viscous diffusion (V_{ij}) defined as

$$P_{ij} = -\langle u_i'u_k'\rangle \left\langle \frac{\partial u_j}{\partial x_k} \right\rangle - \langle u_j'u_k'\rangle \left\langle \frac{\partial u_i}{\partial x_k} \right\rangle, \tag{16}$$

$$\varepsilon_{ij} = -2\nu \left\langle \frac{\partial u_i'}{\partial x_k}\frac{\partial u_j'}{\partial x_k} \right\rangle, \tag{17}$$

$$T_{ij} = -\left\langle \frac{\partial u_i'u_j'u_k'}{\partial x_k} \right\rangle, \tag{18}$$

$$PS_{ij} = -\left\langle u_i'\frac{\partial p'}{\partial x_j} + u_j'\frac{\partial p'}{\partial x_i} \right\rangle, \tag{19}$$

$$V_{ij} = \left\langle \frac{\partial^2 u_i'u_j'}{\partial x_k \partial x_k} \right\rangle. \tag{20}$$

In order to obtain quantities that are only a function of time, we introduce the average along x_2-bands, which is indicated by $\overline{(\cdot)}$. The wall-normal bands inspected are $x_2^+ \in [5, 50]$ and $x_2^* \in [0.2, 0.3]$, which lie within the buffer region and logarithmic layer, respectively. The gains produced by the budget components $\bar{\phi}_{ij}$ for $(i,j) = (1,2)$, $(i,j) = (1,1)$, and $(i,j) = (2,2)$ are defined as

$$\mathrm{Gain}_{-12} = \frac{-\bar{\phi}_{12}(t) + \bar{\phi}_{12}(0)}{-\overline{P}_{12}(0)}, \tag{21}$$

$$\mathrm{Gain}_{11} = \frac{\bar{\phi}_{11}(t) - \bar{\phi}_{11}(0)}{\overline{P}_{11}(0)}, \tag{22}$$

$$\mathrm{Gain}_{22} = \frac{\bar{\phi}_{22}(t) - \bar{\phi}_{22}(0)}{\overline{PS}_{22}(0)}, \tag{23}$$

where Gain_{-12}, Gain_{11}, and Gain_{22} represent the gain in the Reynolds-stress budget equation for $-\overline{\langle u_1'u_2'\rangle}$, $\overline{\langle u_1'u_1'\rangle}$, and $\overline{\langle u_2'u_2'\rangle}$, respectively. Note that Gain_{-12} is defined such that $-\overline{P}_{12} >$

0 contributes to increasing the magnitude of $-\overline{\langle u_1'u_2'\rangle}$. We analyse the channel flow at $Re_\tau \approx 500$ and $\Pi = 60$, in which case the maximum drop in $-\overline{\langle u_1'u_2'\rangle}$ occurs at $t^+ \approx 170$ and $t^* \approx 0.7$ for the bands in the buffer region and logarithmic layer, respectively.

The gains are reported in figure 15 as a function of time. We discuss first the results for the buffer layer region $x_2^+ \in [5, 50]$. Figure 15(a) shows the Evolution of $-\overline{P}_{12}$, $-\overline{T}_{12}$, and $-\overline{PS}_{12}$. The remaining terms are not significant in magnitude nor they play any relevant role in the discussion below and they are omitted for the sake of simplicity. The main contributor to the destruction of $-\overline{\langle u_1'u_2'\rangle}$ is the drop in production $-\overline{P}_{12}$, which can be traced back to a deficit on the pressure-strain correlation in the budget equation for $\overline{\langle u_2'u_2'\rangle}$ (figure 15c). Similarly, the decline of the streaks is the consequence of a lower production $\overline{P}_{11}$ (figure 15e), also caused by the drop in $-\overline{\langle u_1'u_2'\rangle}$.

The sequence of events is similar farther away from the wall as seen in figures 15(b,d,f) for $x_2^* \in [0.2, 0.3]$. The main sink of tangential Reynolds stress arises from the turbulent production $-\overline{P}_{12}$. The reduction in $-\overline{P}_{12}$ is connected to the lower pressure-strain correlation $\overline{PS}_{22}$ in the budget equation of $\overline{\langle u_2'u_2'\rangle}$ akin to the situation described for the buffer region. The decay of the streaks is similarly governed by the drop in the production of streamwise Reynolds stress $\overline{P}_{11}$, with some additional contribution by the turbulent diffusion $\overline{T}_{11}$.

The process of Reynolds stress reduction is then sequentially described by *(i)* the growth of the spanwise boundary layer $\partial\langle u_3\rangle/\partial x_2$, which *(ii)* inhibits the redistribution of energy to $\langle u_2'u_2'\rangle$ via pressure-strain correlation, followed by *(iii)* the weakening of the production of tangential Reynolds stress, which *(iv)* eventually causes the drop in $-\langle u_1'u_2'\rangle$. The terms involved at each step of the process are summarised in figure 16. A similar effect has been observed in transitional boundary-layer flows subjected to spanwise wall oscillations (Hack & Zaki, 2015). Our findings are consistent with the previous theory on transversely strained boundary-layer flows by Moin *et al.* (1990) and Coleman *et al.* (1996*a*) and extends the results to the outer layer of wall bounded turbulence. The leading role of $\partial\langle u_3\rangle/\partial x_2$ in the drop of $-\langle u_1'u_2'\rangle$ is also consistent with the structural model promoted in §2.3.4, where it was argued that the deficient transport of momentum by the streamwise rolls has its origin on the displacement among fluid layers induced by $\partial\langle u_3\rangle/\partial x_2$.

2.4 Applications to wall-modelled LES

We study the predictive capabilities of WMLES in non-equilibrium 3-D channel flows at $Re_\tau \approx 1000$. As discussed in previous sections, this relatively simple flow set-up entails fundamental features of 3DTBL that may challenge the available model formulations. The rapid temporal and wall-normal variations in the strain and vorticity, as illustrated in figure 17, have the potential of rendering turbulence closure models calibrated to equilibrium turbulence of limited utility. Additionally, the accurate prediction of the wall-shear angle and Reynolds stress magnitude is also of paramount importance in external flows over wings or bluff bodies, as it can directly affect the force exerted on the bodies through modification of circulation, downwash effects, pressure redistribution, and strength of separation.

Recent studies of WMLES in transient 3-D channel flows include the works by Carton de Wiart *et al.* (2018), Yang *et al.* (2019) and Bae *et al.* (2018*b*). Carton de Wiart *et al.* (2018) investigated the performance of WMLES in an ample set of cases including acceleration in the streamwise direction, and showed that WMLES is capable of predicting the wall stress

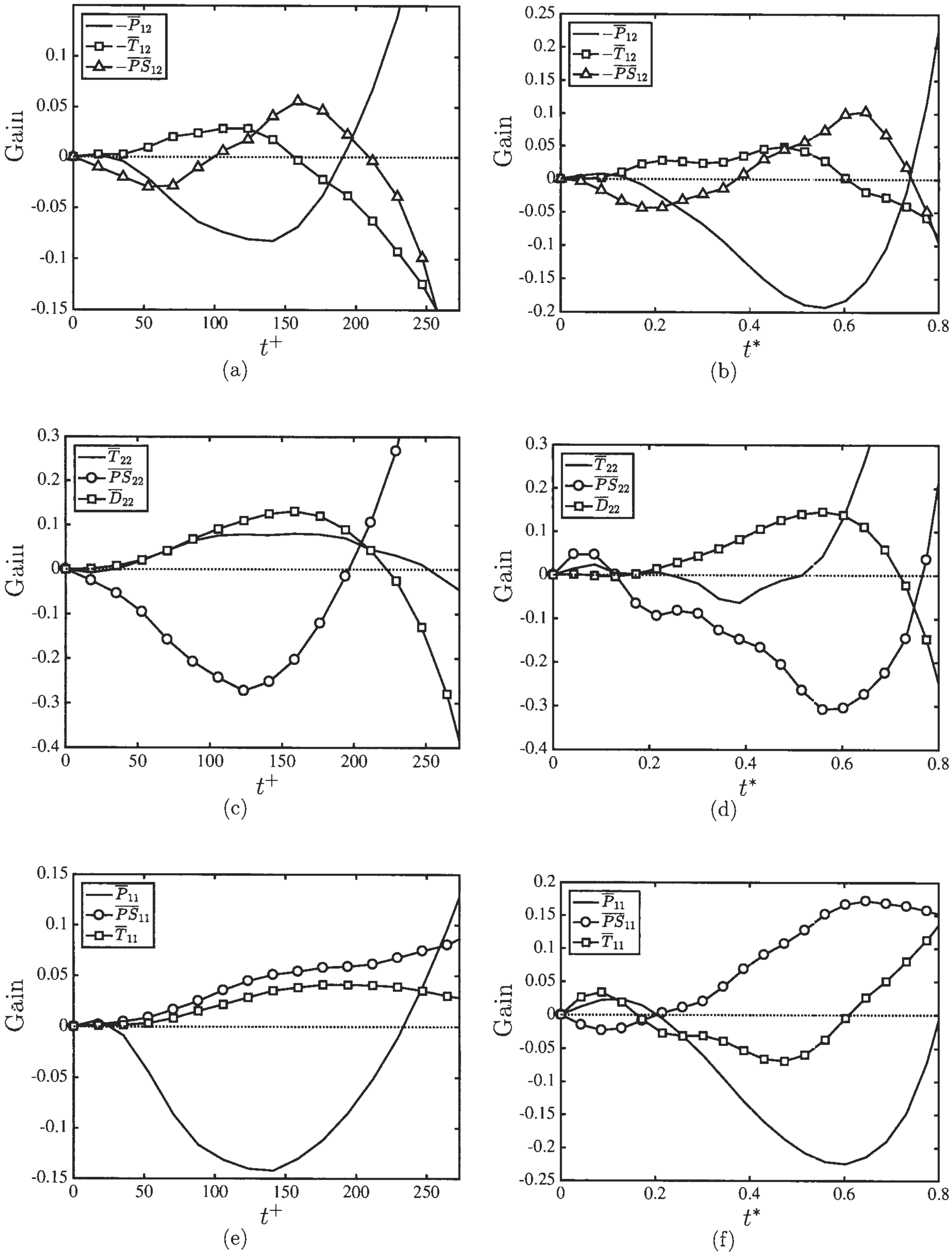

Figure 15: Evolution of the gain produced by the different terms of the Reynolds-stress budget for (a,b) $-\overline{\langle u_1' u_2' \rangle}$, (c,d) $\overline{\langle u_2' u_2' \rangle}$, and (e,f) $\overline{\langle u_1' u_1' \rangle}$. Panels on the left are for $x_2^+ \in [5, 50]$, and panels on the right are for $x_2^* \in [0.2, 0.3]$. The results are for $\Pi = 60$ at $Re_\tau \approx 500$. Zero gain is represented by (········).

$$\frac{\mathrm{d}P}{\mathrm{d}x_3}\uparrow \longrightarrow \frac{\partial \langle u_3 \rangle}{\partial x_2}\uparrow \longrightarrow \Delta p' = -2\frac{\partial \langle u_3 \rangle}{\partial x_2}\frac{\partial u_2'}{\partial x_3} + \ldots \longrightarrow \left\langle p' \frac{\partial u_2'}{\partial x_2} \right\rangle \downarrow \longrightarrow \langle u_2'^2 \rangle \downarrow \longrightarrow \langle u_2'^2 \rangle \frac{\partial \langle u_1 \rangle}{\partial x_2} \downarrow \longrightarrow -\langle u_2' u_1' \rangle \downarrow$$

Sudden spanwise pressure gradient	Development of lateral boundary layer	New pressure field by continuity	Drop in energy redistribution via pressure strain	Decrease of Reynolds stress production	Reduction of Reynolds stress

Figure 16: Summary of the sequential process of Reynolds stress reduction from the sudden imposition of a spanwise pressure gradient up to the final decrease in tangential Reynolds stress. Time goes from left to right. See text for details.

with a reasonable degree of accuracy. Yang *et al.* (2019) also attained good results using wall modelling via physics-informed neural networks, while Bae *et al.* (2018*b*) employed a novel parameter-free dynamic wall model to predict the wall stress in a flow configuration similar to the present set-up.

2.4.1 Wall models

At the coarse near-wall grid resolutions of WMLES, the usual no-slip condition ceases to produce an accurate estimate of the momentum drain at the wall. Hence, wall models are responsible for estimating the wall-shear stress. The LES equations are integrated in time using the wall-shear stress provided by the wall model as a Neumann boundary condition instead of the no-slip condition. The kinematic no-penetration condition is maintained for the impermeable walls of the channel. Three wall models are investigated in the present work: the equilibrium wall model by Kawai & Larsson (2012), and the non-equilibrium wall models by Park & Moin (2014) and Yang *et al.* (2015). We briefly summarise the main characteristics of each model and the modifications performed in the present work with respect to their original formulations.

The model by Yang *et al.* (2015) accounts for non-equilibrium effects while retaining a moderate complexity. This model assumes a parametric velocity profile in the near-wall region, where the coefficients are determined by enforcing a set of physical constraints. These include the continuity of the profile, the LES matching condition at a specified wall distance, and the compliance with the vertically integrated momentum equation, among others. The model is usually referred to as integral wall model (IWM), since the momentum integral constraint is crucial in accounting for non-equilibrium effects. In the original formulation, the wall-model input is averaged in time to regularise the wall-shear stress, which otherwise was found to cause numerical instabilities. In the present study, given the statistically unsteady nature of the flow, the time averaging is replaced by spatial averaging along wall-parallel planes. To comply with the outer LES equations, we modify the original formulation by Yang *et al.* (2015) to account for the spanwise pressure forcing.

The non-equilibrium wall model by Park & Moin (2014, 2016) solves the full Reynolds-averaged Navier-Stokes equations on a separate near-wall mesh with a mixing-length type eddy-viscosity closure which dynamically accounts for the resolved portion of the turbulence in the wall-model domain. This formulation is the most comprehensive amongst the

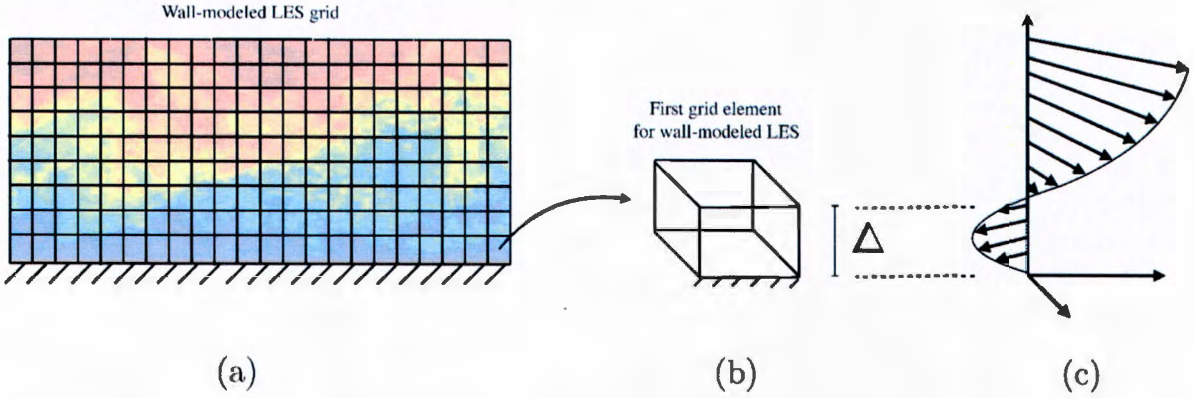

Figure 17: (a) Sketch of a typical grid for WMLES of a turbulent boundary layer. The background colours represent the streamwise velocity from zero velocity (dark blue) to the free stream value (dark red). (b) First grid cell of size Δ at the wall, and (c) comparison with the potential directional changes in the mean velocity profile along the wall-normal coordinate in 3DTBL.

considered wall-stress models, and accounts for non-equilibrium effects embedded into the original Navier-Stokes equations. Herein, this model is termed NEQWM. In order to avoid an over-prediction of the skin friction, the resolved turbulent stress is evaluated on the fly, and it is then subtracted from the modelled stress. Similarly to the IWM, the formulation by Park & Moin (2014) was adjusted to account for the spanwise pressure forcing. This turned out to be particularly important in order to provide the required dominant balance in the momentum conservation equation for the initial times of the transient.

Lastly, the equilibrium wall model (EQWM) of Kawai & Larsson (2012) is derived from the NEQWM by retaining only the wall-normal diffusion terms. The model involves a simple ordinary differential equation, which is solved along the wall-normal direction on each wall face (Wang & Moin, 2002). Consistent with the one-dimensional nature of the model, the spanwise mean pressure gradient vector was projected to the local flow direction at the matching location, and this was added to the EQWM equation as a momentum source term. A similar term was added to the energy equation for consistency.

2.4.2 Numerical set-up

The codes used for wall-modelled calculations are different from the solver presented for DNS, mainly because the wall models were conveniently available in other well-validated LES codes. The calculations using the NEQWM and EQWM are conducted using the code CharLES, which is an unstructured-grid finite-volume LES code for compressible flows developed at the Center for Turbulence Research and currently maintained by Cascade Technologies, Inc. The nominal spatial accuracy of the code is second order, but the reconstruction scheme upgrades to a fourth-order accuracy on uniform Cartesian grids (Herrmann, 2010; Khalighi *et al.*, 2011). The dynamic Smagorinsky model (Moin *et al.*, 1991; Lilly, 1992) is used as subgrid-scale (SGS) model in the filtered conservation equations. The bulk Mach number is fixed at 0.2 for comparison with the incompressible DNS solution.

For the IWM, we use the LESGO solver (LESGO, 2019). The code solves the incompressible filtered Navier-Stokes equations in a half channel with a staggered grid, using a pseudo-spectral approach in the wall-parallel directions and a second-order central finite-difference scheme in the wall-normal direction. The scale-dependent Lagrangian-dynamic Smagorinsky model is used as SGS model (Bou-Zeid *et al.*, 2005). One of the most important impediments of the wall models considered above is that they rely explicitly or implicitly on a Reynolds-averaged parametrisation of the flow, usually through an eddy viscosity, and their coefficients are adjusted by assuming fully-developed turbulence which is statistically in equilibrium. By construction of these models, the imposition of additional mean shear is accompanied by an increment in the magnitude of the Reynolds stresses (see the reviews by Piomelli & Balaras, 2002; Bose & Park, 2018), which might not be case under non-equilibrium conditions.

The LES grid resolution is uniform in the three spatial directions and equal to $(\Delta_1^+, \Delta_2^+, \Delta_3^+)$ = (180, 60, 133) or $(\Delta_1^*, \Delta_2^*, \Delta_3^*)$ = (0.2, 0.06, 0.14). The size of the computational domain is $(L_1^*, L_2^*, L_3^*) = (8\pi, 2, 3\pi)$, which yields a total of 265,980 grid cells distributed as $(N_1, N_2, N_3) = (130, 31, 66)$, in the streamwise, wall-normal, and spanwise directions, respectively. The internal grids for EQWM and NEQWM have 30 to 40 cells stretched along the wall-normal direction. Additionally, the NEQWM shares the same wall-parallel resolution as the LES grid. The wall-normal exchange between the wall model and the LES is located at the centroids of the third grid cell away from the wall, $x_2^* \approx 0.16$.

The calculations are initialised with a 2-D channel flow in a statistically steady state at $Re_\tau \approx 1000$. Then, a spanwise pressure gradient of $\Pi = 10$ is applied to induce a cross-stream shear layer, as in §2.2. The transverse mean pressure gradient selected is relatively low in order to mimic the fact that at high Reynolds numbers, the near-wall layer is in a quasi-equilibrium state, as discussed in §2.3.2. The simulations are run for one eddy-turnover time based on the streamwise friction velocity and channel half-height, $t^* \approx 1$. The results are averaged in the homogeneous directions and among runs starting from ten uncorrelated initial conditions.

2.4.3 Results and discussion

Figure 18 shows the evolution of the streamwise and spanwise mean wall-stress components denoted by $\langle \tau_1 \rangle$ and $\langle \tau_3 \rangle$, respectively. We discuss first the predictions for $\langle \tau_3 \rangle$. A general observation from figure 18(a) is that the NEQWM produces a fairly accurate prediction of $\langle \tau_3 \rangle$ throughout the transient. For short times ($t^* < 0.1$), the NEQWM predictions are closely followed by those from IWM, while the EQWM results in 50% to 25% under-prediction of $\langle \tau_3 \rangle$ throughout the initial transient. The EQWM and the IWM still capture correctly the growth rate of $\langle \tau_3 \rangle$ for $t^* \gtrsim 0.1$. For $t^* \approx 1$, the errors by NEQWM and IWM are roughly 2%, whereas the error for the EQWM is 10%. As a reference, the laminar response of the flow is also included in the figure, which shows that the spanwise wall stress agrees with the laminar solution for $t^* < 0.1$.

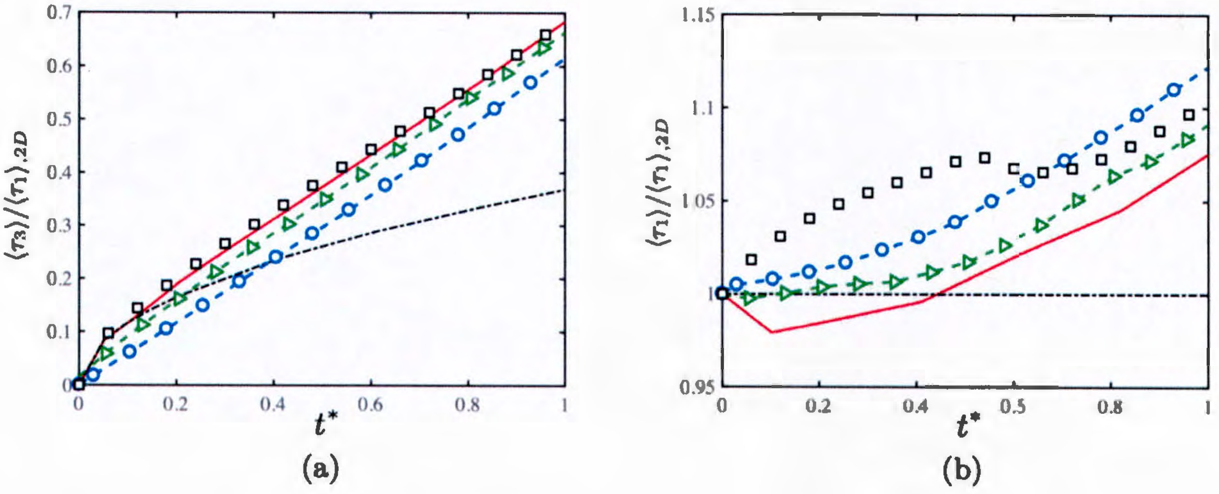

(a) **(b)**

Figure 18: Evolution of (a) the mean spanwise wall-stress $\langle\tau_3\rangle$ and (b) the mean streamwise wall-stress $\langle\tau_1\rangle$ for WMLES and DNS. The stresses are normalised by the value of the initial 2-D streamwise wall-stress $\langle\tau_1\rangle_{,2D}$. The lines and symbols are (——), DNS; (□), WMLES (NEQWM); (△), WMLES (IWM); (○), WMLES (EWQM); (–· –·), laminar solution. Note that the variations in the vertical axis of panel (b) are up to 70% of $\langle\tau_1\rangle_{,2D}$, while those in panel (b) are only up to 15%.

The evolution of $\langle\tau_1\rangle$ is plotted in figure 18(b). Note that the variations in $\langle\tau_1\rangle$ are only up to 10% and well below the changes undergone by $\langle\tau_3\rangle$, which are up to 70%. The EQWM and the IWM predict the wall-stress throughout the transient within 5% and 2% error, respectively. The NEQWM predicts a relatively faster variation in $\langle\tau_1\rangle$ for $t^* \lesssim 0.4$ compared to IWM and EQWM, with deviations from the DNS up to 7%. In all cases, the errors decay as time advances. As expected, none of the wall-models is able to reproduce the initial reduction in $\langle\tau_1\rangle$ for $t^* \lesssim 0.4$. Such a decrease in the streamwise wall-stress component is the result of the complex flow dynamics discussed in §2.3. The wall-models investigated are based on the eddy-viscosity assumption; increasing shear rates in the flow results in additional strain rates. Hence, it comes as no surprise that WMLES consistently exhibits an approximately monotonic increase in $\langle\tau_1\rangle$ after the sudden spanwise pressure gradient is applied due to the additional transverse straining of the flow in the near-wall region.

Evolution of the wall-shear angle, defined as $\gamma_w = \tan^{-1}(\langle\tau_3\rangle/\langle\tau_1\rangle)$, is shown in figure 19(a). The performance of the wall models resembles the trends reported for $\langle\tau_3\rangle$. This similarity is easily understood by noting that the relative time-variations in $\langle\tau_1\rangle$ are modest compared to the variations in $\langle\tau_3\rangle$. The development of the mean spanwise velocity over one eddy-turnover time is shown in figure 19(b). All the WMLESs considered provide an excellent prediction of the boundary layer growth. The spanwise velocity profile develops its own logarithmic region for $t^* > 0.6$, although the slope is substantially smaller than that of equilibrium channel flows. The agreement in the spanwise profile is observed in the turbulent flow region, where contributions from the SGS models and the wall-models are expected to play a role in the mean spanwise momentum balance. These findings highlight the capability of current WMLES and SGS models to predict the mean spanwise velocity

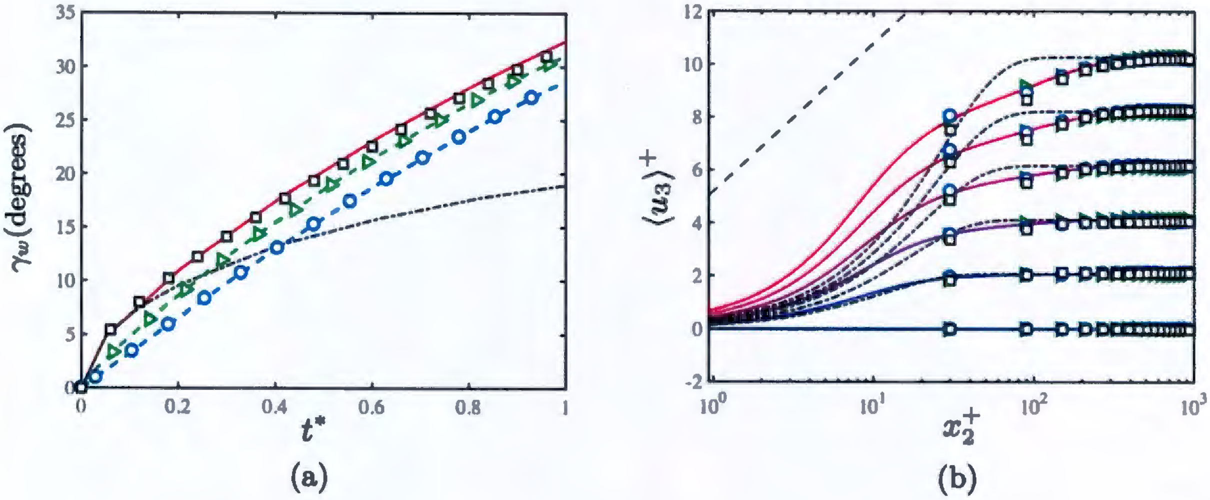

Figure 19: (a) Evolution of the wall shear-stress angle, $\gamma_w = \tan^{-1}(\langle\tau_3\rangle/\langle\tau_1\rangle)$. (b) Mean spanwise velocity at $t^* = 0$, 0.21, 0.405, 0.615, 0.825, and 1.02 (from bottom to top). The lines and symbols are (——), DNS; (□), WMLES (NEQWM); (△), WMLES (IWM); (○), WMLES (EWQM); (-· -·), laminar solution; (- - -), standard logarithmic law, $\langle u_3\rangle^+ = (1/0.41)\ln(x_2^+) + 5.2$.

Re_τ	L_1^*	L_3^*	Δ_1^+	Δ_3^+	$\Delta_{2,\min}^+$	$\Delta_{2,\max}^+$	N_2	T^*	Π	N_R
186	4π	2π	9.06	4.53	0.32	6.51	129	1	5, 10, 20, 30, 40, 60, 80	

Table 2: Geometry and parameters of the additional DNS runs to assess the effect of low Reynolds number. The parameters are defined as in table 1.

profile that arises in response to mild transverse pressure perturbations. Although not shown, the mean streamwise velocity undergoes only minor changes in time from its initial 2-D state, and good agreement is also found between DNS and WMLES.

In summary, our results show that the expected errors in WMLES under moderate non-equilibrium 3-D effects are reduced for increasing degree of modelling complexity. However, factors such as intricacy in model implementation or computational cost can favour the adoption of the simplest wall-models for some flow configurations. Future efforts should be devoted to enhance the capabilities of wall models to accurately capture the flow physics in the presence of strong non-equilibrium effects.

2.5 Response of non-equilibrium 3DTBL at low Reynolds number

For completeness, we present the results for turbulent channels with a sudden imposition of a mean spanwise pressure gradient at $Re_\tau \approx 180$. The discussion is relevant as a large body of the previous numerical studies have been carried out at this low Reynolds number. The channels are computed using the same numerical set-up as in §2.2 and the cases are listed in table 2.

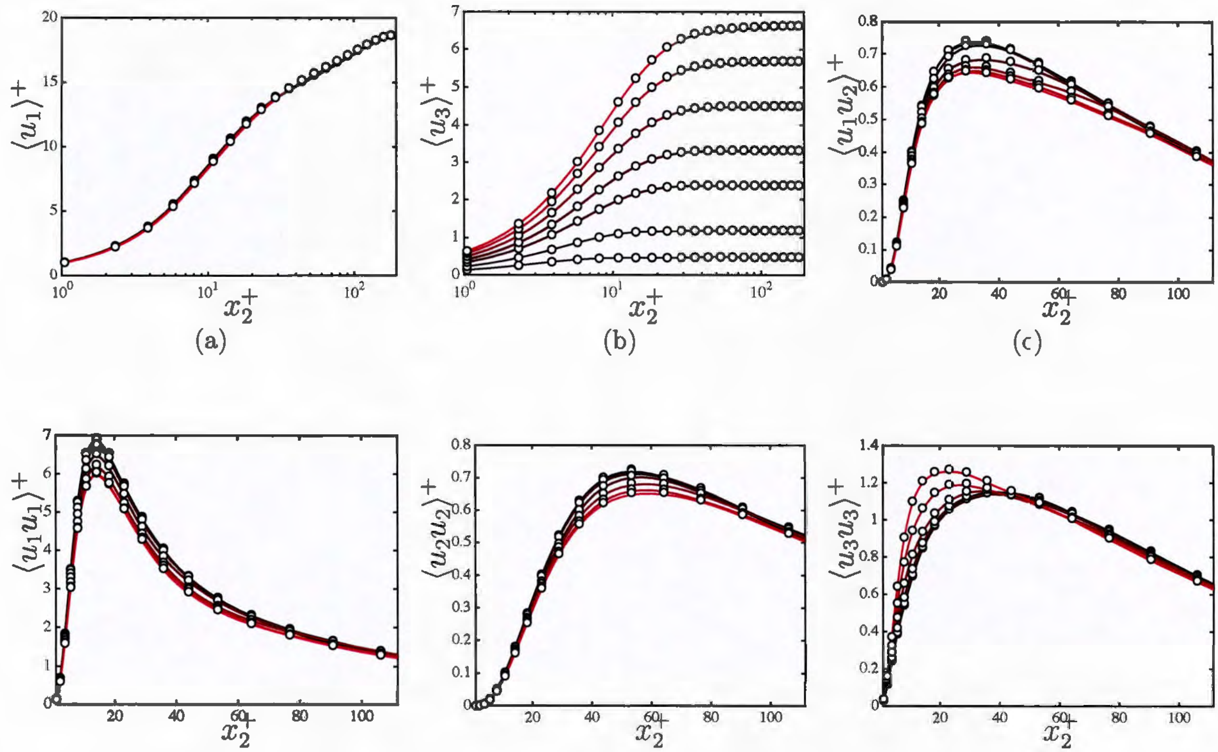
(a) (b) (c)

(d) (e) (f)

Figure 20: Validation case. Mean velocity profiles and Reynolds stresses for $\Pi = 10$ at $Re_\tau \approx 180$. Solid lines are for the present DNS results and the symbols from Moin *et al.* (1990). The results are plotted for times intervals of $0.15h/u_\tau$.

Our numerical set-up is first validated in figure 20 against the original results by Moin *et al.* (1990) at $Re_\tau \approx 180$ and $\Pi = 10$. The differences in the mean velocity profiles and Reynolds stresses are below 0.5%, which provides confidence in our results. The time response of the tangential Reynolds stress for $Re_\tau \approx 180$ and $\Pi = 30$ is shown in figure 21(a), which should be compared with the response for $Re_\tau \approx 500$ and $\Pi = 80$ from figure 21(b). In spite of the marginal change in Re_τ, the evolution of the tangential Reynolds stress is substantially different from $Re_\tau \approx 500$ to $Re_\tau \approx 180$. In the former, the drop in $-\langle u_1u_2\rangle$ occurs almost simultaneously across the channel height, while at higher Re_τ the stress follows a self-similar response in time as discussed in §2.3.3. Figure 21(c) shows the percentage drop of $\min_t\{D_\tau\}$ as a function of Π and x_2^* for $Re_\tau \approx 180$, which is analogous to figures 6(b) and (c). In contrast to the results obtained for the moderate Reynolds numbers considered in §2.3.2, the Reynolds stress depletion at $Re_\tau \approx 180$ exhibits a very weak dependence on x_2. Consequently, the higher Reynolds numbers investigated in the present work, although still moderate, enable the multiscale analysis of 3DTBL, whereas cases at $Re_\tau \approx 180$ do not exhibit a multiscale response precluding the elucidation of new potential scaling laws and physics relevant for high-Reynolds-number wall turbulence.

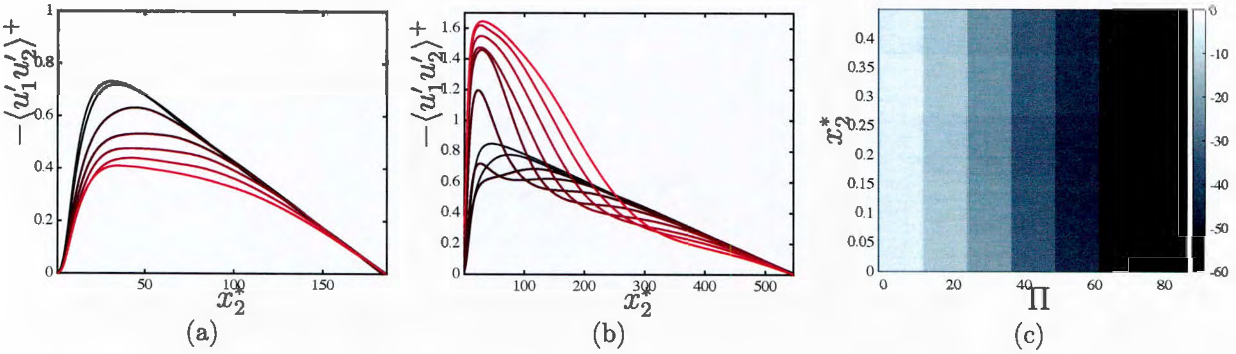

Figure 21: Evolution of the tangential Reynolds stress for (a) $Re_\tau \approx 180$ and $\Pi = 30$ and (b) $Re_\tau \approx 550$ and $\Pi = 80$. Different lines correspond to different times with increasing time from black ($t^* = 0$) to red ($t^* = 1$). The time intervals are equally spaced. (c) The percentage drop of tangential Reynolds stress, $\min_t\{D_\tau\}$, in the frame of reference of the mean shear $\tilde{\mathcal{F}}$ as a function of the spanwise to streamwise the mean pressure gradient ratio Π and wall-normal distance x_2^* for $Re_\tau \approx 180$.

Case	Re_τ	L_1^*	L_3^*	Δ_1^+	Δ_3^+	$\Delta_{2\,\min}^+$	$\Delta_{2,\max}^+$	N_2	T^*	Π	N_R
Large500	546	4π	8π	8.92	4.46	0.26	6.50	385	1	80	10
Finer500	546	4π	2π	3.68	2.15	0.18	3.40	769	1	80	10

Table 3: Geometry and parameters of the additional DNS runs to assess the effect of the computational domain and grid resolution. The parameters are defined as in table 1.

2.6 Sensitivity to the size of the computational domain and grid resolution

As the flow changes direction, the skin friction increases and the flow structures reorganise to be preferentially elongated in the spanwise direction. The former implies a reduction of the effective resolution of the simulations as time increases, whereas the latter could potentially yield spurious results due to the constrain imposed by the limited spanwise length of the domain. The most critical condition is attained at the latest time analysed, i.e. $t^* \approx 1$ and the largest values of Π. We have performed two additional simulations to assess the effect of the computational domain and grid resolution. We take as baseline case the channel at $Re_\tau \approx 500$ and $\Pi = 80$ from table 1. The details of the two additional numerical set-ups are summarised in table 3.

Simulation Large500 aims at evaluating whether the computational domain is large enough to avoid nonphysical constrains on the flow structures. The parameters considered are $Re_\tau \approx 500$ and $\Pi = 80$. The size of the domain is quadrupled in the spanwise directions from $L_3^* = 2\pi$ to $L_3^* = 8\pi$. Figure 22 compares the one-point statistics of Large500 with the original domain from table 1. The results suggest that our analysis is barely influenced by

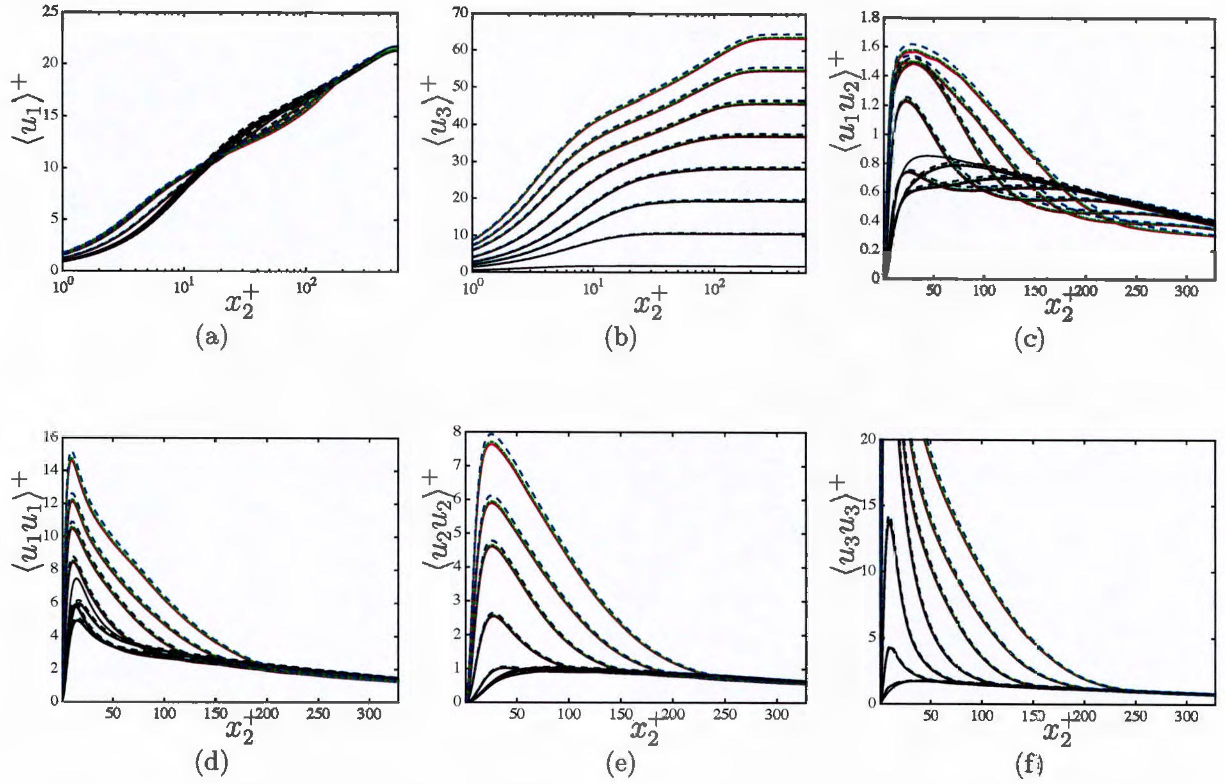

Figure 22: Mean velocity profiles and Reynolds stresses for $\Pi = 80$ at $Re_\tau \approx 500$. Solid lines are for the baseline case. Dash-dotted lines (greenish) and dashed (bluish) are for cases Large500 and Finer500, respectively. Lines with different colour intensity correspond to different times at $t^+ = 12, 72, 132, 192, 252, 312, 372$, and 432. Colours indicate time from $t^+ = 0$, dark, to $t^+ = 432$, light.

the size of the computational domain. The effect of grid resolution is tested in case Finer500 by doubling the number of grid points in each spatial direction while maintaining the original size of the computational domain. The results, included in figure 22, show differences up to ~3% at the latest times, but the grid resolution of the baseline case still suffices to capture the evolution of the mean velocity profiles and Reynolds stresses.

2.7 3-D non-equilibrium response in terms of the Townsend's structure parameter

An alternative marker to quantify 3-D non-equilibrium effects is the magnitude of the tangential Reynolds stress vector, $\tau_m = \sqrt{\langle u_1'u_2'\rangle^2 + \langle u_2'u_3'\rangle^2}$, which is shown in figure 23(a). The stress undergoes first a depletion similarly to the trend observed for $\langle u_1'u_2'\rangle$. To account for the simultaneous growth of turbulent kinetic energy, the intensity of $\sqrt{\langle u_1'u_2'\rangle^2 + \langle u_2'u_3'\rangle^2}$

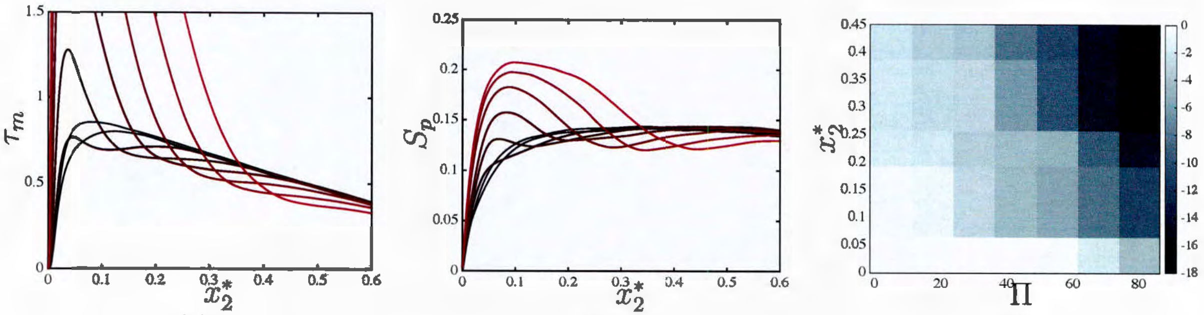

(a) (b) (c)

Figure 23: (a) Magnitude of the Reynolds stress vector $\tau_m = \sqrt{\langle u_1'u_2'\rangle^2 + \langle u_2'u_3'\rangle^2}$ and (b) Townsend's structure parameter for $\Pi = 60$ at $Re_\tau \approx 500$. Different lines correspond to different times at $t^+ = 12, 72, 132, 192, 252, 312, 372$, and 432. Colours indicate time from $t^+ = 0$, black, to $t^+ = 432$, red. (c) Maximum percentage drop of the Townsend's structure parameter (D_s) as a function of the spanwise to streamwise the mean pressure gradient ratio Π and wall-normal distance x^*.

is normally quantified by the Townsend (1976) structure parameter,

$$S_p(x_2, t) = \frac{\sqrt{\langle u_1'u_2'\rangle^2 + \langle u_2'u_3'\rangle^2}}{\langle u_1'u_1'\rangle + \langle u_2'u_2'\rangle + \langle u_3'u_3'\rangle}, \tag{24}$$

which measures the intensity of the Reynolds stress for a given amount of turbulent kinetic energy. The history of S_p also exhibits an initial drop followed by a rapid increase (figure 23b). The relative drop in S_p can be measured analogously to D_τ in (1) as

$$D_s(x_2, t) = \frac{S_p(x_2, t) - S_p(x_2, 0)}{S_p(x_2, 0)} \times 100. \tag{25}$$

The maximum reduction in time of $D_s(x_2, t)$, shown in figure 23(c), is consistent with the results in figure 6 using D_τ.

2.8 Conclusions

In the present work, we have investigated the transient response of the tangential Reynolds stress in a turbulent boundary layer with 3-D mean velocity under non-equilibrium conditions. We have focused our analysis on the multiscale response of the self-similar momentum-carrying eddies in the flow, which is the scenario expected at the Reynolds numbers encountered in real-world applications.

We have performed a series of DNS of fully-developed incompressible turbulent channel flow subjected to a sudden spanwise mean pressure gradient. A variety of spanwise to streamwise mean pressure ratios have been considered ranging from $\Pi = 1$ to 100. The sudden imposition of the forcing is followed by a continuous change of the mean-flow magnitude and direction, in which 3-D non-equilibrium effects prevail. The present set-up is one of the simplest flows enabling the study of 3-D non-equilibrium wall turbulence, while maintaining homogeneity in the streamwise and spanwise directions. We have considered two moderately high Reynolds numbers, namely $Re_\tau \approx 500$ and $Re_\tau \approx 1000$. to uncover the scaling properties of realistic 3DTBL.

Non-equilibrium effects are observed in both the original frame of reference as well as in the time- and wall-normal-dependent frame of reference aligned with the mean shear. The non-equilibrium response of the flow is controlled by the two non-dimensional parameters of the problem, namely Re_τ and Π. By assuming that wall turbulence can be comprehended as a multiscale collection of wall-attached momentum-carrying eddies with sizes and lifetimes proportional to x_2 and x_2/u_τ, respectively, we have established that the maximum depletion of the tangential Reynolds stress is proportional to Πx_2^*. Therefore, larger eddies are more prone to experience non-equilibrium effects than the smaller eddies closer to the wall. Accordingly, the flow can be classified into three distinctive flow regimes. For $\Pi < \mathcal{O}(1)$, the sudden spanwise pressure gradient is too modest to alter the statistical equilibrium of the momentum carrying eddies. Conversely, for $\Pi > 0.03Re_\tau$ the imposed mean spanwise pressure gradient is strong enough to leave out-of-equilibrium eddies at all the scales across the boundary layer, i.e., from the smallest buffer-layer eddies up to the very large scale motions populating the outer region. For $\mathcal{O}(1) < \Pi < 0.03Re_\tau$, the boundary layer attains an intermediate state in which eddies closer to the wall evolve in quasi-equilibrium, whereas eddies further from the wall are influenced by the non-equilibrium effects.

We have examined the history of the tangential Reynolds stress for cases in the fully non-equilibrium regime. The momentum-carrying eddies undergo an ordered response in time: first, the smallest eddies (closer to the wall) reduced their Reynolds stress contribution, followed by the larger eddies (farther from the wall), and so forth. During the initial transient, the results collapse across several wall-normal distances and the two Reynolds numbers inspected when the Reynolds stress drop is assumed to be proportional to Πx_2^* and the time is scaled by x_2/u_τ, consistent with the multiscale population of eddies discussed above. The collapse is further improved for longer times by noting that the characteristic equilibrium velocity and time scales (u_τ and x_2/u_τ, respectively) are no longer representative of eddies in a non-equilibrium state, which are instead controlled by the local-in-time scales $u_\tau^*(t)$ and $x_2/u_\tau^*(t)$. Our results unveil for the first time the self-similar response of non-equilibrium 3DTBL at moderately high Reynolds numbers and provides the appropriate scaling framework for future flow comparisons.

We have proposed a structural model for non-equilibrium 3DTBL rooted in the insight obtained from the physical analysis of the flow. The model comprises streamwise rolls and streaks at different scales which are initially in statistical equilibrium. The imposition of the mean spanwise pressure gradient results in the misalignment between the core of rolls and the flow underneath, which leads to a less efficient configuration of the Reynolds-stress production. The formulation of the model is consistent with the self-similar nature of the eddy response, and describes in a comprehensive manner the findings reported above. The scenario promoted here is supported by DNS results of the averaged velocity field conditioned to regions of intense Reynolds stress, which corroborate the loss of coherence of the layer underneath the core of the rolls. The new structural representation of the flow entails a quantitative advance of the previous theories on transversely strained boundary layers by providing specific scaling laws for the time scale and magnitude reduction of the Reynolds stress at multiple scales. The model also offers a theoretical ground for the different regimes observed in the flow from the quasi-equilibrium state to the fully non-equilibrium response. Inspection of the Reynolds stress budget reveals that the effect of pressure-strain correlation is key in the reduction of Reynolds stress within the additional spanwise shear layer, and that this is the case for all wall-normal heights.

Finally, the predictive capabilities of three state-of-the-art LES wall-modelling techniques have been assessed for 3-D channel flows at $Re_\tau \approx 1000$ and $\Pi = 10$. The models investigated are the equilibrium wall model by Kawai & Larsson (2012) (EQWM), and the non-equilibrium wall models by Park & Moin (2014) (NEQWM) and Yang *et al.* (2015) (IWM). As expected, wall models with a higher degree of complexity yield more accurate predictions of the mean wall-shear, although the overall performance of the three models is similar. For short times, the NEQWM yield the best prediction of the magnitude of the spanwise wall-shear and the angle of the mean wall stress vector. The prediction by IWM and EQWM follow in accuracy those by NEQWM. The larger deviations between wall models are obtained during the early times of the transient ($t^* < 0.1$), while the three models are in relatively good agreement with the DNS results for longer times ($t^* > 1$). None of the wall models considered is able to account for the initial reduction of the Reynolds shear stress and drag, presumably due to their eddy-viscosity formulations. We have argued that the near-wall layer remains in a quasi-equilibrium state at high Reynolds numbers, which explains the fair performance of WMLES based on equilibrium assumptions in transient 3-D boundary layers.

3 TASK 2: WMLES analysis of a 3-D TBL in a 30-degree bend

3.1 Introduction

Large-eddy simulation (LES) has become an essential tool for both fundamental studies and real-world engineering applications. However, industrial use of LES has been hampered by its prohibitive grid-point requirements near the wall. This limitation motivates the need for wall models to perform LES at a reduced cost by modeling small-scale near-wall eddies, while resolving large-scale eddies in the outer region Larsson *et al.* (2016); Bose & Park (2018); Chapman (1979); Choi & Moin (2012). Although wall-modeled LES (WMLES) has emerged as a viable alternative to the computationally more expensive wall-resolved LES Slotnick *et al.* (2014), the performance of wall models in non-equilibrium turbulent boundary layers with mean-flow three-dimensionality (3DTBLs) has not yet been carefully assessed. This assessment is particularly important as most widely used wall models to date are built on equilibrium assumptions such as mean-flow two-dimensionality and statistically steady state.

Skewed mean velocity profiles and non-equilibrium effects can be caused by the lateral motion of the walls or the spanwise pressure gradient imposed by the bounding geometry, among others. These 3DTBLs exist in a variety of practical problems, such as the bow and stern regions of a ship, swept-back wings, curved ducts, and turbomachinery to name a few. From the point of view of WMLES, 3DTBLs have peculiar features that are challenging to model. Among these, we can highlight the misalignment of the Reynolds stresses and the mean rate-of-strain, and the counter-intuitive depletion of wall friction and Reynolds stress magnitude (e.g. Bradshaw & Terrell, 1969; Johnston, 1970; Van den Berg & Elsenaar, 1972; Elsenaar & Boelsma, 1974; Bradshaw & Pontikos, 1985).

Recently, WMLES of a temporally-developing 3DTBL in a channel flow with a sudden imposition of spanwise pressure gradient was conducted by Lozano-Durán *et al.* (2020). The authors considered three wall-model approaches: an ordinary-differential-equation (ODE)-based equilibrium wall model Kawai & Larsson (2012), an integral non-equilibrium wall model Yang *et al.* (2015), and a partial-differential-equation-based non-equilibrium wall model Park & Moin (2014). The performance of the wall models was assessed in the transient channel flow at $Re_\tau = u_\tau h/\nu \approx 1000$, where u_τ is the wall-shear velocity, h is the channel half-height, and ν is the kinematic viscosity. Lozano-Durán *et al* (2020) quantified the accuracy in predicting the magnitude and direction of the wall stress for increasing complexity of the wall model. While the most comprehensive wall-model in terms of incorporating non-equilibrium effects outperformed the simpler approaches, the equilibrium wall model provided the best trade-off between accuracy when considering ease of model implementation and computational cost.

Recent studies of WMLES in transient 3-D channel flows also include the works by Carton de Wiart *et al.* (2018), Yang *et al.* (2019) and Bae *et al.* (2018*a*). Carton de Wiart *et al.* (2018) investigated the performance of WMLES in several cases including acceleration in the streamwise direction, and showed that WMLES is capable of predicting the wall stress with a good degree of accuracy. Yang *et al.* (2019) also attained accurate results using wall modeling via physics-informed neural networks, while Bae *et al.* (2018*a*) employed a novel

RANS-free dynamic wall model to predict the wall stress. In addition to the 3-D channel flow configuration, Cho *et al.* (2018) examined the performance of the ODE based equilibrium wall model for a spatially-developing 3DTBL inside a bent square duct at $Re_\tau = 1200 - 2400$, following the experiment of Schwarz & Bradshaw (1994). The authors reported a fairly good prediction of velocity and pressure distributions, but with a measurable discrepancy of the crossflow angles in the bend region where the mean three dimensionality is most pronounced. However, only one WMLES mesh was considered without a grid convergence study.

Another important example of non-equilibrium flows can be found in separated turbulent boundary layers. WMLES have demonstrated success in predicting trailing-edge separation of hydrofoils and airfoils (Wang & Moin, 2002; Park & Moin, 2014; Bose & Moin, 2014), and airfoils in high-lift configuration (Bodart & Larsson, 2011). In the recent NASA Juncture Flow Experiment (Rumsey *et al.*, 2019), WMLES was successful in recovering the trailing-edge separation bubble to within 10% error using on average ten points per boundary layer thickness (Lozano-Durán *et al.*, 2020*b*), which is remarkable considering the notably finer resolutions utilized by RANS-based approaches (Rumsey *et al.*, 2019). Nonetheless, it is unclear whether separated regions should be tackled with WMLES, and the question of whether a wall model is needed in the separated region remains unknown. The recent review by Bose & Park (2018) has also pointed out that the use of the no-slip boundary condition might be justified in the separated region since there the flow is governed by slow and large-scale eddies. In that case, it remains to establish how to switch between the no-slip and wall model boundary conditions.

In this article, we investigate the performance of WMLES with ODE-based equilibrium wall-model to predict 3DTBL in a bent square duct and a skewed bump. A preliminary version of the present work can be found in Cho *et al.* (2018) and Cho *et al.* (2019). The manuscript is organized as follows. We first report on the performance of the ODE-based equilibrium wall model in a spatially-developing 3DTBL inside a bent square duct, which is accompanied by a mesh convergence study in Section 3.2. In Section 4.1, we assess the ODE-based equilibrium wall model for LES predictions of 3-D separated flows. A recent experimental study by Ching *et al.* (2018*b*) on flows over a wall-mounted skewed bump with 3-D flow separations is chosen for comparison. Concluding remarks are offered in Section 4.3.

3.2 WMLES of a spatially-developing 3DTBL in a bent square duct

3.2.1 Computational details

The flow configuration of the bent square duct is shown in figure 24, which follows the experimental setup by Schwarz & Bradshaw (1994). The square duct has a 0.762m × 0.762m cross-subsection and a streamwise length of 4.561 m. In Schwarz & Bradshaw (1994), the boundary layer became turbulent by a trip wire with 1.6 mm diameter. A spatially-developing 3DTBL was generated by a 30° bend that imposes a cross-stream pressure gradient, where the boundary layer thickness are about $3 - 7\%$ of the duct side length. The surface streamlines were deflected by up to 22° relative to the centerline velocity vector. Downstream of the bend, the developed 3DTBL gradually relaxes back to a turbulent boundary layer with two-dimensional mean-flow.

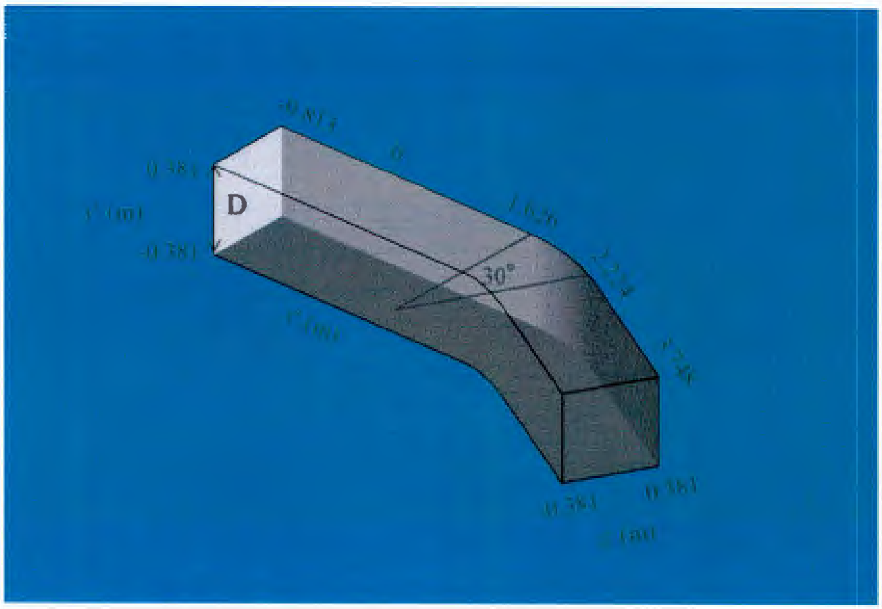

Figure 24: Flow configuration of the bent square duct. Here, the coordinate system (x', y', z') is aligned with the local duct centerline.

We define two coordinate systems following the reference experiment (see Figure 24). The first coordinate system (x, y, z) is aligned with the upstream subsection of the bend, where x, y, and z denote the streamwise, wall-normal, and spanwise directions, respectively. The velocity vector in this coordinate system is denoted by (U, V, W). The second coordinate system (x', y', z') is aligned with the local duct centerline.

WMLES is conducted using the code charLES with Voronoi mesh generator Brès *et al.* (2018). It solves the compressible LES equations with constant-coefficient Vreman model as the SGS model (Vreman, 2004). For all simulations, the coefficient of the Vreman model is set to 0.07. The unstructured Voronoi mesh generator, based on a hexagonal close packed (HCP) point-seeding method, is employed to automatically build meshes for arbitrarily complex geometries with minimal user input. Using this platform, high-quality meshes are generated suitable for low-dissipation kinetic energy and entropy preserving numerical methods for high-fidelity LES Chandrashekar (2013). To generate the grid, a surface geometry of the square duct is needed to describe the computational domain, as shown in Figure 24. Then, the user specifies the coarsest grid resolution of the uniformly seeded HCP points, Δs_{max}. Clipped Voronoi diagrams are used to generate arbitrary polyhedral cells, where the cell centers are related to these HCP points. To efficiently distribute the points within a volume, sphere packed arrangements are utilized, which generates uniform cells in regions far from boundaries. Finally, the user can introduce local mesh refinement by specifying volumes (i.e. refinement windows). The length scale discontinuities at the interface of refinement windows are handled by introducing nested refinement layers between the refinement windows and the coarsest resolution (Δs_{max}), so that these length scale jumps are never worse than 1 : 2. Additionally, Lloyd iterations are used for mesh smoothing, which align the near-wall cells normal to the surface and have a more uniform distance than the original seeding. Therefore, the resulting Voronoi cells are mostly isotropic. For the present WMLES, $\Delta s_{\max}$ is set to 0.01m and three different mesh refinements are considered, as shown in Table 4 and Figure 25. The number of Lloyd iterations is 20 in all cases. For case D1, the meshes are refined in the near-wall region so that the number of grid cells across the local boundary layer thickness (N_δ) ranges from 8 to 11 along the streamwise direction. The minimum cell size in the wall units is $\Delta s^+_{\min} = \Delta s_{\min} u_\tau/\nu = 140$, and 30.4 million control volumes are used in total. Case D2 has additional grid refinement, such that the number of control volumes across the boundary layer thickness within the bend subsection ($N_{\delta,\text{bend}}$) increases from 9 (case D1) to 13 – 15 (case D2) using 38 million control volumes. In the finest grid resolution (case D3), $\Delta s_{\min}$ is further reduced to 0.00125 m, resulting in $N_{\delta,\text{bend}} = 24$ using 76.4 million control volumes with 16 to 26 points per boundary layer thickness.

Table 4: Case setup for the bent square duct

Case	Δs (m)	N_{CV}	N_δ	$N_{\delta,\text{bend}}$
D1	0.0025–0.01	30.4M	8–11	9
D2	0.0025–0.01	38M	8–21	13–15
D3	0.00125–0.01	76.4M	16–26	24

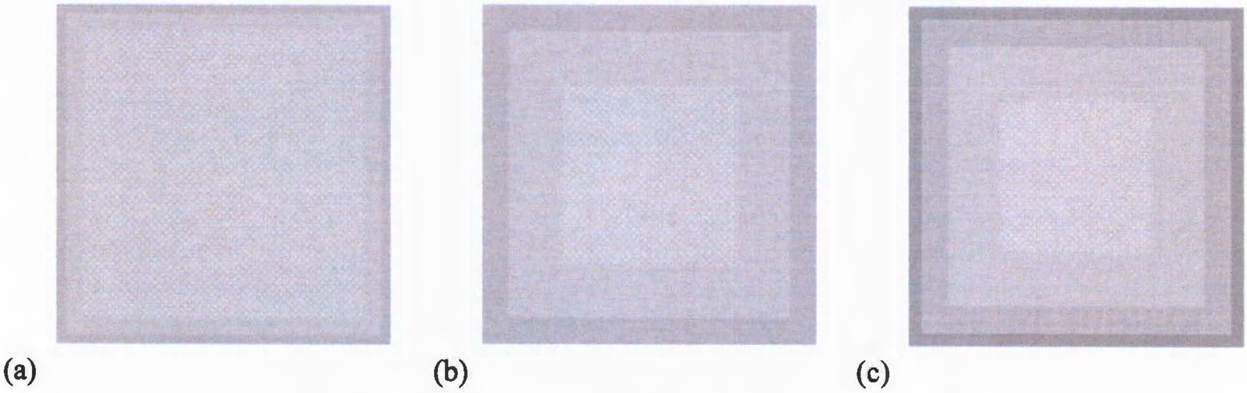

Figure 25: Cross-subsection grids ($y' - z'$ plane): (a) case D1; (b) case D2; (c) case D3.

The wall-shear stress from the ODE-based equilibrium wall model Wang & Moin (2002); Kawai & Larsson (2012); Bodart & Larsson (2012) is imposed as boundary condition at the bottom, top, and side walls. The wall-shear stress from the equilibrium wall model is obtained by integrating

$$\frac{d}{dy}\left[(\mu + \mu_{t,wm})\frac{du_\parallel}{dy}\right] = 0, \tag{26}$$

$$\frac{d}{dy}\left[(\mu + \mu_{t,wm})\, u_\parallel \frac{du_\parallel}{dy} + c_p\left(\frac{\mu}{\mathrm{Pr}} + \frac{\mu_{t,wm}}{\mathrm{Pr}_{t,wm}}\right)\frac{dT}{dy}\right] = 0, \tag{27}$$

in a layer between $y = 0$ and $y = h_{wm}$, where y is the wall-normal direction, μ is the dynamic viscosity, $\mu_{t,wm}$ is the eddy viscosity, $u_\parallel$ is the wall-parallel velocity, c_p is the specific heat at constant pressure, $\mathrm{Pr} = 0.7$ is the Prandtl number, $\mathrm{Pr}_{t,wm} = 0.9$ is the turbulent Prandtl number, and T is the temperature. The eddy viscosity is modeled using the mixing length formula

$$\mu_{t,wm} = \kappa\rho y\sqrt{\frac{\tau_w}{\rho}}D, \tag{28}$$

$$D = \left[1-\exp\left(-\frac{y^+}{A^+}\right)\right]^2, \tag{29}$$

where $\kappa = 0.4$ is the von Kármán constant, ρ is the density, τ_w is the wall-shear stress, D is the van Driest damping function, and $A^+ = 17$ is a model coefficient. The walls ($y = 0$) are assumed to be isothermal. The matching location ($y = h_{wm}$) of the equilibrium wall model is at the cell centers of wall-adjacent control volume. Temporally-filtered LES data are provided to the wall model as proposed by Yang *et al.* (2017). The characteristic-based non-reflective outflow boundary condition is imposed at the outflow plane Poinsot & Lele (1992). For the inflow boundary condition, a synthetic turbulence boundary condition is imposed to provide a realistic turbulent inflow condition that matches the experiment in the upstream subsection of the bend. Note that the experiment did not report the flow conditions near the trip wire ($x' = 0$ m), and that the boundary layer measurements are available far downstream of the trip wire ($x' > 0.826$ m). This mandated us to adopt an iterative procedure to adjust a suitable set of inflow parameters to best match the flow condition at the reported stations upstream of the bend. For this purpose, the location of the computational inlet, the mean velocity therein, and the fluctuations superimposed have been tuned. First, a uniform velocity of 26.5 m/s (the freestream value in the experiment) in the streamwise direction is chosen as the mean velocity field in the inflow plane. Random fluctuations following the standard uniform distribution (±0.2% the freemstream velocity) are then applied to all velocity components. Lastly, the development length (or the location of the computational inlet relative to the bend) is determined by an iterative procedure: a series of preliminary WMLES of a straight square duct are conducted until the mean velocity profiles at $x' = 0.978$ in cases D1, D2, and D3 match the reference experiment reasonably well (see Figure 26). The compuatational domain so determined starts at $x' = -0.813$. Then, the performance of the WMLES is evaluated at downstream locations. The Reynolds number based on the duct side length ($D = 0.762$ m) and the inlet freestream velocity (26.5 m/s) is 1,400,000. The Reynolds number based on the local momentum thickness and the freestream velocity ranges from 4,000 to 9,000 ($Re_\tau = 1,200-2,400$).

3.2.2 Results and discussion

Figure 26 shows the profile of the mean velocity magnitude ($Q = \sqrt{U^2+W^2}$) normalized with the local freestream value (Q_∞) as a function of the wall-normal distance at various streamwise locations. The velocity profiles from three grids (i.e., cases D1, D2, and D3) are almost on top of each other at each streamwise location, which indicates that the WMLES solution has reached grid convergence. For comparison, the results of the no-slip LES (without wall model) using the same coarse mesh for case D1 are also included in the figure.

In the upstream subsection of the bend at $x' = 0.978$ m, the WMLES solution reproduces the upstream condition of the reference experiment. The mean velocity magnitude profiles

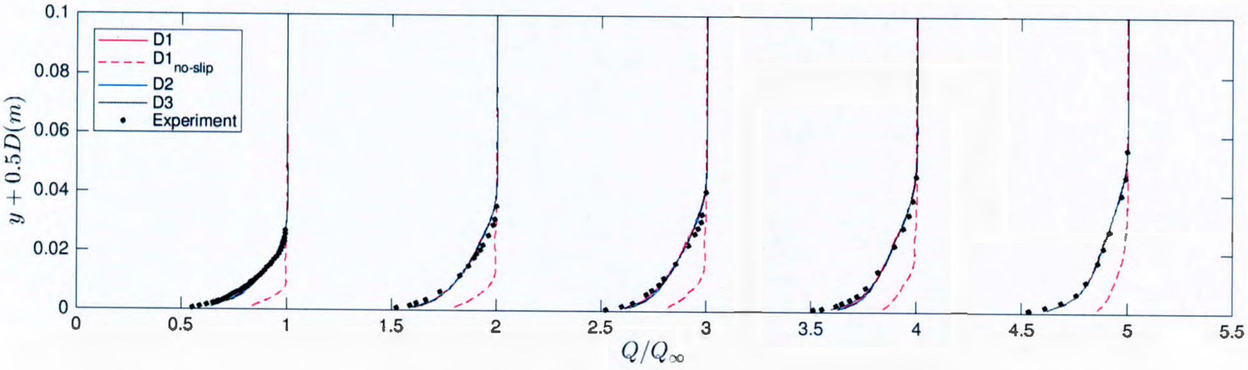

Figure 26: Mean velocity profiles at $x' = 0.978$ m (upstream subsection of the bend), $x' = 1.775$ m and 2.075 m (inside the bend), and $x' = 2.415$ m and 2.948 m (downstream subsection of the bend). Here, the profiles at $x' = 1.775, 2.075, 2.415$, and 2.948 m are shifted by $1, 2, 3$, and 4 on the horizontal axis, respectively. Lines, present WMLES (cases D1, D2, D3); circles, experiment Schwarz & Bradshaw (1994); dashed lines, no-slip LES on the case D1 mesh (without wall model).

inside the bend (at $x' = 1.775$ m and 2.075 m) and downstream subsection (at $x' = 2.415$ m and 2.948 m) are also predicted with reasonable accuracy. On the other hand, the discrepancy between the experimental data and the result from no-slip LES is remarkable, indicating the importance of deploying the wall model at the present grid resolutions. In particular, the mean velocity profiles are overpredicted in the absence of wall-model. This is a common outcome of LES on coarse grids without wall model, in which the lack of support for near-wall Reynolds stresses translates into an excess of streamwise momentum (Lozano-Durán & Bae, 2019).

Figure 27 compares the Reynolds stress profiles from the WMLES to the experiment Schwarz & Bradshaw (1994) at various streamwise locations. Here, u', v', and w' indicate velocity fluctuations in streamwise, wall-normal, and spanwise directions, respectively, and $U_{ref} = 26.5 m/s$. Consistent with the mean velocity profiles, the Reynolds stress profiles in all cases almost overlap each other at each streamwise location, and they are in reasonable agreement with the experiment. However, the profiles of the no-slip LES (without wall model) using the mesh for case D1 deviate significantly from the experiment.

The local skin friction distribution along the certerline of the square duct is shown in Figure 28. The experimental data was reported with 5% uncertainty bands, and the average error between the present WMLES and the experimental data is 8%. Similar to the trends of mean velocity and Reynolds stress profiles, the skin friction exhibits low sensitivity to different grid resolutions, and the no-slip LES (without wall model) significantly underpredicts the skin friction.

The crossflow turning angles are defined as $\gamma = \tan^{-1}(W/U)$, where W and U are spanwise and streamwise mean velocity components with respect to the upstream coordinates (x, y, z). The variations of γ along the axial directions (x') are represented in Figure 29. Hereafter, γ_∞ is γ at the freestream, while γ_s is γ at the surface. The results in Figure 29(a) show that the angle γ_∞ turns from 0° before the bend to 30° after the bend, in accordance with the specified geometry. Both WMLES (cases D1, D2, and D3) and no-slip LES (D1

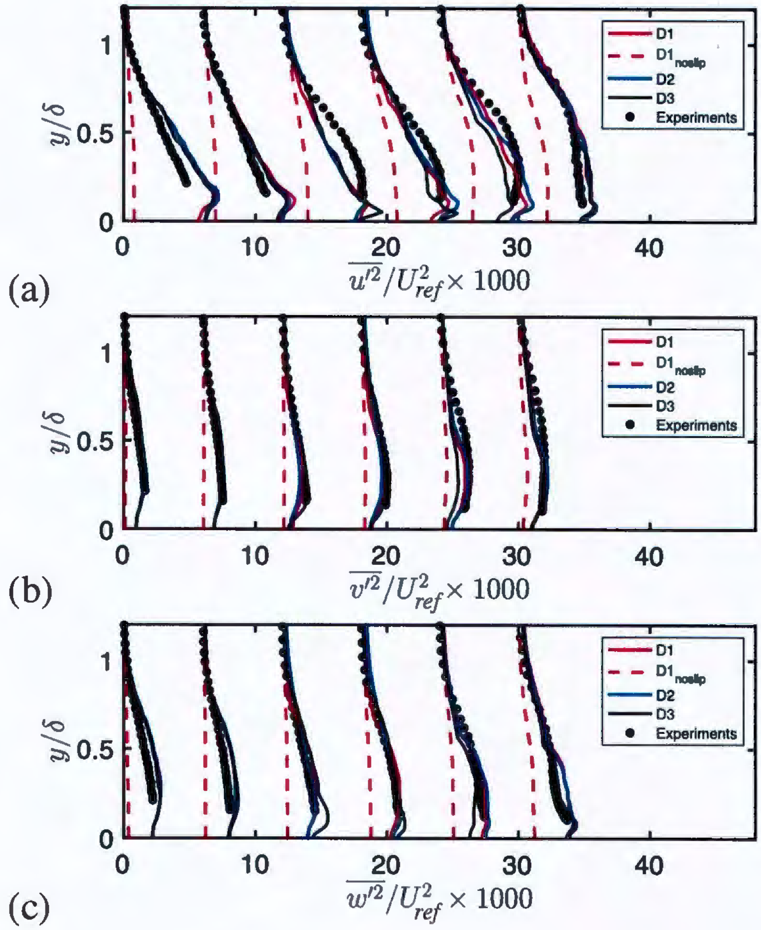

Figure 27: Reynolds stress profiles at $x' = 0.978$ m and 1.435 m (upstream subsection of the bend), $x' = 1.775$ and 2.075 m (inside the bend), and $x' = 2.415$ and 2.948 m (downstream subsection of the bend). Here, the profiles at $x' = 1.435, 1.775, 2.075, 2.415$, and 2.948 m are shifted by $6, 12, 18, 24$ and 30 on the horizontal axis, respectively: (a) $\overline{u'^2}/U_{ref}^2 \times 1000$; (b) $\overline{v'^2}/U_{ref}^2 \times 1000$; (c) $\overline{w'^2}/U_{ref}^2 \times 1000$. Lines, present WMLES (cases D1, D2, D3); circles, experiment Schwarz & Bradshaw (1994); dashed lines, no-slip LES on the case D1 mesh (without wall model).

no-slip) predictions are almost on top of each other at the freestream region. The values of γ_∞ from both the WMLES and no-slip LES calculations also show an excellent agreement with the experimental data. This can be ascribed to the essentially inviscid mechanism responsible for the turning of the flow in the core region of the square duct. Assuming a inviscid core region, it can be shown that $\gamma_\infty \approx \theta$, where θ is the geometric turning angle of the duct along the bend. A small discrepancy with experiments (¡ 2°) is observed in Figure 29 between the present simulation and the experiment close to the end of the test subsection ($x' > 3$). In a recent study, Hu *et al.* (2019) conducted WMLES of the same square duct configuration using non-equilibrium wall models and observed a tendency similar to the current WMLES for $x' > 3$. Schwarz & Bradshaw (1994) reported that the flow direction uncertainty was ±1°, where the mean velocity field was obtained using a three-hole pressure

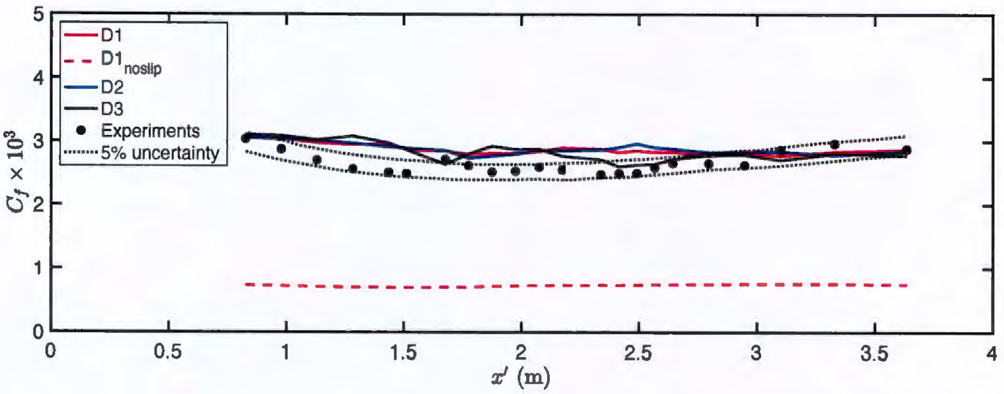

Figure 28: Local skin friction distribution along the streamwise direction (x'). Lines, present WMLES (cases D1, D2, D3); circles, experiment Schwarz & Bradshaw (1994); dashed lines, no-slip LES on the case D1 mesh (without wall model).

probe. Therefore, the difference between WMLES and experiments in the downstream of the bend region may be partly due to experimental uncertainties.

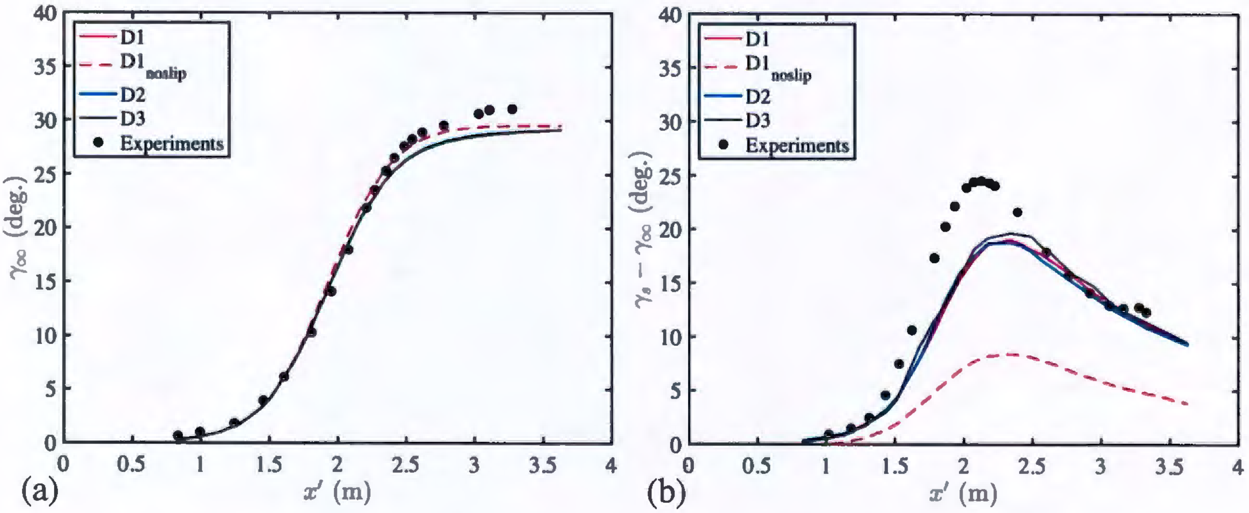

Figure 29: Crossflow turning angles: (a) freestream turning angle (γ_∞) distribution along the streamwise direction (x'); (b) surface crossflow angle relative to freestream ($\gamma_s - \gamma_\infty$) along the streamwise direction (x'). Lines, present WMLES (cases D1, D2, D3); circles, experiment Schwarz & Bradshaw (1994); dashed lines, no-slip LES on the case D1 mesh (without wall model).

Figure 29(b) shows the streamwise development of $\gamma_s - \gamma_\infty$. The initial increase of the surface crossflow angle upstream the bend subsection and its subsequent decrease are qualitatively captured by WMLES for varying grid resolutions (D1, D2, and D3). However, the magnitude of $\gamma_s - \gamma_\infty$ is underpredicted near the bend region by about 20%. These differences between the WMLES and experimental data are mainly localized within the bend, and they decrease as the 3DTBL gradually recovers to the two-dimensional turbulent boundary layer in the downstream subsection. Refining the WMLES grid resolution

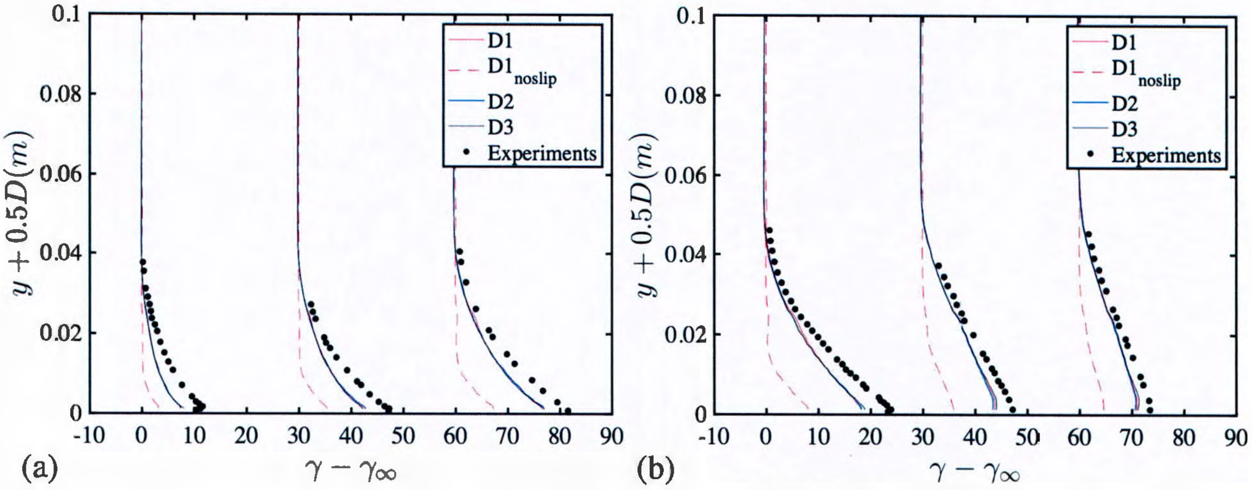

Figure 30: Crossflow angle relative to freestream: (a) crossflow inside the bend at $x'(\mathrm{m}) = 1.676, 1.875$, and 2.075; (b) crossflow in the downstream subsection of the bend at $x'(\mathrm{m}) = 2.338, 2.948$, and 3.329. Here, the profiles at $x' = 1.875$ and 2.948 m are shifted by 30° and the profiles at $x' = 2.075$ and 3.329 m are shifted by 60° on the horizontal axis, respectively. Lines, present WMLES (cases D1, D2, D3); circles, experiment Schwarz & Bradshaw (1994); dashed lines, no-slip LES on the case D1 mesh (without wall model).

(case D3) provides a slight improvement in the bend region compared to coarser grids (cases D1 and D2), but the difference is marginal. The mismatch between WMLES and experiment along the duct bend can be attributed to various causes. The first one is related to the methodology employed to obtain γ_s. Strictly speaking, the angle γ at the wall is $\gamma_s = \lim_{y\to 0} \tan^{-1}(W/U) = \tan^{-1}(\tau_W/\tau_U)$, where τ_W and τ_U are the averaged spanwise and streamwise wall stress, respectively. In the current WMLES, γ_s is obtained from the tangential wall-stress streamlines after the wall stress is averaged in time. Experimentally, the γ_s is measured by oil-flow visualizations at the wall after initial transients of the oil. Albeit both methodologies provide a reasonable description of γ_s, they do not allow for fully consistent one to one comparison, which may prompt some disagreement between both results. The second cause for the large errors in $\gamma_s - \gamma_\infty$ is probably more noteworthy, and arises from the wall-modeling assumptions in Eq. (26). The equilibrium approximation of the current wall model is such that the wall stress vector is aligned with the wall-parallel velocity at the first off-wall location, $\gamma_s = \tan^{-1}(W(x, \Delta_s, z)/U(x, \Delta_s, z))$, which might result in large errors under the presence of acute mean three-dimensionality (Lozano-Durán *et al.*, 2020). It also implies that the mesh refinement alone without the aid of non-equilibrium wall models will not improve the WMLES solution unless the LES grid is able to resolve the three-dimensionality of the mean flow Hu *et al.* (2019) recently reported that the equilibrium wall model with the minimum wall-normal grid size of 30 in wall unit (2.3 times finer than the finest case D3) still showed a discrepancy in predicting the mean three-dimensionality in the bend region. However, changing the equilibrium wall model to PDE non-equilibrium wall model was shown to improve the performance of the WMLES.

Figure 30 shows $\gamma - \gamma_\infty$ as a function of the wall-normal direction and complements the picture provided by Figure 29. The crossflow angle increases until the end of the bend subsection (Figure 30(a)) and decays in the downstream subsection (Figure 30(b)). Figure 30 also shows that the current WMLES predicts the crossflow development and decay, although the angles are smaller than those in the experiment. Consistent with Figure 29, the discrepancy between WMLES and experiments in $\gamma - \gamma_\infty$ increases with the crossflow development, and decreases after the bend once the flow starts relaxing to a turbulent boundary layer with two-dimensional mean-flow. Figure 30 also shows that no-slip LES significantly underperforms WMLES, but the lack of further improvements with mesh refinements in WMLES hints to the necessity of non-equilibrium wall-modeled accounting for 3-D non-equilibrium effects as discussed above.

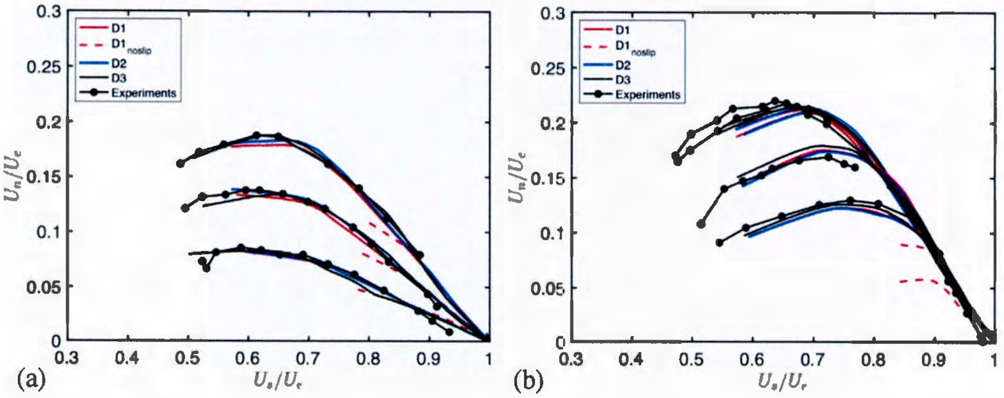

Figure 31: Triangular plot of velocity: (a) crossflow development at $x'(\mathrm{m}) = 1.676, 1.875$, and 2.075; (b) crossflow decay at $x'(\mathrm{m}) = 2.338, 2.491, 2.948$, and 3.634. Lines, present WMLES (cases D1, D2, D3); circles, experiment Schwarz & Bradshaw (1994); dashed lines, no-slip LES on the case D1 mesh (without wall model).

A common approach to quantify the 3-D characteristics of the mean-velocity profile is to construct the so-called triangular plot, which comprises the normal (U_n) and streamwise (U_s) components of the velocity with respect to the free-stream velocity (U_e). Here, we use the triangular plot to further evaluate the capability of WMLES to predict mean-flow three-dimensionality. The results, included in Figure 31, show that current WMLES cases are in reasonable agreement with the experimental data The free-stream flow is represented by $(U_s, U_n) = (1, 0)$. Both WMLES and experiments match for $U_s/U_e > 0.7$, which corresponds to the upper part of the boundary layer. Althought not shown, it was also assessed that in this region WMLES follows the expected inviscid relationship $U_n \approx 2(\gamma - \gamma_\infty)(U_e - U_s)$. The apex of maximum cross-flow occurs at $U_n/U_e \approx 0.2$, which is also well captured by WMLES. The most noticeable difference between WMLES and experiments is the absence of velocities in the range $U_s/U_e < 0.6$ for cases D1 and D2, as these values of U_s are located in the near-wall region of the boundary layer which is unresolved by the their grids. However, the refined grid from D3 is able to correctly predict the experimental values closer to the wall. On the other hand, the no-slip LES case (without wall model) deviates significantly from the experiment: the values attained by U_n are roughly half of those from WMLES and experiments, which points at a lack of three-dimensionality in the mean profile of case $\mathrm{D1}_{\mathrm{noslip}}$ consistent with the angles reported in figure 30.

4 TASK 3: WMLES analysis of 3-D TBL in a skewed bump

4.1 WMLES of a 3D flow separation behind a skewed bump

4.1.1 Computational details

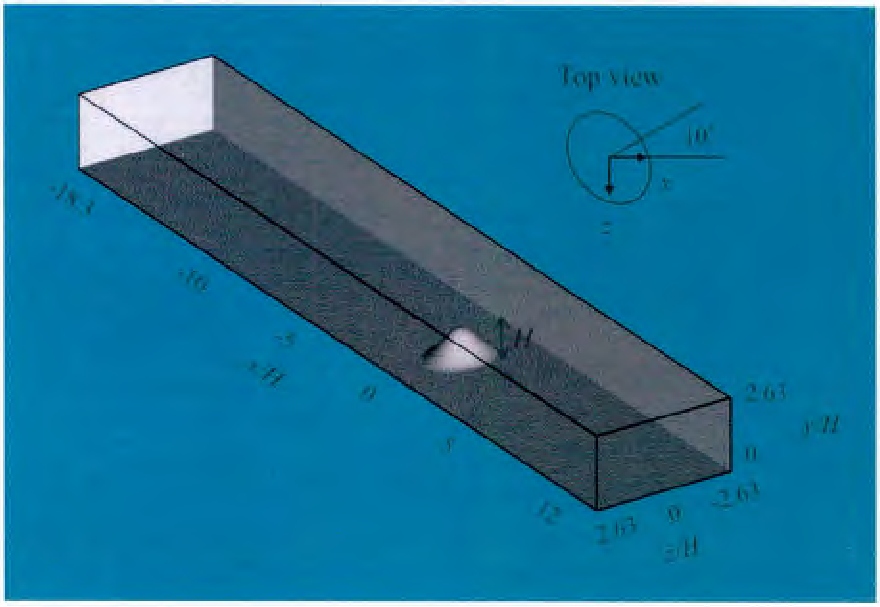

Figure 32: Flow configuration of the skewed bump. The coordinate origin is located on the bottom wall under the center of the bump.

Table 5: Case setup for the skewed bump

Case	$\Delta s/H$	N_{CV}	$N_{\delta,x/H=-4}$
B1	0.025–0.1	6.7M	20
B2	0.012–0.1	19M	20
B3	0.006–0.1	10.8M	20
B4	0.006–0.1	22.3M	20

The computational setup for the three-dimensional skewed bump is illustrated in Figure 32 which follows the study by Ching *et al.* (2018*b*). The bump is mounted on the bottom wall of a square duct, and its surface is defined by (Ching *et al.*, 2018*b*,*a*; Ching & Eaton, 2020)

$$y_s = H\left[0.5 + 0.5\cos\left(2\pi\sqrt{\frac{x_s^2}{b^2} + \frac{z_s^2}{a^2}}\right)\right], \tag{30}$$

for $\frac{x_s^2}{b^2} + \frac{z_s^2}{a^2} < \frac{1}{4}$, where x_s, y_s and z_s denote the surface of the bump in the streamwise, wall-normal, and spanwise directions, respectively; $H(= 19\text{mm})$ indicates the bump height,

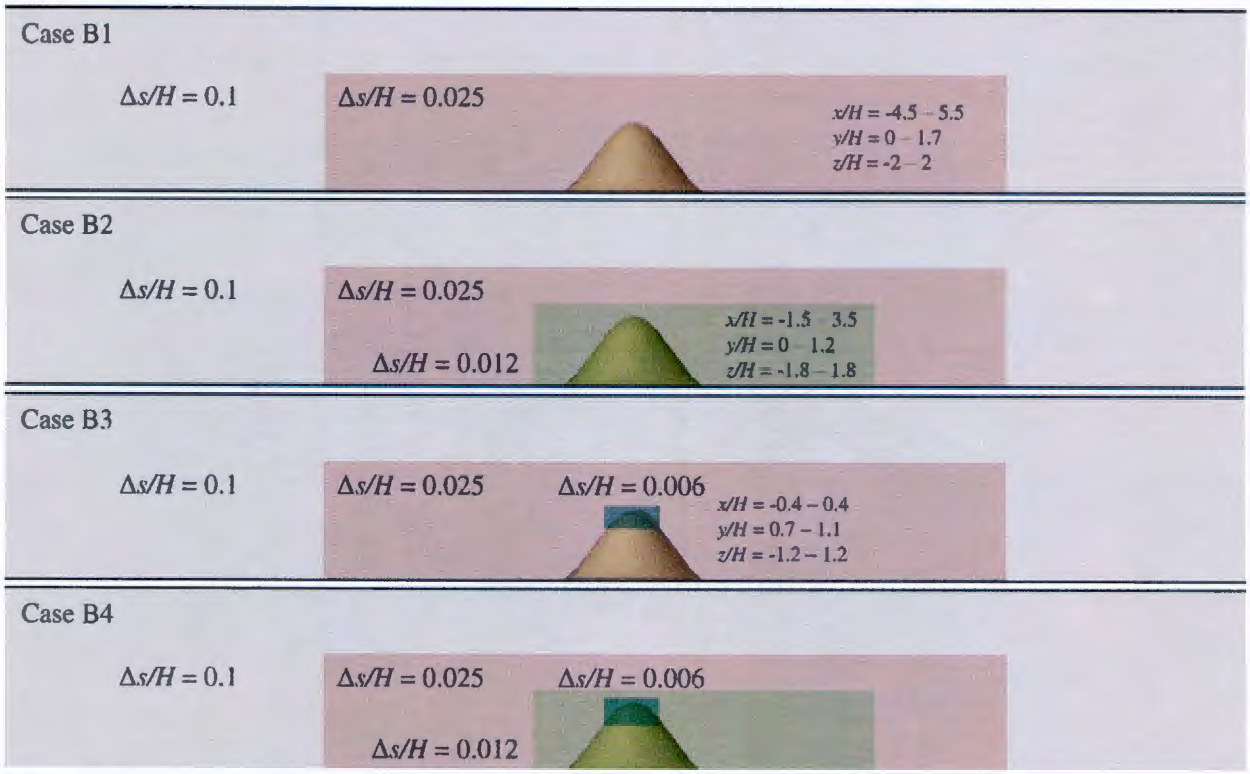

Figure 33: Schematic diagram of the mesh refinement.

and the parameters a and b are 57 mm and 42.75 mm, respectively. Here, the coordinates x_s and z_s are defined with respect to the bump rotation angle θ,

$$\begin{aligned} x_s &= x\cos(\theta) + z\sin(\theta), & (31)\\ z_s &= x\sin(\theta) - z\cos(\theta). & (32)\end{aligned}$$

The bump angle in the present study is at $\theta = 10°$. The origin of the coordinate system is located on the bottom wall below the center of the bump and the Reynolds number based on the bulk velocity (0.83 m/s), and the bump height is 16,000. The Reynolds number based on the wall-shear velocity and the local boundary layer thickness at $x/H = -4$ is 560. This is a relatively low Reynolds number case compared to the bent square duct simulation, where Re_τ ranges from 1,200 to 2,400.

We compare the WMLES results with those from experimental and LES studies Ching *et al.* (2018*b*); Ching & Eaton (2020). Previous experiments and simulations of the present axisymmetric bump have shown that the flow over the bump separates near the top due to the development of an adverse pressure gradient, i.e. the separation point is not determined by the bump geometry (Ching *et al.*, 2018*b*,*a*; Ching & Eaton, 2020). A large separation bubble is formed in the wake of the bump, where a common-up vortex pair appears in the mean flow field. Further downstream, this common-up vortex pair evolves into a common-down vortex pair.

We utilize the same flow solver, charLES, with Voronoi mesh generator. The boundary conditions for the skewed bump are similar to those of the bent square duct (see Subsection 3.2.1). At the inlet, we prescribed a synthetic turbulence boundary condition, with random fluctuations (±1.5% the freemstream velocity) added to the spatially-uniform freestream velocity of 0.83 m/s. The length of the upstream development section is determined in a separate WMLES of a square duct with the bump removed by matching the mean velocity profiles at $x/H = -4$ in cases B1 - B4 from the reference experiment (see Figure 35). Then, we examine the performance of the WMLES at downstream locations. The ODE-based equilibrium wall model from Eqs. (26) and (27) is used to obtain the wall shear stress at bottom, top, and side walls, which are also assumed isothermal. The Navier-Stokes characteristic boundary condition is imposed at the outlet Poinsot & Lele (1992).

The computational domain size is $L_x \times L_y \times L_z = 575.7$ mm × 50 mm × 100 mm. We investigate the grid requirements to capture the correct flow physics of different flow regions by considering a set of four grid resolutions, which are summarized in Table 5 and depicted in Figure 33. For all the cases, the coarsest grid resolution is set to $0.1H$, and the meshes are refined around the bump and the bottom wall ($-4.5H < x < 5.5H, 0 < y < 1.7H, -2H < z < 2H$, see red-colored region in Figure 33) such that the grid size in that region is $0.025H$. The boundary layer thickness at $x/H = -4$ is half the height of the bump ($0.5H$), and the boundary layer thickness increases in the streamwise direction until it is affected by the adverse pressure gradient as the boundary layer approaches the wall-mounted bump. The present isotropic Voronoi cells result in 20 cells across the boundary layer thickness at $x/H = -4$. For case B2, an additional refinement window with grid size equal to $0.012H$ is added to the case B1 around the bump and the bottom wall ($-1.5H < x < 3.5H, 0 < y < 1.2H, -1.8H < z < 1.8H$, see green-colored region in Figure 33). For case B3, the refinement window with the grid size of $0.006H$ is added to the case B1 on top of the bump ($-0.4H < x < 0.4H, 0.7 < y < 1.1H, -1.2H < z < 1.2H$, see blue-colored region in Figure 33). Lastly for the case B4, both refinement windows used in cases B2 and B3 are included into case B1 to assess grid convergence. The total number of smoothing iterations is 20 in all cases. It is worth nothing that our grids are in the range of ≈ 7–22M control volumes (table 5), while Ching *et al.* (2018*b*) employed 80M control volumes to perform the wall-resolved LES of the bump. This outlines the computational savings of WMLES, about ×4–8, despite the moderate Reynolds number of the present case.

4.2 Results and discussion

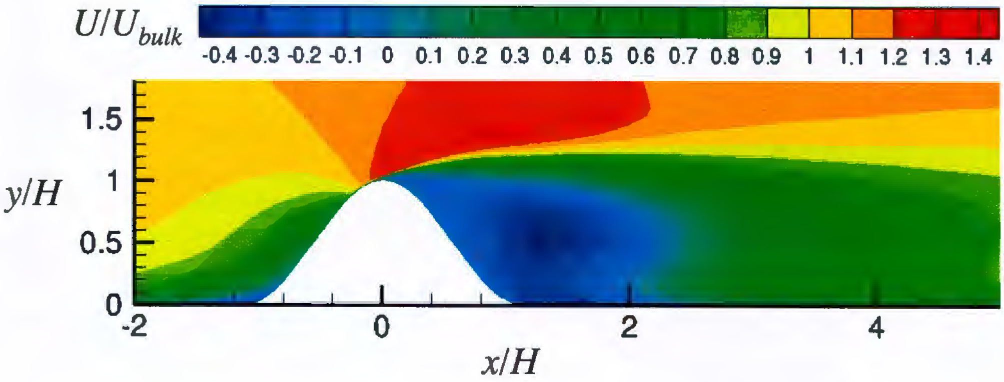

Figure 34: Contours of mean streamwise velocity at $z/H = 0$ from the case B3.

To illustrate the mean flow configuration across the bump, Figure 34 shows the mean streamwise velocity contours on the centerplane (i.e., $z/H = 0$) for case B3. The flow separates near the top of the bump ($x/H \approx 0$) and reattaches at $x/H \approx 2$, generating a large separation bubble behind the bump. Figures 35, 36, and 37 contain the mean streamwise velocity profiles at various streamwise locations for WMLES along with the reference experiment and LES data Ching *et al.* (2018*b*); Ching & Eaton (2020). At the upstream section of the bump (Figure 35) and windward side of the bump prior to the separated region (Figure 36(a)), WMLES predicts velocity profiles to within 1% error regardless of the mesh distribution. The good agreement of the mean velocity with LES data at the upstream section of the bump ($x/H = -4$) also verifies the adequacy of the inlet boundary condition generated by the synthetic turbulence.

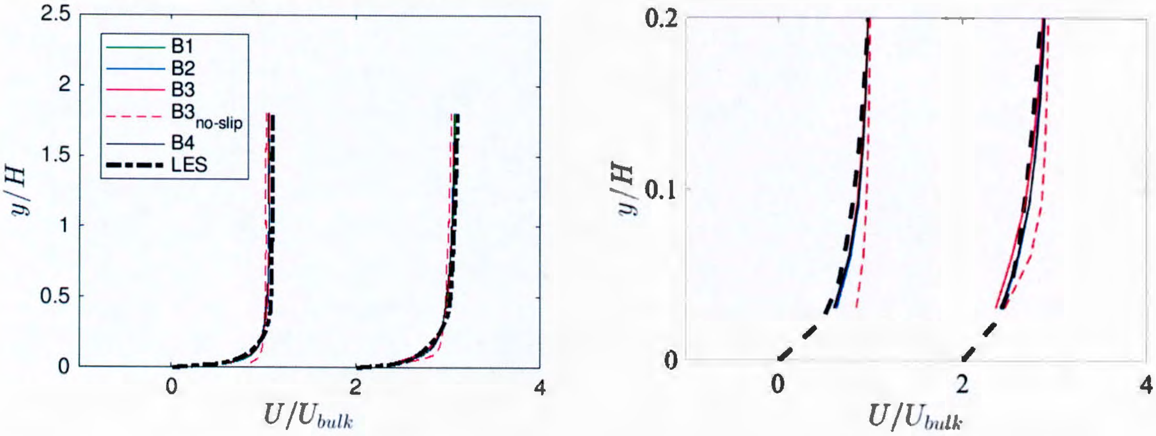

Figure 35: Mean velocity profiles in the upstream section of the bump at $x/H = -4$ and -2. Here, the profile at $x/H = -2$ is shifted by 2 on the horizontal axis. Lines, present WMLES (cases B1,B2,B3,B4); dashed lines, no-slip LES on the case B3 mesh (without wall model); dash-dot lines, LES Ching & Eaton (2020). Panel (a) shows the profiles up to $y/H = 1.7$, and panel (b) up to $y/H = 0.2$ to highlight the differences in the near-wall region.

Further downstream, the velocity profiles at the leeward side of the bump (Figure 36 (b)) and at $x/H = 3$ in the downstream section of the bump (Figure 37) are sensitive to the grid resolution. In case B1, the mean velocity distributions at the leeward side of the bump (Figure 36(b)) and at $x/H = 3$ (Figure 37) disagree with the reference experiment and LES by up to 20% error. These locations are inside and right behind the main separation bubble, respectively, where WMLES predictions are expected to be the most challenging. Nonetheless, the discrepancy between the WMLES and reference cases is greatly reduced with the additional grid refinements from cases B2-B4, bringing the predictions to within 1% agreement with the reference LES and experiments. Note that case B2 is set to contain the main separation bubble within the green-colored refined region and the case B3 is set to include additional grid cells around the separation point. Overall, the statistics from case B2 and case B3 show remarkable differences, while the statistics from case B3 are comparable to B4 as well as those from the reference studies. Consequently, resolving the thin separated shear layer near the apex (i.e., the blue refinement window in Figure 33) plays an important role in the successful prediction of the 3-D separated region. This is in agreement with

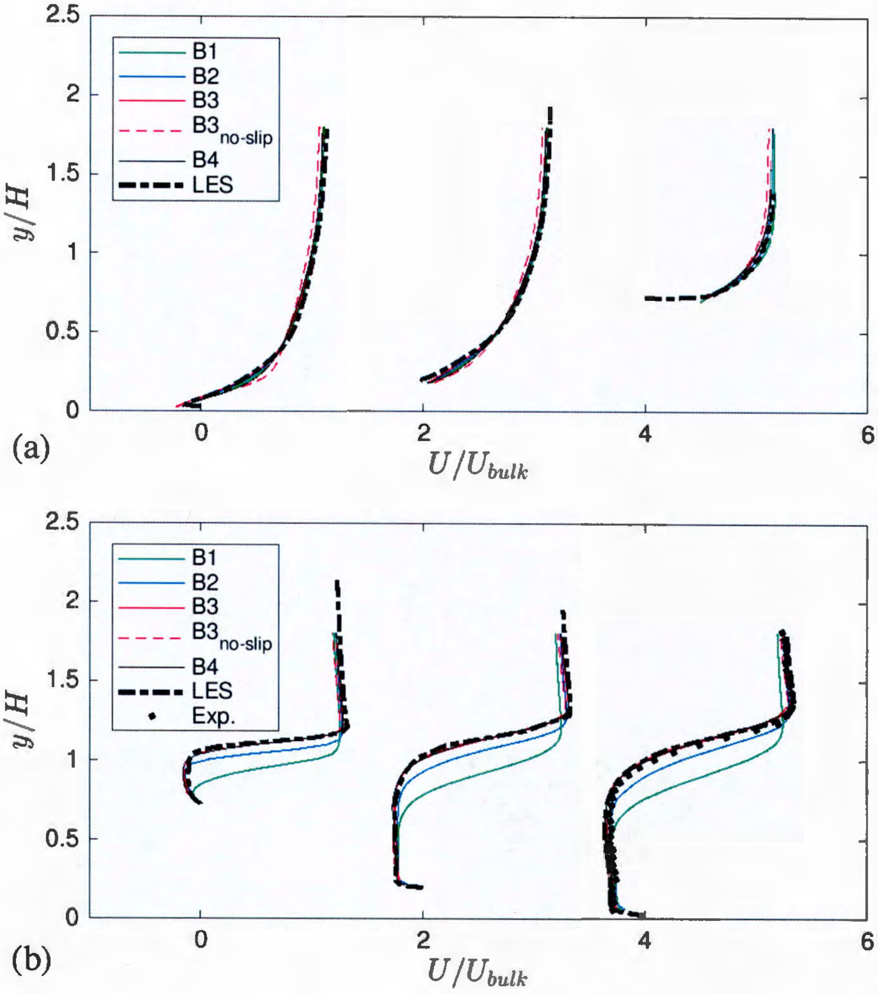

Figure 36: Mean velocity profiles over the bump: (a) windward side at $x/H = -1, -0.8$, and -0.4; (b) leeward side at $x/H = 0.4, 0.8$, and 1. Here, the profiles at $x/H = -0.8$ and 0.8 are shifted by 2 and the profiles at $x/H = -0.4$ and 1 are shifted by 4 on the horizontal axis, respectively. Lines, present WMLES (cases B1,B2,B3,B4); dashed lines, no-slip LES on the case B3 mesh (without wall model); dash-dot lines, LES Ching & Eaton (2020); circles, experiment Ching *et al.* (2018*b*).

previous WMLES studies in complex geometries Bose & Moin (2014); Park & Moin (2014); Kawai & Asada (2013); Park (2017), which have shown the importance of resolving separated shear layers with proper grid resolution to accurately capture the flow in their vicinity (Bose & Park, 2018). This observation is also consistent with the analysis from Lozano-Durán & Bae (2019), who showed that the errors incurred by WMLES in a given region of the flow scale with the mean shear. Finally, in the far downstream of the separation bubble at $x/H = 5$, the effect of the 3D separation is weakened and WMLES predicts velocity profiles for all mesh resolutions with reasonably good accuracy.

A better insight into the separation zone is shown in Figure 38, which portrays a zoomed-in view of the streamwise velocity contours at $z/H = 0$ from cases B1-B4. In the reference LES study Ching & Eaton (2020), the separation point on the centerplane was shown to

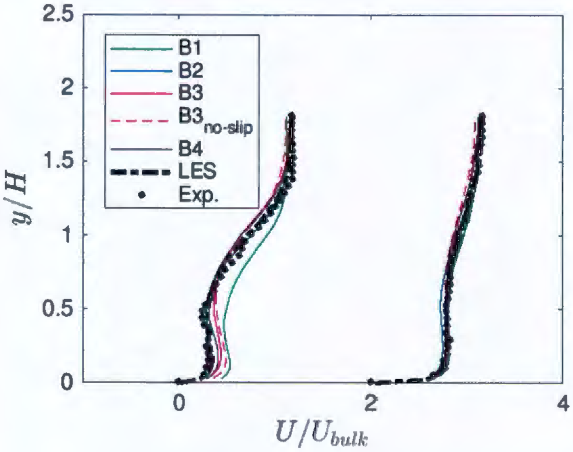

Figure 37: Mean velocity profiles in the downstream section of the bump at $x/H = 3$ and 5. Here, the profile at $x/H = 5$ is shifted by 2 on the horizontal axis. Lines, present WMLES (cases B1,B2,B3,B4); dashed lines, no-slip LES on the case B3 mesh (without wall model); dash-dot lines, LES Ching & Eaton (2020); circles, experiment Ching *et al.* (2018*b*).

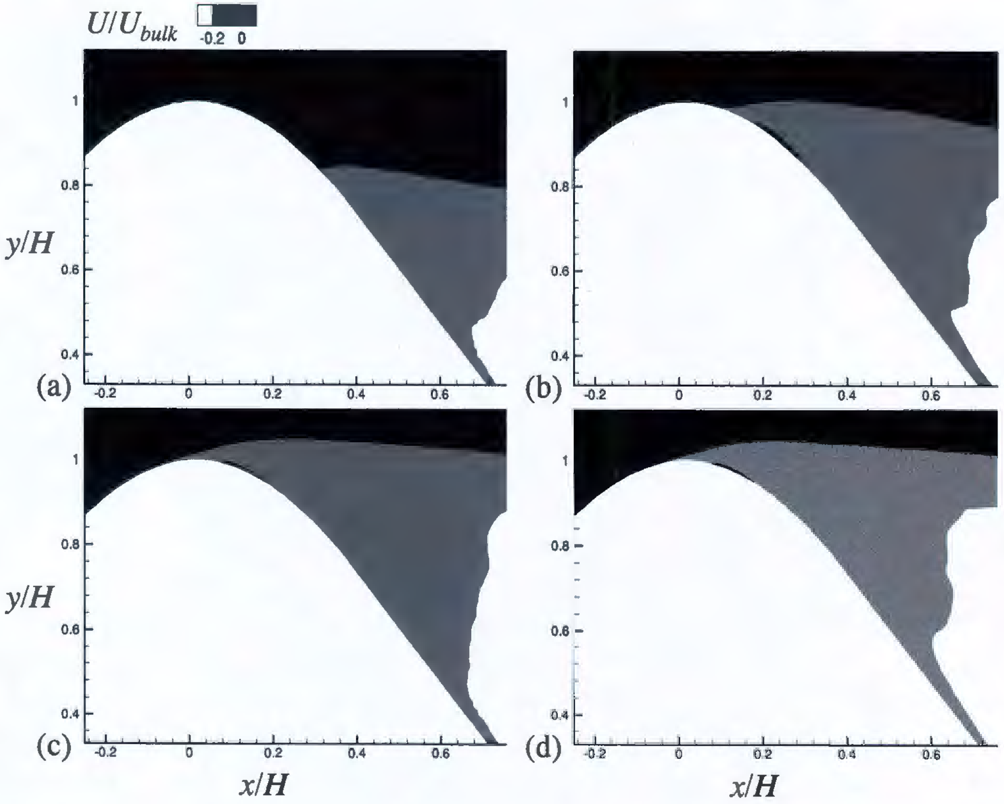

Figure 38: Contours of mean streamwise velocity at $z/H = 0$ showing the separation point and the secondary separation bubble: (a) case B1; (b) case B2; (c) case B3; (d) case B4.

be located around $x/H = 0$. Here, the separation point is delayed in cases B1 and B2, whereas B3 and B4 exhibit a similar separation point to that of Ching & Eaton (2020). The difference between figure 38 (b) and (c) highlights again the importance of resolving shear layer near the apex of the bump, which largely affects the bubble size and reattachment. In addition to the main large separation bubble discussed above, a thin secondary separation bubble was also observed at the leeside of the bump by Ching & Eaton (2020) in the range $0.1 < x/H < 0.3$. In WMLES, this secondary bubble is too thin to be accurately captured with the current grid resolution; however, Figure 38 shows that cases B2-B4 are able to capture an incipient separation zone.

For comparison, the velocity profiles from the no-slip LES (i.e., without the wall model) on the same mesh as B3 are also included Figures 35, 36, and 37 and denoted by $\mathrm{B3_{no-slip}}$ (red dashed lines). In the upstream section of the bump (Figure 35), $\mathrm{B3_{no-slip}}$ deviates slightly from WMLES and the experimental results in the near-wall region. However, velocity profiles over the bump (Figure 36) predicted from the no-slip LES coincide with those from B3. This indicates that the contribution of the equilibrium wall model in these regions is negligible, hence, the equilibrium wall model naturally deactivates in the separated region at the grid resolution of case B3. We can also argue that further grid refinements would most probably lead to similarly accurate results, as the ODE-based equilibrium wall model is consistent with the no-slip condition in the limit of $y^+ \to 0$. Consequently, the use of the equilibrium wall model in the present 3-D separated region does not hinder the performance of WMLES for grid resolutions equal or below those in B3. Finally, right after the separation bubble at $x/H = 3$, no-slip LES slightly underperforms the WMLES, but this deviation becomes marginal at $x/H = 5$ in Figure 37.

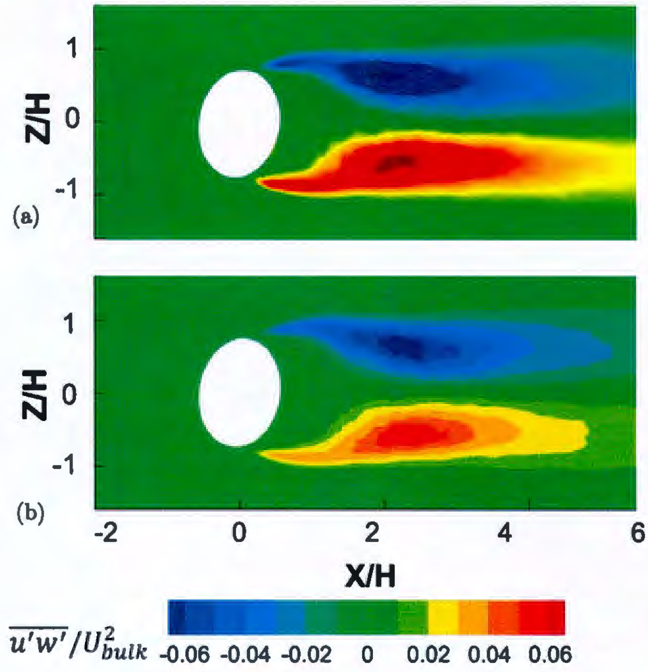

Figure 39: $\overline{u'w'}/U_{bulk}^2$ contours at $y/H = 0.5$: (a) WMLES from the case B3; (b) LES Ching & Eaton (2020).

Figure 39 compares the Reynolds shear stress ($\overline{u'w'}$) contours at $y/H = 0.5$ from the case B3 to the reference LES Ching & Eaton (2020). Ching & Eaton (2020) reported that these contours suggest spanwise movements of the wake, because positive streamwise fluctuations are correlated with spanwise fluctuations toward the centerline. The Reynolds shear stress contours predicted from the WMLES show reasonable agreement with the LES, implying that the flow physics in the bump wake region is accurately captured.

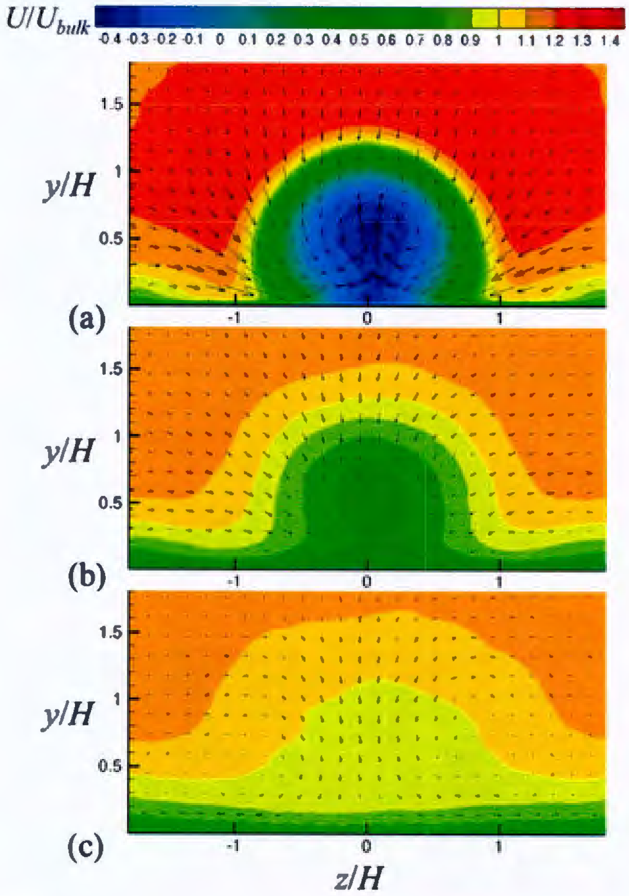

Figure 40: Mean streamwise velocity contours with in-plane velocity vectors from the case B3: (a) $x/H = 1.5$; (b) $x/H = 4$; (c) $x/H = 8$.

Figure 40 illustrates the vortex structures downstream the bump. As reported in previous studies Ching *et al.* (2018*b*,*a*); Ching & Eaton (2020), a common-up vortex pair is captured in the separation bubble right behind the bump. This vortex pair evolves into a common-down vortex pair in the far downstream at $x/H = 4.0$. Not only the mean structures, but also the shedding frequency behind the bump is captured in the current WMLES as shown by the velocity power spectra from the probes in the wake region in Figure 41. Following Ching *et al.* (2018*b*); Ching & Eaton (2020), the Strouhal number is defined as

$$St = \frac{f\sqrt{A_b}}{U_{\mathrm{bulk}}}, \tag{33}$$

where f is the shedding frequency, A_b is the blockage area, and U_{bulk} is the bulk velocity. The shedding frequency from the WMLES matches the reference LES.

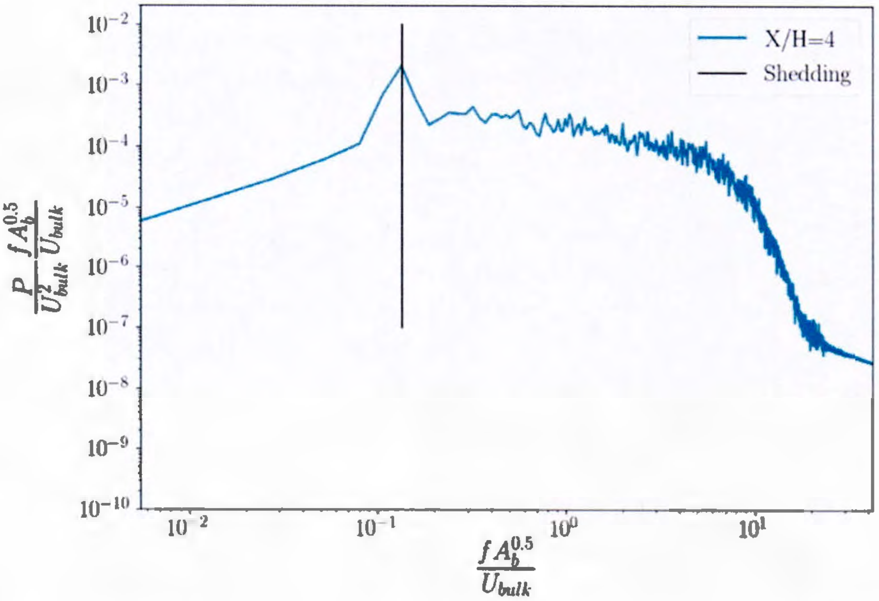

Figure 41: Velocity power spectra in the wake region from the case B3. The vertical line denotes Strouhal number from LES Ching & Eaton (2020).

4.3 Conclusions

We have investigated the performance of wall-modeled LES in predicting turbulent boundary layers with mean-flow three-dimensionality using an ODE-based equilibrium wall model. Two cases were considered: a spatially-developing 3DTBL inside a bent square duct Schwarz & Bradshaw (1994) and 3-D separated flows in a skewed bump Ching *et al.* (2018*b*,*a*); Ching & Eaton (2020). In the square duct simulation, WMLES was capable of predicting mean velocity profiles and crossflow angles in the outer region of the flow to within 1–5% error using ten points per boundary layer thickness. However, 20% error was observed in the cross-flow angles near the wall in the bend region where the non-equilibrium effects are most significant. This error persisted with increased grid resolution implying that grid refinement alone without the use of non-equilibrium wall models may not improve the solution in the presence of skewed mean velocity profiles in the near wall region. WMLES of the wall-mounted skewed bump showed that the ODE-based equilibrium wall model with a grid resolution of about forty points across the 3-D separation region predicts mean velocity profiles, shedding frequency, and separation location to within 13% error. Grid refinement analysis of the bump simulations showed that resolving the incipient flow separation and associated thin shear layer is crucial to attain accurate predictions. Within the separation zone, our results indicate that WMLES performs well, and reverting to no-slip boundary condition is not necessary provided adequate grid resolution is used across the bubble.

5 Summary

Non-equilibrium wall turbulence with mean-flow three-dimensionality is ubiquitous in geophysical and engineering flows. Under these conditions, turbulence may experience a counter-intuitive depletion of the turbulent stresses, which has important implications for modelling and control. Yet, current turbulence theories have been established mainly for statistically two-dimensional equilibrium flows and are unable to predict the reduction in the Reynolds stress magnitude. We have proposed a multiscale model which captures the response of non-equilibrium wall-bounded turbulence under the imposition of three-dimensional strain. The analysis is performed via direct numerical simulation of transient three-dimensional turbulent channels subjected to a sudden lateral pressure gradient at friction Reynolds numbers up to 1,000. We show that the flow regimes and scaling properties of the Reynolds stress are consistent with a model comprising momentum-carrying eddies with sizes and time scales proportional to their distance to the wall. We have further demonstrated that the reduction in Reynolds stress follows a spatially and temporally self-similar evolution caused by the relative horizontal displacement between the core of the momentum-carrying eddies and the flow layer underneath. Inspection of the flow energetics reveals that this mechanism is associated with lower levels of pressure-strain correlation which ultimately inhibits the generation of Reynolds stress, consistent with previous works. Finally, we have assessed the ability of the state-of-the-art wall-modelled large-eddy simulation to predict non-equilibrium, three-dimensional flows.

We have also examined the performance of wall-modeled large-eddy simulation (WMLES) to predict turbulent boundary layers (TBLs) with mean-flow three-dimensionality. The analysis was performed for an ordinary-differential-equation-based equilibrium wall model due to its widespread use and ease of implementation. Two test cases are considered for this purpose: a spatially-developing TBL in a square duct with a 30-degree bend, and the flow behind a wall-mounted skewed bump with a three-dimensional separation bubble. In the duct simulation, WMLES is capable of predicting mean velocity profiles and crossflow angles in the outer region of the flow to within 1–5% error using ten points per boundary layer thickness. The largest disagreement (20% error) is observed in the crossflow angles in the bend region, where three-dimensional effects are the most significant. In the skewed bump simulation, it is shown that the present equilibrium wall-model with a grid resolution of about forty points across the 3-D separation region predicts mean velocity profiles, separation location to within 1–3% error. The bubble size and vortex structures in the bump wake are also correctly represented. It is demonstrated that WMLES is capable of achieving accurate results in the separated region and its vicinity, provided that the strong shear layer generated at the apex of the bump is well-resolved.

References

ADRIAN, R. J., MEINHART, C. D. & TOMKINS, C. D. 2000 Vortex organization in the outer region of the turbulent boundary layer. *J. Fluid Mech.* **422**, 1–54.

AGOSTINI, LIONEL & LESCHZINER, MICHAEL 2017 Spectral analysis of near-wall turbulence in channel flow at $\mathrm{Re}_\tau = 4200$ with emphasis on the attached-eddy hypothesis. *Phys. Rev. Fluids* **2**, 014603.

DEL ÁLAMO, J. C. & JIMÉNEZ, J. 2006 Linear energy amplification in turbulent channels. *J. Fluid Mech.* **559**, 205–213.

DEL ÁLAMO, J. C., JIMÉNEZ, J., ZANDONADE, P. & MOSER, R. D. 2004 Scaling of the energy spectra of turbulent channels. *J. Fluid Mech.* **500**, 135–144.

ANDERSON, SHAWN D & EATON, JOHN K 1987 Experimental study of a pressure-driven, three-dimensional, turbulent boundary layer. *AIAA J.* **25** (8), 1086–1092.

ANDERSON, SHAWN D & EATON, JOHN K 1989 Reynolds stress development in pressure-driven three-dimensional turbulent boundary layers. *J. Fluid Mech.* **202**, 263–294.

BAARS, W.J., HUTCHINS, N. & MARUSIC, I. 2017 Self-similarity of wall-attached turbulence in boundary layers. *J. Fluid Mech.* **823**.

BAE, H J, LOZANO-DURÁN, A, BOSE, S T & MOIN, P 2018*a* Dynamic slip wall model for large-eddy simulation. *J. Fluid Mech.* **859**, 400–432.

BAE, H. J., LOZANO-DURÁN, A., BOSE, S. T. & MOIN, P. 2018*b* Dynamic wall model for the slip boundary condition in large-eddy simulation. *J. Fluid Mech.* pp. 400–432.

BAE, H. J., LOZANO-DURÁN, A., BOSE, S. T. & MOIN, P. 2018*c* Turbulence intensities in large-eddy simulation of wall-bounded flows. *Phys. Rev. Fluids* **3**, 014610.

BALARAS, E., BENOCCI, C. & PIOMELLI, U. 1996 Two-layer approximate boundary conditions for large-eddy simulations. *AIAA J.* **34** (6), 1111–1119.

VAN DEN BERG, B & ELSENAAR, A 1972 Measurements in a three-dimensional incompressible turbulent boundary layer in an adverse pressure gradient under infinite swept wing conditions. *Tech. Rep.*. Nationaal Lucht-en Ruimtevaartlaboratorium.

VAN DEN BERG, B, ELSENAAR, A, LINDHOUT, JPF & WESSELING, P 1975 Measurements in an incompressible three-dimensional turbulent boundary layer, under infinite swept-wing conditions, and comparison with theory. *J. Fluid Mech.* **70** (1), 127–148.

VAN DEN BERG, BERNARD, LINDHOUT, JAN PIETER FLORIS, HUMPHREYS, DAVID ANTHONY & KRAUSE, EGON 1988 Three-dimensional turbulent boundary layers-calculations and experiments. In *Brunswick, Federal Republic of Germany, Friedr. Vieweg und Sohn (Notes on Numerical Fluid Mechanics. Volume 19), 1988, 168 p.*, , vol. 19.

BISSONNETTE, LUC R & MELLOR, GEORGE L 1974 Experiments on the behaviour of an axisymmetric turbulent boundary layer with a sudden circumferential strain. *J. Fluid Mech.* **63** (2), 369–413.

Bodart, J. & Larsson, J. 2011 Wall-modeled large eddy simulation in complex geometries with application to high-lift devices. *Center for Turbulence Research - Annual Research Briefs* pp. 37–48.

Bodart, J & Larsson, J 2012 Sensor-based computation of transitional flows using wall-modeled large eddy simulation. *Annual Research Briefs, Center for Turbulence Research, Stanford University* pp. 229–240.

Bogard, D G & Tiederman, W G 1986 Burst detection with single-point velocity measurements. *J. Fluid Mech* **162**, 389–413.

Bose, S T & Moin, P 2014 A dynamic slip boundary condition for wall-modeled large-eddy simulation. *Phys. Fluids* **26**, 015104.

Bose, S T & Park, G I 2018 Wall-modeled large-eddy simulation for complex turbulent flows. *Annu. Rev. Fluid Mech.* **5**, 535–561.

Bou-Zeid, Elie, Meneveau, Charles & Parlange, Marc 2005 A scale-dependent lagrangian dynamic model for large eddy simulation of complex turbulent flows. *Phys. Fluids* **17** (2), 025105.

Bradshaw, P & Pontikos, NS 1985 Measurements in the turbulent boundary layer on an 'infinite' swept wing. *J. Fluid Mech.* **159**, 105–130.

Bradshaw, P & Terrell, MG 1969 The response of a turbulent boundary layer on an 'infinite' swept wing to the sudden removal of pressure gradient. *NPL Aero Report* **1305**.

Brès, G A, Bose, S T, Emory, M, Ham, F E, Schmidt, O T, Rigas, G & Colonius, T 2018 Large-eddy simulations of co-annular turbulent jet using a voronoi-based mesh generation framework. *AIAA Paper* **2018-3302**, 1–13.

Castillo, Luciano & George, William K. 2001 Similarity analysis for turbulent boundary layer with pressure gradient: Outer flow. *AIAA J.* **39** (1), 41–47.

Chandran, Dileep, Baidya, Rio, Monty, Jason P. & Marusic, Ivan 2017 Two-dimensional energy spectra in high-Reynolds-number turbulent boundary layers. *J. Fluid Mech.* **826**, R1.

Chandrashekar, P 2013 Kinetic energy preserving and entropy stable finite volume schemes for compressible euler and navier-stokes equations. *Commun. Comput. Phys.* **14**, 1252–1286.

Chapman, D R 1979 Computational aerodynamics development and outlook. *AIAA J.* **17**, 1293–1313.

Cheng, Cheng, Li, Weipeng, Lozano-Durán, Adrián & Liu, Hong 2019 Identity of attached eddies in turbulent channel flows with bidimensional empirical mode decomposition. *J. Fluid Mech.* **870**, 1037–1071.

Chiang, C & Eaton, JK 1996 An experimental study of the effects of three-dimensionality on the near wall turbulence structures using flow visualization. *Exp. Fluids* **20** (4), 266–272.

Ching, D S & Eaton, J K 2020 Large-eddy simulation study of unsteady wake dynamics and geometric sensitivity on a skewed bump. *J. Fluid Mech.* **885**, A22.

Ching, D S, Elkins, C J, Alley, M T & Eaton, J K 2018*a* Unsteady vortex structures in the wake of nonaxisymmetric bumps using spiral mrv. *Exp. in Fluids* **59** (144) 1–17.

Ching, D S, Elkins, C J & Eaton, J K 2018*b* Investigation of geometric sensitivity of a non-axisymmetric bump: 3d mean velocity measurements. *Exp. in Fluids* **59** (143), 1–14.

Cho, M, Park, G I, Lozano-Durán, A & Moin, P 2019 Wall-modeled large-eddy simulation ofnon-equilibrium turbulent boundary layers. *Annual Research Briefs, Center for Turbulence Research, Stanford University* pp. 15–28.

Cho, M, Park, G I & Moin, P 2018 Wall-modeled les of a spatially-developing non-equilibrium turbulent boundary layer. *Annual Research Briefs, Center for Turbulence Research, Stanford University* pp. 251–259.

Choi, H & Moin, P 2012 Grid-point requirements for large eddy simulation: Chapmans estimates revisited. *Phys. Fluids* **24**, 011702.

Choi, Jung-Il, Xu, Chun-Xiao & Sung, Hyung Jin 2002 Drag reduction by spanwise wall oscillation in wall-bounded turbulent flows. *AIAA J.* **40** (5), 842–850.

Choi, Kwing-So & Clayton, Brian R 2001 The mechanism of turbulent drag reduction with wall oscillation. *Int. J. Heat Fluid Fl.* **22** (1), 1 – 9.

Chorin, Alexandre Joel 1968 Numerical Solution of the Navier-Stokes Equations. *Math. Comput.* **22** (104), 745–762.

Coleman, Gary Neil, Ferziger, JH & Spalart, PR 1990 A numerical study of the turbulent Ekman layer. *J. Fluid Mech.* **213**, 313–348.

Coleman, Gary N, Kim, John & Le, Anh-Tuan 1996*a* A numerical study of three-dimensional wall-bounded flows. *Int. J. Heat Fluid Fl.* **17** (3), 333–342.

Coleman, Gary N., Kim, John & Spalart, Philippe R. 1996*b* Direct numerical simulation of strained three-dimensional wall-bounded flows. *Exp. Therm. Fluid Sci.* **13** (3), 239 – 251.

Coleman, G. N., Kim, J. & Spalart, P. R. 2000 A numerical study of strained three-dimensional wall-bounded turbulence. *J. Fluid Mech.* **416**, 75–116.

Coles, D. E. & Hirst, Eric. 1969 Computation of turbulent boundary layers; 1968 AFOSR-IFP-Stanford Conference.

Compton, Debora A & Eaton, John K 1997 Near-wall measurements in a three-dimensional turbulent boundary layer. *J. Fluid Mechanics* **350**, 189–208.

Cossu, Carlo & Hwang, Yongyun 2017 Self-sustaining processes at all scales in wall-bounded turbulent shear flows. *Philos. Trans. Royal Soc. A* **375** (2089).

Davidson, P. A., Nickels, T. B. & Krogstad, P.-Å. 2006 The logarithmic structure function law in wall-layer turbulence. *J. Fluid Mech.* **550**, 51–60.

De Graaff, D. B. & Eaton, J. K. 2000 Reynolds-number scaling of the flat-plate turbulent boundary layer. *J. Fluid Mech.* **422**, 319–346.

Del Álamo, J. C., Jiménez, J., Zandonade, P & Moser, Robert D. 2006 Self-similar vortex clusters in the turbulent logarithmic region. *J. Fluid Mech.* **561**, 329–358.

Dong, S., Lozano-Durán, A., Sekimoto, A. & Jiménez, J. 2017 Coherent structures in statistically stationary homogeneous shear turbulence. *J. Fluid Mech.* **816**, 167–208.

Driver, David M & Hebbar, Sheshagiri K 1987 Experimental study of a three-dimensional, shear-driven, turbulent boundary layer. *AIAA J.* **25** (1), 35–42.

Driver, David M & Hebbar, Sheshagiri K 1989 Three-dimensional shear-driven boundary-layer flow with streamwise adverse pressure gradient. *AIAA J.* **27** (12), 1689–1697.

Driver, David M & Hebbar, Sheshagiri K 1991 Three-dimensional turbulent boundary layer flow over a spinning cylinder. *NASA Ames Research Center Technical Report* .

Durbin, Paul A. 2018 Some recent developments in turbulence closure modeling. *Annu. Rev. Fluid Mech.* **50** (1), 77–103.

Eaton, JK 1991 Turbulence structure and heat transfer in three-dimensional boundary layers. In *Proceedings of the 9th Symposium on Energy Engineering Sciences*.

Eaton, John K 1995 Effects of mean flow three dimensionality on turbulent boundary-layer structure. *AIAA J.* **33** (11), 2020–2025.

Elsenaar, A & Boelsma, SH 1974 Measurements of the Reynolds stress tensor in a three-dimensional turbulent boundary layer under infinite swept wing conditions. *Tech. Rep.*. Nationaal Lucht-en Ruimtevaartlaboratorium.

Farrell, B F, Gayme, D F & Ioannou, P J 2017 A statistical state dynamics approach to wall turbulence. *Philos. Trans. Royal Soc. A* **375** (2089), 20160081.

Farrell, Brian F., Ioannou, Petros J., Jiménez, Javier, Constantinou, Navid C., Lozano-Durán, Adrián & Nikolaidis, Marios-Andreas 2016 A statistical state dynamics-based study of the structure and mechanism of large-scale motions in plane poiseuille flow. *J. Fluid Mech.* **809**, 290–315.

Fernholz, HH & Vagt, J-D 1981 Turbulence measurements in an adverse-pressure-gradient three-dimensional turbulent boundary layer along a circular cylinder. *J. Fluid Mech.* **111**, 233–269.

Flack, Karen & Johnston, James 1994 Near-wall flow in a three-dimensional turbulent boundary layer on the endwall of a rectangular bend. In *32nd Aerospace Sciences Meeting and Exhibit*, p. 405.

Flack, Karen Ashby 1993 Near wall investigation of three dimensional turbulent boundary layers. *Stanford University Thermosciences Div. Rep.* pp. MD–63.

Flores, O. & Jiménez, J. 2010 Hierarchy of minimal flow units in the logarithmic layer. *Phys. Fluids* **22** (7), 071704.

Furuya, M. & Fujita, H. 1966 Turbulent boundary layer over rough gauze surfaces. *Trans. Japan Soc. Mech. Engrs* **32**, 725.

GANAPATHISUBRAMANI, B. 2008 Statistical structure of momentum sources and sinks in the outer region of a turbulent boundary layer. *J. Fluid Mech.* **606**, 225–237.

GIOMETTO, M G, LOZANO-DURÁN, A, PARK, G I & MOIN, P 2017 Three-dimensional transient channel flow at moderate reynolds numbers: Analysis and wall modeling. *Annual Research Briefs* pp. 193–205.

HACK, M. J. PHILIPP & ZAKI, TAMER A. 2015 Modal and non-modal stability of boundary layers forced by spanwise wall oscillations. *J. Fluid Mech.* **778**, 389–427.

HE, S., LOZANO-DURÁN, A., HE, J. & CHO, M. 2018 Turbulent-turbulent transition of a transient three-dimensional channel flow. *Center for Turbulence Research - Proceedings of the Summer Program* pp. 257–266.

HE, S. & SEDDIGHI, M. 2013 Turbulence in transient channel flow. *J. Fluid Mech.* **715**, 60–102.

HE, S. & SEDDIGHI, M. 2015 Transition of transient channel flow after a change in Reynolds number. *J. Fluid Mech.* **764**, 395–427.

HELLSTRÖM, LEO.H.O., MARUSIC, I. & SMITS, A.J. 2016 Self-similarity of the large-scale motions in turbulent pipe flow. *J. Fluid Mech.* **792**, R1.

HERRMANN, MARCUS 2010 Detailed numerical simulations of the primary atomization of a turbulent liquid jet in crossflow. *J. Eng. Gas Turb. Power* **132** (6), 061506–061506–10.

HOLSTAD, A., ANDERSSON, H. I. & PETTERSEN, B. 2010 Turbulence in a three-dimensional wall-bounded shear flow. *Int. J. Numer. Meth. Fl.* **62** (8), 875–905.

HOWARD, RJA & SANDHAM, ND 1997 Simulation and modelling of the skew response of turbulent channel flow to spanwise flow deformation. In *Direct and Large-Eddy Simulation II*, pp. 213–224. Springer.

HOYAS, S. & JIMÉNEZ, J. 2006 Scaling of the velocity fluctuations in turbulent channels up to $Re_\tau = 2003$. *Phys. Fluids* **18** (1), 011702.

HU, X, CHO, M & PARK, G I 2019 Wall-modeled les of 3d turbulent boundary layer in a square duct with a 30° bend. *72nd Annual Meeting of the APS Division of Fluid Dynamics* .

HWANG, J. & SUNG, H.J. 2018 Wall-attached structures of velocity fluctuations in a turbulent boundary layer. *J. Fluid Mech.* **856**, 958–983.

HWANG, Y. 2015 Statistical structure of self-sustaining attached eddies in turbulent channel flow. *J. Fluid Mech.* **767**, 254–289.

HWANG, Y. & BENGANA, Y. 2016 Self-sustaining process of minimal attached eddies in turbulent channel flow. *J. Fluid Mech.* **795**, 708–738.

HWANG, Y. & COSSU, C. 2010 Self-sustained process at large scales in turbulent channel flow. *Phys. Rev. Lett.* **105**, 044505.

HWANG, YONGYUN & COSSU, CARLO 2011 Self-sustained processes in the logarithmic layer of turbulent channel flows. *Phys. Fluids* **23** (6), 061702.

Jiménez, J. 2018 Coherent structures in wall-bounded turbulence. *J. Fluid Mech.* **842**, P1.

Jiménez, J. & Moin, P. 1991 The minimal flow unit in near-wall turbulence. *J. Fluid Mech.* **225**, 213–240.

Jiménez, J. & Pinelli, A. 1999 The autonomous cycle of near-wall turbulence. *J. Fluid Mech.* **389**, 335–359.

Johnston, James P 1970 Measurements in a three-dimensional turbulent boundary layer induced by a swept, forward-facing step. *J. Fluid Mech.* **42** (4), 823–844.

Johnston, J. P. & Flack, K. A. 1996 Review—advances in three-dimensional turbulent boundary layers with emphasis on the wall-layer regions. *J. Fluids Eng.* **118** (2), 219–232.

Jung, Seo Yoon & Sung, Hyung Jin 2006 Characterization of the three-dimensional turbulent boundary layer in a concentric annulus with a rotating inner cylinder. *Phys. Fluids* **18** (11), 115102.

Jung, WJ, Mangiavacchi, N & Akhavan, R 1992 Suppression of turbulence in wall-bounded flows by high-frequency spanwise oscillations. *Phys. Fluids* **4** (8), 1605–1607.

Kannepalli, Chandrasekhar & Piomelli, Ugo 2000 Large-eddy simulation of a three-dimensional shear-driven turbulent boundary layer. *J. Fluid Mech.* **423**, 175–203.

Kawahara, Genta, Uhlmann, Markus & van Veen, Lennaert 2012 The significance of simple invariant solutions in turbulent flows. *Annu. Rev. Fluid Mech.* **44** (1), 203–225.

Kawai, S & Asada, K 2013 Wall-modeled large-eddy simulation of high reynolds number flow around an airfoil near stall condition. *Comput. Fluids* **85**, 105–113.

Kawai, S & Larsson, J 2012 Wall-modeling in large eddy simulation: length scales, grid resolution, and accuracy. *Phys. Fluids* **24**, 015015.

Khalighi, Yaser, Ham, Frank, Nichols, Joseph, Lele, Sanjiva & Moin, Parviz 2011 *Unstructured Large Eddy Simulation for Prediction of Noise Issued from Turbulent Jets in Various Configurations*. AIAA.

Kiesow, Robert O & Plesniak, Michael W 2002 Modification of near-wall structure in a shear-driven 3-d turbulent boundary layer. *J. Fluids Eng.* **124** (1), 118–126.

Kiesow, Robert O. & Plesniak, Michael W. 2003 Near-wall physics of a shear-driven three-dimensional turbulent boundary layer with varying crossflow. *J. Fluid Mech.* **484**, 1–39.

Kim, J., Moin, P. & Moser, R. 1987 Turbulence statistics in fully developed channel flow at low Reynolds number. *J. Fluid Mech.* **177** (1), 133–166.

Klewicki, Joe, Fife, Paul, Wei, Tie & McMurtry, Pat 2007 A physical model of the turbulent boundary layer consonant with mean momentum balance structure. *Philos. Trans. Royal Soc. A* **365** (1852), 823–840.

Laadhari, F, Skandaji, L & Morel, R 1994 Turbulence reduction in a boundary layer by a local spanwise oscillating surface. *Phys. Fluids* **6** (10), 3218–3220.

LARSSON, J, KAWAI, S, BODART, J & BERMEJO-MORENO, I 2016 Large eddy simulation with modeled wall-stress: recent progress and future directions. *Mech. Eng. Rev.* **3**, 15–00418.

LE, ANH-TUAN 1999 A numerical study of three-dimensional turbulent boundary layers. PhD thesis, University of California.

LE, ANH-TUAN, COLEMAN, GARY N & KIM, JOHN 1999 Near-wall turbulence structures in three-dimensional boundary layers. In *Proc. First Intl Symp. on Turbulence and Shear Flow Phenomena*, pp. 147–152.

LEE, MYOUNGKYU & MOSER, ROBERT D. 2015 Direct numerical simulation of turbulent channel flow up to $Re_\tau \approx 5200$. *J. Fluid Mech.* **774**, 395–415.

LESGO 2019 A parallel pseudo-spectral large-eddy simulation code. https://lesgo.me.jhu.edu.

LILLY, D. K. 1992 A proposed modification of the Germano subgrid-scale closure method. *Phys. Fluids A* **4** (3), 633–635.

LITTELL, HOWARD S. & EATON, JOHN K. 1994 Turbulence characteristics of the boundary layer on a rotating disk. *J. Fluid Mech.* **266**, 175–207.

LOHMANN, ROBERT P 1976 The response of a developed turbulent boundary layer to local transverse surface motion. *J. Fluids Eng.* **98** (3), 354–363.

LOZANO-DURÁN, A., BAE, H.J., BOSE, S.T. & MOIN, P. 2017 Dynamic wall models for the slip boundary condition. *Center for Turbulence Research - Annual Research Briefs* pp. 229–242.

LOZANO-DURÁN, A. & BAE, H. J. 2016 Turbulent channel with slip boundaries as a benchmark for subgrid-scale models in LES. *Annual Research Briefs, Center for Turbulence Research, Stanford University* pp. 97–103.

LOZANO-DURÁN, ADRIÁN & BAE, HYUNJI JANE 2019 Error scaling of large-eddy simulation in the outer region of wall-bounded turbulence. *J. Comput. Phys.* **392**, 532–555.

LOZANO-DURÁN, ADRIÁN, BAE, H. JANE & ENCINAR, MIGUEL P. 2020*a* Causality of energy-containing eddies in wall turbulence. *J. Fluid Mech.* **882**, A2.

LOZANO-DURÁN, A. & BORRELL, G. 2016 Algorithm 964: An efficient algorithm to compute the genus of discrete surfaces and applications to turbulent flows. *ACM Trans. Math. Softw.* **42** (4), 34:1–34:19.

LOZANO-DURÁN, ADRIÁN, BOSE, SANJEEB T. & MOIN, PARVIZ 2020*b* *Prediction of trailing edge separation on the NASA Juncture Flow using wall-modeled LES*, p. 1776. AIAA Scitech 2020 Forum.

LOZANO-DURÁN, A., FLORES, O. & JIMÉNEZ, J. 2012 The three-dimensional structure of momentum transfer in turbulent channels. *J. Fluid Mech.* **694**, 100–130.

LOZANO-DURÁN, A, GIOMETTO, M G, PARK, G I & MOIN, P 2020 Non-equilibrium three-dimensional boundary layers at moderate reynolds numbers. *J. Fluid Mech.* **883**, A20.

Lozano-Durán, A., Hack, M. J. P. & Moin, P. 2018 Modeling boundary-layer transition in direct and large-eddy simulations using parabolized stability equations. *Phys. Rev. Fluids* **3**, 023901.

Lozano-Durán, A. & Jiménez, J. 2014*a* Effect of the computational domain on direct simulations of turbulent channels up to $Re_\tau = 4200$. *Phys. Fluids* **26** (1), 011702.

Lozano-Durán, A. & Jiménez, J. 2014*b* Time-resolved evolution of coherent structures in turbulent channels: characterization of eddies and cascades. *J. Fluid Mech.* **759**, 432–471.

Maciel, Yvan, Rossignol, Karl-Stéphane & Lemay, Jean 2006 Self-similarity in the outer region of adverse-pressure-gradient turbulent boundary layers. *AIAA J.* **44** (11), 2450–2464.

Maciel, Yvan, Wei, Tie, Gungor, Ayse G. & Simens, Mark P. 2018 Outer scales and parameters of adverse-pressure-gradient turbulent boundary layers. *J. Fluid Mech.* **844**, 5–35.

Mansour, N. N., Kim, J. & Moin, P. 1988 Reynolds-stress and dissipation-rate budgets in a turbulent channel flow. *J. Fluid Mech.* **194**, 15–44.

Marusic, Ivan & Monty, Jason P. 2019 Attached eddy model of wall turbulence. *Annu. Rev. Fluid Mech.* **51** (1), 49–74.

Marusic, I., Monty, J. P., Hultmark, M. & Smits, A. J. 2013 On the logarithmic region in wall turbulence. *J. Fluid Mech.* **716**, R3.

Mathur, A., Gorji, S., He, S., Seddighi, M., Vardy, A. E., ODonoghue, T. & Pokrajac, D. 2018 Temporal acceleration of a turbulent channel flow. *J. Fluid Mech.* **835**, 471–490.

McKeon, B. J. 2017 The engine behind (wall) turbulence: perspectives on scale interactions. *J. Fluid Mech.* **817**, P1.

Meneveau, Charles & Marusic, Ivan 2013 Generalized logarithmic law for high-order moments in turbulent boundary layers. *J. Fluid Mech.* **719**, R1.

Millikan, C. B. 1938 A critical discussion of turbulent flows in channels and circular tubes. In *Proceedings* 5th *Int. Congr. Applied Mechanics, New York* (ed. J. P. Den Hartog & H. Peters), pp. 386–392. Wiley.

Mizuno, Y. & Jiménez, J. 2011 Mean velocity and length-scales in the overlap region of wall-bounded turbulent flows. *Phys. Fluids* **23** (8), 085112.

Moin, P., Shih, T.H., Driver, D. & Mansour, N. N. 1990 Direct numerical simulation of a three-dimensional turbulent boundary layer. *Phys. Fluids* **2** (10), 1846–1853.

Moin, P., Squires, K., Cabot, W. & Lee, S. 1991 A dynamic subgrid-scale model for compressible turbulence and scalar transport. *Phys. Fluids* **3** (11), 2746–2757.

Moisy, F. & Jiménez, J. 2004 Geometry and clustering of intense structures in isotropic turbulence. *J. Fluid Mech.* **513**, 111–133.

Monkewitz, Peter A., Chauhan, Kapil A. & Nagib, Hassan M. 2008 Comparison of mean flow similarity laws in zero pressure gradient turbulent boundary layers. *Phys. Fluids* **20** (10), 105102.

Morrison, J. F., McKeon, B. J., Jiang, W. & Smits, A. J. 2004 Scaling of the streamwise velocity component in turbulent pipe flow. *J. Fluid Mech.* **508**, 99–131.

Ölçmen, MS & Simpson, RL 1992 Perspective: On the near wall similarity of three-dimensional turbulent boundary layers (data bank contribution). *J. Fluids Eng.* **114** (4), 487–495.

Ölçmen, Semİh M & Simpson, Roger L 1995 An experimental study of a three-dimensional pressure-driven turbulent boundary layer. *J. Fluid Mech.* **290**, 225–262.

Orlandi, P. 2000 *Fluid Flow Phenomena: A Numerical Toolkit*. Springer.

Osawa, Kosuke & Jiménez, Javier 2018 Intense structures of different momentum fluxes in turbulent channels. *Phys. Rev. Fluids* **3**, 084603.

Panton, R.L. 1984 *Incompressible Flow*. Wiley.

Panton, R. L. 2001 Overview of the self-sustaining mechanisms of wall turbulence. *Prog. Aerosp. Sci.* **37** (4), 341–383.

Park, G I 2017 Wall-modeled large-eddy simulation of a high reynolds number separating and reattaching flow. *AIAA J.* **55**, 3709–3721.

Park, G I & Moin, P 2014 An improved dynamic non-equilibrium wall-model for large eddy simulation. *Phys. Fluids* **26**, 015108.

Park, G I & Moin, P 2016 Numerical aspects and implementation of a two-layer zonal wall model for les of compressible turbulent flows on unstructured meshes. *J. Comput. Phys.* **305**, 589–603.

Perry, A. E. & Abell, C. J. 1975 Scaling laws for pipe-flow turbulence. *J. Fluid Mech.* **67**, 257–271.

Perry, A. E. & Abell, C. J. 1977 Asymptotic similarity of turbulence structures in smooth- and rough-walled pipes. *J. Fluid Mech.* **79**, 785–799.

Piomelli, U. & Balaras, E. 2002 Wall-layer models for large-eddy simulations. *Annu. Rev. Fluid Mech.* **34**, 349–374.

Pirozzoli, Sergio, Modesti, Davide, Orlandi, Paolo & Grasso, Francesco 2018 Turbulence and secondary motions in square duct flow. *J. Fluid Mech.* **840**, 631–655.

Poinsot, T & Lele, S K 1992 Boundary conditions for direct simulation of compressible viscous flows. *J. Comput. Phys.* **101**, 104–129.

Prandtl, L. 1925 Bericht über die Entstehung der Turbulenz. *Z. Angew. Math. Mech.* **5**, 136–139.

Ricco, Pierre & Quadrio, Maurizio 2008 Wall-oscillation conditions for drag reduction in turbulent channel flow. *Int. J. Heat Fluid Fl.* **29** (4), 891 – 902.

Rosenfeld, Azriel & Kak, Avinash C. 1982 *Digital Picture Processing: Volume 1 and 2*, 2nd edn. Orlando, FL: Academic Press.

Rowley, Clarence W. & Dawson, Scott T.M. 2017 Model reduction for flow analysis and control. *Annu. Rev. Fluid Mech.* **49** (1), 387–417.

Rumsey, Christopher L., Carlson, Jan & Ahmad, Nashat 2019 FUN3D Juncture Flow Computations Compared with Experimental Data. In *AIAA Scitech 2019 Forum*.

Schoppa, W. & Hussain, F. 2002 Coherent structure generation in near-wall turbulence. *J. Fluid Mech.* **453**, 57–108.

Schwarz, W R & Bradshaw, P 1994 Turbulence structural changes for a three-dimensional turbulent boundary layer in a 30° bend. *J. Fluid Mech.* **272**, 183–209.

Schwarz, Walter R & Bradshawt, Peter 1993 Measurements in a pressure-driven three-dimensional turbulent boundary layer during development and decay. *AIAA J.* **31** (7), 1207–1214.

Seddighi, M., He, S., Pokrajac, D., ODonoghue, T. & Vardy, A. E. 2015 Turbulence in a transient channel flow with a wall of pyramid roughness. *J. Fluid Mech.* **781**, 226–260.

Sendstad, Olav & Moin, Parviz 1992 The near wall mechanics of three-dimensional turbulent boundary layers. *Tech. Rep.* Rep. TF 57. Thermo Sci. Div. Mech. Eng. Stanford University.

Sillero, J. A., Jiménez, J. & Moser, R. D. 2013 One-point statistics for turbulent wall-bounded flows at Reynolds numbers up to $\delta^+ \approx 2000$. *Phys. Fluids* **25** (10), 105102.

Sillero, Juan A., Jiménez, Javier & Moser, Robert D. 2014 Two-point statistics for turbulent boundary layers and channels at Reynolds numbers up to $\delta^+ \approx 2000$. *Phy. Fluids* **26** (10), 105109.

Slotnick, J, Khodadoust, A, Alonso, J, Darmofal, D, Gropp, W, Lurie, E & Mavriplis, D 2014 Cfd vision 2030 study: A path to revolutionary computational aerosciences. *NASA/CR-2014-218178* pp. 1–51.

Spalart, Philippe R. 1988 Direct simulation of a turbulent boundary layer up to $Re_\theta = 1410$. *J. Fluid Mech.* **187**, 61–98.

Spalart, Philippe R. 1989 Theoretical and numerical study of a three-dimensional turbulent boundary layer. *J. Fluid Mech.* **205**, 319–340.

Townsend, A. A. 1961 Equilibrium layers and wall turbulence. *J. Fluid Mech.* **11**, 97–120.

Townsend, A. A. 1976 *The structure of turbulent shear flow*, 2nd edn. Cambridge University Press.

Vallikivi, M., Ganapathisubramani, B. & Smits, A. J. 2015 Spectral scaling in boundary layers and pipes at very high Reynolds numbers. *J. Fluid Mech.* **771**, 303–326.

Vreman, AW 2004 An eddy-viscosity subgrid-scale model for turbulent shear flow: Algebraic theory and applications. *Phys. Fluids* **16** (10), 3670–3681.

Waleffe, Fabian 1997 On a self-sustaining process in shear flows. *Phys. Fluids* **9** (4), 883–900.

Wallace, James M. 2016 Quadrant analysis in turbulence research: History and evolution. *Annu. Rev. Fluid Mech.* **48** (1), 131–158.

WANG, M & MOIN, P 2002 Dynamic wall modeling for large-eddy simulation of complex turbulent flows. *Phys. Fluids* **14**, 2043–2051.

WEBSTER, DR, DEGRAAFF, DB & EATON, JK 1996 Turbulence characteristics of a boundary layer over a swept bump. *J. Fluid Mech.* **323**, 1–22.

CARTON DE WIART, CORENTIN, LARSSON, JOHAN & M. MURMAN, SCOTT 2018 Validation of WMLES on a periodic channel flow featuring adverse/favorable pressure gradients. In *Tenth International Conference on Computational Fluid Dynamics (ICCFD10)*, p. 355.

WRAY, A. A. 1990 Minimal-storage time advancement schemes for spectral methods. *Tech. Rep.* MS 202 A-1. NASA Ames Research Center.

WU, XIAOHUA, MOIN, PARVIZ, ADRIAN, RONALD J. & BALTZER, JON R. 2015 Osborne Reynolds pipe flow: Direct simulation from laminar through gradual transition to fully developed turbulence. *Proc. Natl. Acad. Sci.* **112** (26), 7920–7924.

WU, XIAOHUA, MOIN, PARVIZ, WALLACE, JAMES M., SKARDA, JINHIE, LOZANO-DURÁN, ADRIÁN & HICKEY, JEAN-PIERRE 2017 Transitional–turbulent spots and turbulent–turbulent spots in boundary layers. *Proc. Natl. Acad. Sci.* **114** (27), E5292–E5299.

WU, XIAOHUA & SQUIRES, KYLE 1997 Large eddy simulation of an equilibrium three-dimensional turbulent boundary layer. *AIAA J.* **35** (1), 67–74.

WU, XIAOHUA & SQUIRES, KYLE D 1998 Prediction of the three-dimensional turbulent boundary layer over a swept bump. *AIAA J.* **36** (4), 505–514.

WU, XIAOHUA & SQUIRES, KYLE D. 2000 Prediction and investigation of the turbulent flow over a rotating disk. *J. Fluid Mech.* **418**, 231–264.

YANG, Q., WILLIS, A.P. & HWANG, Y. 2019 Exact coherent states of attached eddies in channel flow. *J. Fluid Mech.* **862**, 1029–1059.

YANG, X I A, PARK, G I & MOIN, P 2017 Log-layer mismatch and modeling of the fluctuating wall stress in wall-modeled large-eddy simulations. *Phys. Rev. Fluids* **2**, 104601.

YANG, X I A, SADIQUE, J, MITTAL, R & MENEVEAU, C 2015 Integral wall model for large eddy simulations of wall-bounded turbulent flows. *Phys. Fluids* **27**, 025112.

ZAGAROLA, MARK V. & SMITS, ALEXZNDER J. 1998 Mean-flow scaling of turbulent pipe flow. *J. Fluid Mech.* **373**, 33–79.